

Transactions on **GIGAKU**



GIGAKU Press

Nagaoka University of Technology

Transactions on GIGAKU: Scope and Policy

Nagaoka University of Technology publishes an online, open access journal titled “Transactions on GIGAKU”, which is focused on the science and technology related to GIGAKU*. The mission of this journal is to spread out the concept of GIGAKU and the fruits of GIGAKU to the global world and to be a strong network for innovations in science and technology and for development of next generations of high-level human resources. This journal, therefore, covers research and education activities related to GIGAKU in broad areas.

* See ‘What is GIGAKU?’ below.

‘What is GIGAKU?’

GIGAKU is a term composed of two Japanese word-roots; GI and GAKU. The word GI (技) literally stands for all kinds of arts and technology, and GAKU (学) stands for scientific disciplines in general when used as a suffix.

The term was originally coined to describe the fundamental philosophy of education and research of Nagaoka University of Technology (NUT) when it was established in 1976. Through this term the founders of NUT intended to express their recognition that all technical challenges in the real world require a scientific approach. And NUT has a relentlessly pursued GIGAKU since then.

Fourty-one years have passed and all surrounding conditions have changed dramatically during those years. We are witnessing rapidly globalizing economics and huge scale changes in demographic, industrial and employment structures. All those changes seem to necessitate the further evolution of GIGAKU. In response to this, NUT recently announced its new “Growth Plan” and a renewed definition of the term is given;

GIGAKU is a science of technologies, which gives us an angle to analyze and reinterpret diverse technical processes and objects and thus helps us to advance technologies forward. By employing a broad range of knowledge about science and engineering, management, safety, information technology and life sciences, GIGAKU provides us with workable solution and induces future innovations.

October 2018

Nobuhiko Azuma, President of Nagaoka University of Technology

Editors (2018 to 2019):

Editor-in-chief:

Dr. Masato Aketagawa, Professor, Department of Mechanical Engineering, Nagaoka University of Technology (NUT), Japan

Co-Editors:

Dr. Kazunori Sato, Vice President, NUT (Professor, Department of Materials Science and Technology, NUT)

Dr. Shigeru Nagasawa, Professor, Department of Mechanical Engineering, NUT

Dr. Masatoshi Takeda, Professor, Department of Mechanical Engineering, NUT

Dr. Yukio Miyashita Associate Professor, Department of Mechanical Engineering, NUT

Dr. Masahiro Iwahashi, Professor, Department of Electrical, Electronics and Information Engineering, NUT

Dr. Tomoichiro Okamoto, Associate Professor, Department of Electrical, Electronics and Information Engineering, NUT

Dr. Koichi Takimoto, Professor, Department of Bioengineering, NUT

Dr. Taichi Sugai, Assistant Professor, Department of Nuclear System Safety Engineering, NUT

Dr. Takaomi Kobayashi, Professor, Department of Science of Technology Innovation, NUT

Dr. Takashi Yamaguchi, Professor, Department of Science of Technology Innovation, NUT

Dr. Takashi Yukawa, Professor, Department of Science of Technology Innovation, NUT

Dr. Tadachika Nakayama, Professor, Department of Science of Technology Innovation, NUT

Dr. Yuichi Otsuka, Associate Professor, Department of System Safety, NUT

Dr. Makoto Ichitsubo, Professor, Department of General Education, NUT

Submission and Publishing

“Transactions on GIGAKU” publishes original papers focusing on education, science, and technology related to GIGAKU. Papers submitted are peer-reviewed before publication. Publication charge is free for all submitted papers.

Copyright

The copyright of the papers published in Transactions on GIGAKU is transferred to Nagaoka University of Technology. (See our copyright transfer form for details.)

Contact

gigaku-press@jcom.nagaokaut.ac.jp

(Revised May 2019)

Transactions on GIGAKU

Volume 6, No. 1, April 2019

The 7th International GIGAKU Conference in Nagaoka (IGCN) and The 3rd STI-Gigaku (October 4-5, 2018, Nagaoka University of Technology, Nagaoka, Japan)

The IGCN is designed and organized to provide a cross-border, cross-sector, cross-disciplinary forum for those researchers, educators, and industrial leaders who are creating and practicing GIGAKU in various technology domains in various countries. Some papers presented in the IGCN are published in this first volume of Transactions on GIGAKU.

The STI-Gigaku conference (hosted by NUT) is most importantly to focus on Sustainable Development Goals (SDGs), which are the collection of 17 global goals set by the United Nations as 2030 Agenda, aiming at its world-wide education network system to be proactively integrated onto the next steps while connecting with parties involved in related fields, sectors, and nationalities to share research progress and achievements.

Table of contents

1. Pages 06001/1-8

Enhancement of Evanescent-Light-Induced Wedge Waves due to Water Confinement in a Point-Contact Configuration

Iwao Matsuya, Yuuki Hirai, Yasuhisa Oguro, Takumi Arai, Toshiki Machida,
Takayuki Ishibashi, Ikuo Ihara

2. Pages 06002/1-8

Development of Precision Measuring Robot of Crawler Type and Feasibility Study of Measuring Unit for Improvement of Measurement Accuracy

Ichiro Yoshida, Kazuhide Tanaka

3. Pages 06003/1-8

Effect of Ground Movement Direction on Ultimate Lateral Resistance of Line Alignment Piles in Clay

Quang N. Pham, Satoru Ohtsuka, Koichi Isobe, Yutaka Fukumoto

4. Pages 06004/1-11

High Temperature Gas Cooled Reactor Regulation Development – Operation & Maintenance Perspective

I Wayan Ngarayana, Kenta Murakami

5. Pages 06005/1-11

Galet – Geant4 Based Application Templet for Primers

Tsukasa Aso, Wataru Takase, Takashi Sasaki

6. *Pages 06006/1-8*
Numerical Study on Core Degradation Behavior with TRAC and MCCI Behavior with MELCOR at Fukushima Dai-ichi Nuclear Reactor Accident
Kohei Ueta, Hiep Huy Nguyen, Kazuyuki Takase
7. *Pages 06007/1-6*
Basic property of the wind turbine with the circular cylinder blades driven by longitudinal vortex
Yuya Kimura, Takumi Sankyo, Hayate Kimura, Syodai Sugimura, Takahiro Nomura, Shigeru Ogawa, Yuji Yamada, Tsutomu Takahashi
8. *Pages 06008/1-6*
Observation of Three Dimensional Nanostructures Fabricated by Two-Photon Polymerization Method
Son T. Nguyen¹, M. A. Hariz B. Mohd Pauzi, Tadachika Nakayama, Tsuyoshi Takahashi, Kenya Moriya, Yoshinori Tokoi, Hisayuki Suematsu, and Koichi Niihara
9. *Pages 06009/1-8*
Optimization of Mirror Magnetic Fields in a Permanent Magnet ECR Ion Source for Generation of Multi-Charged Aluminum Ions
Tsubasa Nakamura, Shinji Yamada, Takumi Tomonari, Ayumu Inagaki, Hiroya Uyama, Yuta Wada, Toyohisa Asaji, Kazumasa Takahashi, Toru Sasaki
10. *Pages 06010/1-7*
Purification and antigenicity evaluation of fish-disease bacterial outer membrane proteins for immersion vaccine development
Noriyo Mitome, Nagisa Hamada, Naoki Yamashita, Seng Eng Khuan

Enhancement of Evanescent-Light-Induced Wedge Waves due to Water Confinement in a Point-Contact Configuration

Iwao Matsuya^{1,*}, Yuuki Hirai¹, Yasuhisa Oguro¹, Takumi Arai¹, Toshiki Machida¹, Takayuki Ishibashi², and Ikuo Ihara¹

¹*Department of Mechanical Engineering, Nagaoka University of Technology,*

²*Department of Materials Science and Technology, Nagaoka University of Technology, 1603-1 Kamitomioka-machi, Nagaoka 940-2188, Japan*

**E-mail: matsuya@mech.nagaokaut.ac.jp*

A new method for generating ultrasonic waves utilizing evanescent light during the total internal reflection at the surface of a half ball lens is presented. A waveguide with a sharp wedge is employed as a specimen to launch a wedge wave and the edge tip of the waveguide ridge is attached to the lens to create a contact point between them. A low-power pulsed Nd:YAG laser is irradiated into the lens to form the evanescent light. The effect of water confinement in a point-contact configuration is investigated for the ability of generating wedge waves by comparing in an open system. The amplitude of the first mode 1 wedge wave produced by the evanescent light is enhanced more than eight times due to the water confinement. The similar relationship between the direct ablation and the confined ablation for the direct laser irradiation is demonstrated.

1. Introduction

A laser ultrasonic technique is a powerful tool where an ultrasonic wave is excited by a pulsed laser in a material and material properties are evaluated by detecting its elapsed time [1, 2]. In association with the technique, a shock wave provided by the pulsed laser has been applied in medical applications such as a drug delivery, killing tumors, and so on [3-8]. However, the applicable size has still been limited to a relatively large-scale due to the diffraction limitation of the irradiated light, and a micro-nano scale application has not still been explored for the technique. Recently, in order to overcome the limitation, near-field optics, including evanescent light, has been offered as the method in which the laser energy can be focused on a very small area [9, 10], and that has begun to combine with laser ultrasonic technology [11-14]. If the evanescent light become available as a wave source, especially in a liquid, the unprecedented usability for smaller objects in the application will be developed broadly.

We have been attempting to generate bulk acoustic waves in an aluminum plate utilizing evanescent light formed at a right-angle prism, and it has been successfully carried out [13]. However, the amplitude of the obtained acoustic waves has been easily changed according to the contact state because the plane contact between the plate and the prism is imperfect due to the surface roughness of each plane. Besides, the excited wave signal has usually been nothing but a noise level. On the other hand, there are two methods to generate ultrasonic waves utilizing a pulsed laser ablation. One is direct ablation where the pulsed laser is directly irradiated onto a bulk sample and the ablation causes ultrasonic wave, the other is confined ablation where the target sample is covered with a transparent material such as a glass plate or a liquid and the enhanced ultrasound is generated in the closed system [15-17]. Although the confined ablation is a very important technology in terms of creating an intense ultrasound, we could not have verified that as long as employing the plane-contact configuration.

A wedge wave is a kind of elastic guided wave propagating along a ridge of a sharp blade [18-21]. Wedge waves can propagate for a long distance with a low attenuation because its energy during the travel concentrates in a small spot at the blade tip. The vibration of the wedge wave shows asymmetrical movement across the ridge line and its amplitude is usually much bigger than the other bulk elastic waves. The wedge wave is thus appropriate for being produced by the evanescent light

which only has a small energy. Moreover, the point contact between the waveguide and the prism surface at which the evanescent light is formed can be easily achieved if the edge tip of the waveguide ridge is attached to the prism. Therefore, the contact state is drastically improved compared with the plane contact, and most importantly, the confined ablation for the evanescent light can be realized by arranging a liquid around the contact point.

In the present work, we report a method for generating ultrasonic wave taking advantage of the evanescent light. The half ball lens is employed instead of the right-angle prism to avoid stray light at the oblique side of the prism. A waveguide with a sharp wedge is used to create the intense signal of the wedge wave and to make the point contact configuration. The generation of wedge waves is carried out in both the open system and the closed system. The effect of the water confinement is investigated for the ability of generating wedge waves.

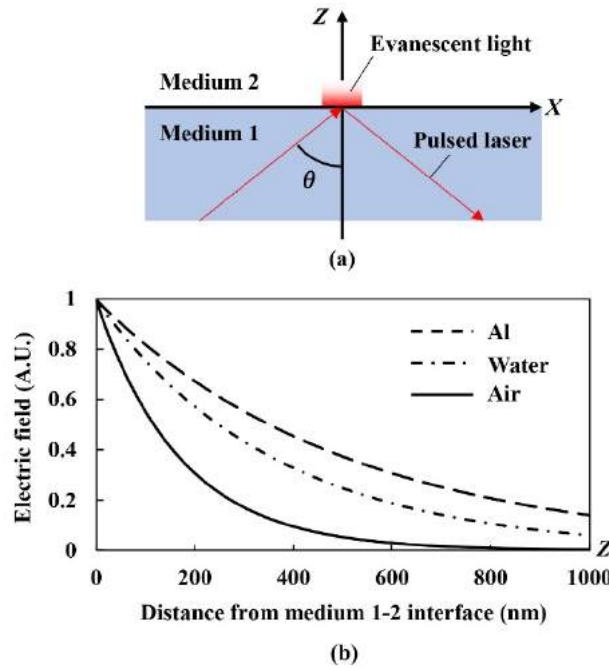


Fig. 1 Scheme of evanescent light generation. (a) Evanescent light and total internal reflection of pulsed laser at medium 1-2 interface. (b) Electric field of evanescent light.

2. Evanescent Light

When the pulsed laser reflects at a boundary between two different mediums, if the incident angle is more than the critical angle, the evanescent light is formed outside the boundary. Figure 1(a) illustrates the scheme of the evanescent light generation. During the total internal reflection of the pulsed laser irradiated from the medium 1 to 2, the evanescent light exhibits exponential decay with distance from the interface. The electric field of the evanescent light at the interface is given by [22]

$$E(x, z) = T_0 \exp\left(-i\omega t + i\frac{2\pi n_1}{\lambda} x \sin \theta\right) \cdot \exp\left(-\frac{2\pi}{\lambda} z \sqrt{\left(\frac{n_1}{n_2}\right)^2 \sin^2 \theta - 1}\right) \quad (1)$$

Here T_0 is maximum amplitude of electric field, ω is angular frequency of the incident light, λ is wave length of the light in the medium 2, and θ is angle of incident light, t represents time. The axis perpendicular to the boundary is Z , the axis equivalent to the boundary is X . n_1 and n_2 are refractive indexes of the medium 1 and 2, and the medium 1 is usually glass. Figure 1(b) shows the electric field of evanescent light along the Z -axis when the medium 2 is changed. The penetration depth of evanescent light into the medium 2, which is the distance where the initial electric field decreases $1/e$, is expressed as follows [22],

$$\Lambda = \frac{1}{\frac{2\pi}{\lambda} \sqrt{\left(\frac{n_1}{n_2}\right)^2 \sin^2 \theta - 1}} \quad (2)$$

where Λ is penetration depth of evanescent light. The refractive indexes are 1.33 for water, 1.37 for aluminum, and 1.51 for glass [13]. In this work, the incident angle of the pulsed laser is determined to be 69.0° which is larger than the critical angle of 62.1° derived from Snell's law for the glass-water interface, and that of 65.1° for the glass-aluminum interface. Using Eq. (2), when the medium 2 is changed, the penetration depths of evanescent light are 170 nm for air, 362 nm for water, 510 nm for aluminum. When the evanescent light illuminates a solid plate specimen which usually has more than $1 \mu\text{m}$ of surface roughness, it does not reach the medium 2 entirely due to the imperfect plane-contact. In order to verify the ability of generating ultrasonic wave using the evanescent light, the point-contact between medium 1 and 2 is essential.

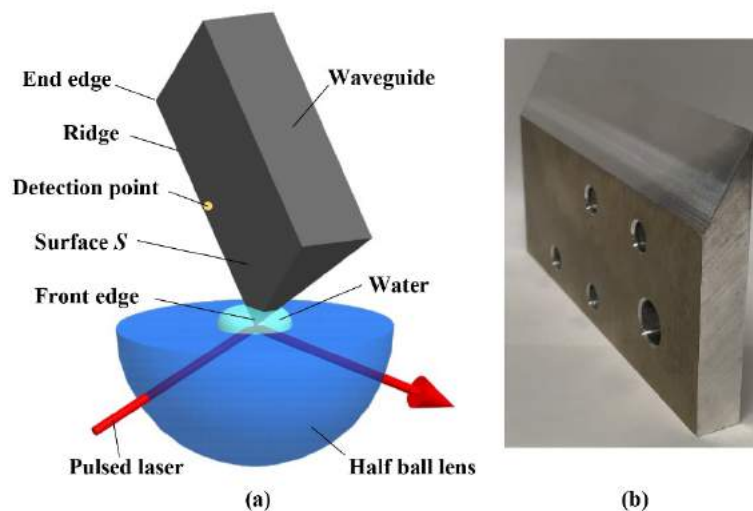


Fig. 2 Schematic depiction of experimental setup. (a) Contact point configuration between waveguide (around ridge) and half ball lens. (b) Picture of waveguide with 30° wedge.

3. Experiment

Figure 2 shows the experimental setup for launching wedge waves on the ridge of the waveguide by means of the evanescent light. A well-polished aluminum (A5052) waveguide with 10 mm thickness is used as a specimen. As shown in Fig. 2(b), the waveguide is 100 mm in length and has a tip angle of 30° , the sharpness of which is measured at an average of $16.3 \mu\text{m}$ by a laser microscope. The flat surface of the half ball lens with 10 mm diameter is positioned to be facing upward. The front edge of the waveguide ridge is attached on the flat surface of the half ball lens to make a point contact between them, the angle between the ridge line and the flat surface is fixed at 45° , and the surface S of the waveguide and the flat surface are normal to each other, as shown in Fig. 2(a). The contact force between the waveguide and the lens is carefully removed to be less than 50 g, which is confirmed not to exceed the proof strength of aluminum by the 3-dimensional elastic analysis simulation. A pulsed Nd:YAG laser (Tempest 30, New Wave Research, 1064 nm) is operated at a 8.2 mW single shot with a duration of 4 ns. When the evanescent light is irradiated on the front edge of the waveguide ridge, the wedge waves are launched and propagated along the ridge of the waveguide. In order to detect wedge waves, a laser doppler vibrometer (OFV-505, Polytec) is used. The detection point in the middle of the waveguide is 50 mm away from the contact point, and the distance between the detection point and the end edge of the waveguide is 50 mm.

Figure 3 shows the simulation result of the ray-trace for the optical system using the optical design software, OpTaliX. A laser beam of 5 mm diameter is focused using a biconvex lens with a 200 mm focal length. The beam is reflected at a mirror to enter the half ball lens at an incident angle of 69° . The focal point is controlled to be placed at a point which is 2 mm away from the reflecting point in

the half ball lens, as shown in Fig. 2. If the pulsed laser is focused at the surface of the half ball lens, it is easily broken due to an energy concentration. But employing this arrangement, the lens is able to endure the laser power up to approximately 22 mW for a single shot. The spot size on the flat surface of the half ball lens is derived at 0.33 mm and 0.18 mm in the major and the minor axis, respectively. The generation of the wedge wave utilizing the evanescent light is carried out with and without water on the flat surface of the half ball lens. For comparison, removing the half ball lens, the pulsed laser is directly focused on the front edge of the waveguide ridge with and without a drop of water. The oval focused-area on the surface S of the waveguide is 0.14 mm and 0.10 mm in the major and the minor axis examined by the knife-edge technique [15].

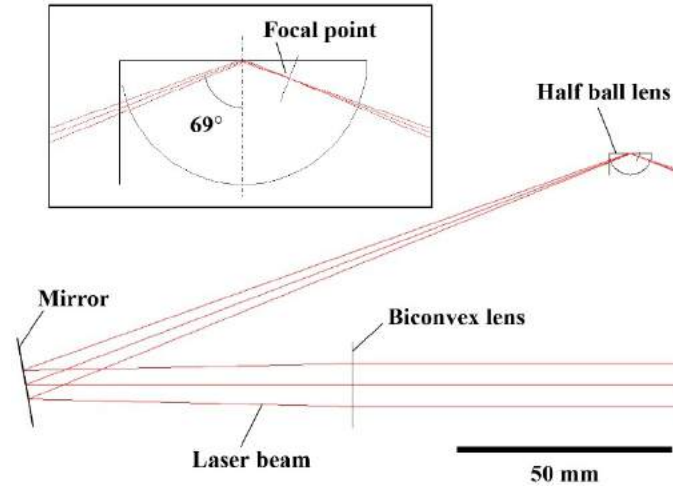


Fig. 3 Ray-trace simulation for optical system. The inset shows enlarged view of the half ball lens.

When the wedge waves are detected by the vibrometer, the voltage signals are captured using a 12-bit serial acquisition board at a sampling rate of 100 MHz. In order to evaluate the waveforms purely, data processing such as a filter or an averaging is not conducted. To derive the velocities of the wedge waves from the waveform, the cross-correlation method is utilized to obtain the elapsed time between the first and the reflected wedge waves from the end edge of the waveguide. The velocity V for wedge wave in the air is reported as an empirical formula as shown below [18],

$$V = V_R \sin(m\phi) \quad (3)$$

where V_R is velocity of Rayleigh wave, m is order of wave mode, ϕ is wedge angle. Since V_R for the waveguide is experimentally obtained 2940 m/s, the velocities of the wedge wave are estimated to be 1470 m/s for mode 1 and 2546 m/s for mode 2. Note that since Eq. (3) is an empirical formula, it is expected that the velocity derived from Eq. (3) is different from the experimental value as the wave mode increases [23].

4. Results and Discussion

Figures 4(a) and 4(b) show the waveforms of the wedge waves excited by the directly-irradiated pulsed laser without water (direct ablation) and with water (confined ablation). In Fig. 4(a), the first small wave is the surface acoustic wave (SAW). The wave packets A_1 and A_2 correspond to the mode 2 wedge wave, which is passed through the detecting point after the launch and is reflected from the end edge of the waveguide. The wave packets B_1 and B_2 correspond to the mode 1 wedge wave. Because of the dispersiveness of wedge waves, the width of the wave packet B_2 in time-domain is widened compared to wave packet B_1 . The velocities of the mode 1 and 2 wedge wave are obtained to be 1462 m/s and 2367 m/s for both cases, which agree well with Ref. 20 and 21 despite the differing launch method. Considering the velocities of the wedge wave and the propagated distance, the wave packets between A_2 and B_2 are the mode-converted wedge waves converted at the end edge of the waveguide. The same tendency concerning the position of the wave packets can be observed in Fig. 4(b), except for the amplitude of the waves. Compared to Fig. 4(a), the peak-to-peak amplitude of the

first mode 1 for the confined ablation is 7.12 times greater than the corresponding one for the direct ablation, which is enhanced from 9.62 to 68.5 A.U.. In general, during laser heating, the produced pressure in confined ablation is 4-10 times greater than direct ablation [16], so this result is considered to be appropriate.

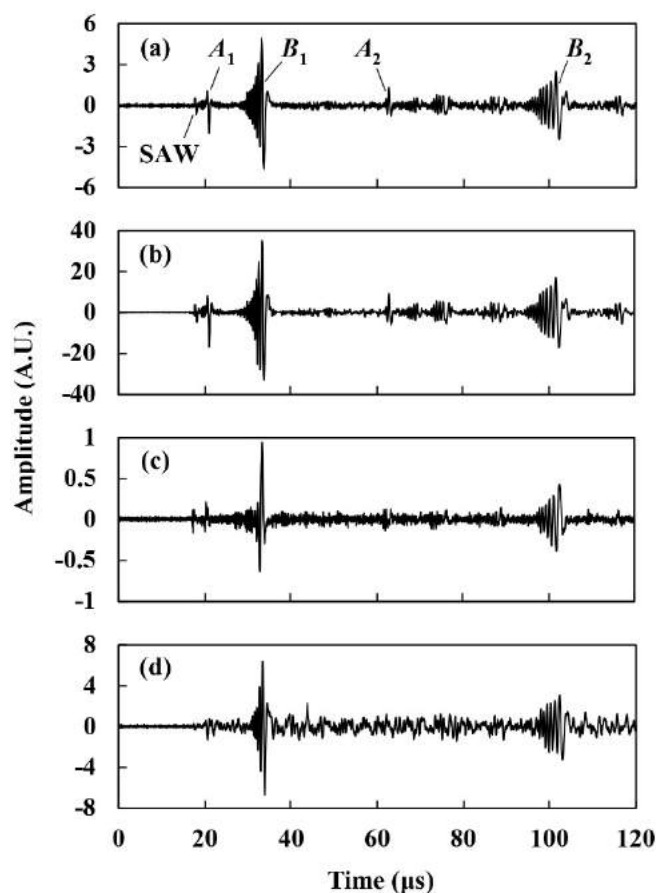


Fig. 4 Waveforms of wedge waves obtained by (a) direct ablation and (b) confined ablation for direct laser irradiation. Those produced by evanescent light in (c) open system and (d) closed system confined by water.

Figures 4(c) and 4(d) show the waveforms of the wedge wave generated by the evanescent light with and without water. Regarding the wave position, the first and the reflected mode 1 and 2 wedge waves are observed as well as the above cases of the direct and the confined ablation. It has been confirmed that the half ball lens vibrates by itself only if the lens breaks. In addition, any breakdown inside the half ball lens was not observed following those experiments. Consequently, it is considered that those major waves in Figs. 4(c) and 4(d) are not brought by the vibration of the lens but excited by the evanescent light. The velocities of the mode 1 and 2 wedge waves are 1446 m/s and 2329 m/s, as shown in Fig. 3(c), and the corresponding ones in Fig. 4(d) are 1449 m/s and 2329 m/s. Those values almost coincide with both cases of the direct and the confined ablation. The peak-to-peak amplitude of the first mode 1 wedge wave in Fig. 4(c) is 1.58 A.U. and the corresponding one in Fig. 4(d) is 13.1 A.U. which is amplified 8.26 times. Although the amplitudes of the evanescent-light-induced wedge wave are roughly one-sixth of those produced by the direct laser irradiation, the similar amplification factor due to the water-confinement is indicated. When the front edge of the waveguide ridge is separated less than 0.5 mm from the surface of the lens, which is far bigger than the penetration depths of the evanescent light in the air and the water, no signal is observed regardless of the existence of the water. Therefore, it is considered that the vibration of the water that absorbs the energy from the

evanescent light was not the excitation source for the wedge waves. Figure 5 shows the scanning electron microscope (SEM) image of the apex of the front edge after the one shot of the evanescent light confined by the water. A triangle-shaped damaged region is observed at the apex. It is considered that the temperature of the waveguide was rapidly increased by the evanescent light irradiation and the apex was melted, vaporized and ionized in the water-confined geometry. Therefore, it is clearly shown the wedge waves were excited by the ablation of the evanescent light on a small scale. We considered the consumed energy for missing volume which is melted and evaporated by the evanescent light. The missing volume is estimated to be $1.00 \times 10^{-13} \text{ m}^3$ at best by using the SEM image as shown in Fig. 6. Note that every corner of the 3D model in Fig. 6 is sharp, which is different from the actual shape, the estimated burnout volume might be excessively large. The density of aluminum is $2.68 \times 10^6 \text{ g/m}^3$, therefore the mass of the missing part is derived to be $2.68 \times 10^{-7} \text{ g}$. Using the mole number of aluminum (26.98 g/mol), the missing volume is $9.93 \times 10^{-6} \text{ mol}$. Consequently, the energy of the burnout of the apex can be calculated to be 3.0 J in the best case by taking advantage of that the heat quantities for melting and vaporizing aluminum are 1.07×10^4 and $2.91 \times 10^5 \text{ J/mol}$, respectively [24]. Compared to the total energy of the irradiated laser (2.1 MJ), the energy consumed by the burnout is considered to be extremely small due to the point contact.

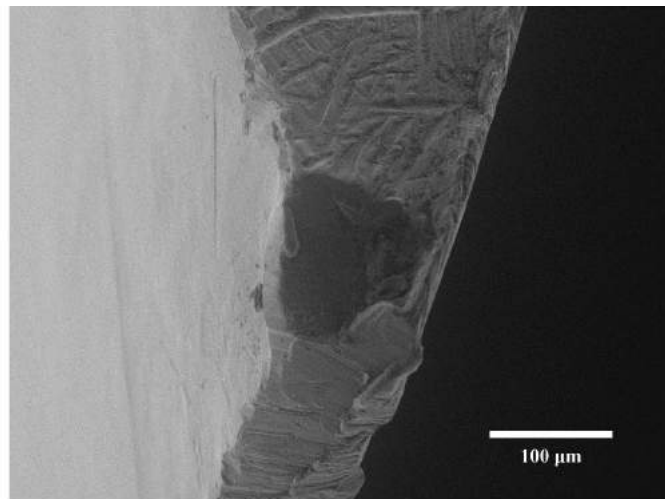


Fig. 5 SEM image of apex of front edge after evanescent light irradiation confined by water.

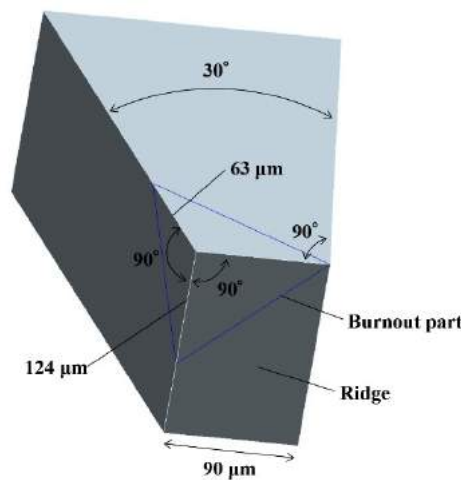


Fig. 6 3D model of missing volume at the apex of front edge.

5. Conclusion

We have reported a novel method for generating ultrasonic waves utilizing evanescent light during the total internal reflection at the flat surface of a half ball lens. The waveguide with a sharp wedge is used as a specimen to obtain clear signal of generated wedge waves which is much bigger than acoustic bulk waves. The point-contact configuration between the tip of the waveguide and the half ball lens is employed to achieve better contact state than the plane contact, and to examine the effect of confined ablation with water. The ray-trace simulation is applied to create the optimal optical system and to avoid breakdown inside the half ball lens. The amplitude of the first mode 1 wedge wave generated by the evanescent light is enhanced more than eight times due to water confinement, which shows a similar relationship between the direct and the confined ablation for the direct laser irradiation. Although the contact point configuration with the wedge was examined to produce wedge waves in this work, it is also possible for the evanescent light to provide an ultrasonic wave or a shock wave for other applications, such as an extremely small material in a liquid medium.

Acknowledgments

This work was supported by JSPS KAKENHI grant numbers 15H03889, 16H04507, 17K18822, and Nagaoka University of Technology (NUT) presidential research grant.

References

- [1] T. Hayashi, "Imaging defects in a plate with complex geometries," *Appl. Phys. Lett.*, vol. 108, Feb. 2016, Art. no. 081901.
- [2] A. Kosugi, I. Ihara, and I. Matsuya, "Accuracy evaluation of surface temperature profiling by a laser ultrasonic method," *Jpn. J. Appl. Phys.*, vol. 51, Feb. 2012, Art. no. 07GB01.
- [3] T. Kodama, M. R. Hamblin, and A. G. Doukas, "Cytoplasmic molecular delivery with shock waves: importance of impulse," *Biophys. J.*, vol. 79, no. 4, Oct. 2000, pp.1821-1832.
- [4] A. G. Doukas, and N. Kollias, "Transdermal drug delivery with a pressure wave," *Adv. Drug Deliv. Rev.*, vol. 56, no. 5, Mar. 2004, pp. 559-579 (2004).
- [5] M. Schmidt, U. Kahlert, J. Wessolleck, D. Maciaczyk, B. Merkt, J. Maciaczyk, J. Osterholtz, G. Nikkhah, and M.O. Steinhauser, "Characterization of a setup to test the impact of high-amplitude pressure waves on living cells," *Sci. Rep.*, vol. 4, Jan. 2014, Art. no. 3849.
- [6] T. Požar, A. Babnik, and J. Možina, "From laser ultrasonics to optical manipulation," *Opt. Express*, vol. 23, no. 6, Mar. 2015, pp. 7978-7990.
- [7] M. T. Tsai, T. Y. Tsai, S. C. Shen, C. Y. Ng, Y. J. Lee, J. D. Lee, and C. H. Yang, "Evaluation of laser-assisted trans-nail drug delivery with optical coherence tomography," *Sensors*, vol. 16, no. 12, Dec. 2016, Art. no. 2111.
- [8] H. J. Nieminen, G. Barreto, M. A. Finnilä, A. G. Pérez, A. Salmi, S. Ranjan, K. K. Eklund, K. P. H. Pritzker, S. Saarakkala, and E. Hæggestörm, "Laser-ultrasonic delivery of agents into articular cartilage," *Sci. Rep.*, vol. 7, Jun. 2017, Art. no. 3991.
- [9] T. Funatsu, Y. Harada, M. Tokunaga, K. Saito, and T. Yanagida, "Imaging of single fluorescent molecules and individual ATP turnovers by single myosin molecules in aqueous solution," *Nature*, vol. 374, Apr. 1995, pp. 555-559.
- [10] T. Ishibashi, and Y. Cai, "Polarization properties in apertureless-type scanning near-field optical microscopy," *Nanoscale Res. Lett.*, vol. 10, Sep. 2015, Art. no. 375.
- [11] U. Störkel, K. L. Vodopyanov, and W. Grill, "GHz ultrasound wave packets in water generated by an Er laser," *J. Phys. D: Appl. Phys.*, vol. 31, no. 18, Mar. 1998, pp. 2258-2263.

- [12] P. Ahn, Z. Ahang, C. Sun, and O. Balogun, "Ultrasonic near-field optical microscopy using a plasmonic nanofocusing probe," *J. Appl. Phys.*, vol. 113, Jun. 2013, Art. no. 234903.
 - [13] I. Matsuya, K. Matozaki, A. Kosugi, and I. Ihara, "A feasibility study on generation of acoustic waves utilizing evanescent light," *J. Phys. Conf. Ser.*, vol. 520, Jun. 2014, Art. no. 012003.
 - [14] X. Chen, B. Dong, and O. Balogun, "Near-field photothermal heating with a plasmonic nanofocusing probe," *Int. J. Thermophys.*, vol. 37, Jan. 2016, Art. no. 26.
 - [15] C. B. Scruby, and L. E. Drain, "Laser Ultrasonics Techniques and Applications," Taylor & Francis Group, New York, 1990.
 - [16] R. Fabbro, J. Fournier, P. Ballard, D. Devaux, and J. Virmont, "Physical study of laser produced plasma in confined geometry," *J. Appl. Phys.*, vol. 68, no. 2, Jul. 1990, pp. 775-784.
 - [17] L. Berthe, R. Fabbro, P. Peyre, L. Tollier, and E. Bartnicki, "Shock waves from a water-confined laser-generated plasma," *J. Appl. Phys.*, vol. 82, no. 6, Sep. 1997, pp. 2826-2832.
 - [18] P. E. Lagasse, "Analysis of a dispersionfree guide for elastic waves," *Electron. Lett.* 8, 372 (1972).
 - [19] P. D. Pupyrev, A.M. Lomonosov, A.P. Mayer, "Laser-generated ultrasonic pulse shapes at solid wedges," *Ultrasonics*, vol. 70, Apr. 2016, pp. 75-83.
 - [20] I. Matsuya, Y. Honma, M. Mori, and I. Ihara, "Measuring liquid-level utilizing wedge wave," *Sensors*, vol. 18, Dec. 2017, Art. no. 2.
 - [21] I. Matsuya, Y. Honma, and I. Ihara, "Experimental study on liquid-level measurement based on laser ultrasonic technique and tip-generated wedge wave," *Proc. Mtgs. Acoust.*, vol. 32, Apr. 2018, Art. no. 030012.
 - [22] M. Ohtsu, and M. Hori, "Near-Field nano-optics, From Basic Principles to Nano-Fabrication and Nano-Photonics," Plenum Publishers, New York, 1999.
 - [23] M. Billy, "Acoustic technique applied to the measurement of the free edge wave velocity," *Ultrasonics*, vol. 34, Aug. 1996, pp. 611-619.
 - [24] P. W. Atkins, "Atkins' Physical Chemistry," Oxford University Press, England, 2014.
- (Received: 11 October 2018, Accepted: 6 February 2019)*

Development of Precision Measuring Robot of Crawler Type and Feasibility Study of Measuring Unit for Improvement of Measurement Accuracy

Ichiro YOSHIDA^{1,*}, Kazuhide TANAKA²

¹⁾ Department of Mechanical Engineering, Faculty of Science and Engineering, Hosei University,

²⁾ Major in Mechanical Engineering, Graduate School of Science and Engineering, Hosei University,
3-7-2 Kajinocho, Koganei-shi, Tokyo 184-8584, Japan

*E-mail: yoshida.ichiro@hosei.ac.jp

Precision geometrical quantity measurements are absolutely necessary in electric power stations (steam power station, nuclear power station, and etc.) for environmental load reduction, quality assurance, and safety. These precision measurements are difficult manual operations. Specifically, these measurements are often performed in high or narrow places, uncomfortable environments, and so on. As such, power station employees are subjected to stressful situations and painful postures, among other difficulties. Hence, we studied and developed a precision geometrical measuring robot to relieve stress and improve the work environment. Herein, we propose the research on precision measuring robot that is a precision measurement instrument with mobility. The robot proposed in this paper is a mobile, crawler-type precision measuring robot that can perform surface roughness measurements. Handling robots that supply workpieces to surface roughness instruments have been developed; however, we do not know of research on the robotization and self-propulsion for roughness measurement instruments. Stiffness and stability of mechanical structure is important for high-precision measurement; however, the measurement accuracy of the measuring robot decreases because of the decrease in stiffness and stability caused by the lightweight structure needed for robotization. Therefore, we propose a measuring unit that uses electromagnets. In this research, the mechanism and structure of the measuring unit was designed and developed, and the effectiveness and capability of the developed measuring unit were examined through experiments. From the results of the measuring experiments, standard deviations of the roughness parameter value, Ra, were improved from one third to half by using the proposed measuring unit with electromagnets.

1. Introduction

Precision geometrical quantity measurements in electric power stations are absolutely necessary for environmental load reduction, quality assurance, and safety [1-3]. These precision measurements are difficult manual operations. Specifically, these measurements are often performed in high, narrow places, uncomfortable environments, and so on. As such, power station employees are subjected to stressful situations and painful postures, among other difficulties. Hence, we study and develop a precision geometrical measuring robot to relieve stress and to improve the working environment.

Examples of precision geometric quantity measurements in electric power stations include length measurement, form measurement, geometrical tolerance measurement, surface roughness measurement, surface texture measurement, and wear measurement, among others. In this work, we propose and develop a precision crawler-type geometrical measuring robot that can measure surface roughness, because surface texture influences the environmental loading and lifespan of power stations. To the best knowledge of the authors, this research is the first that introduces a precision geometrical measuring robot with mobility for surface roughness measurement. Presently, handling robots that supply workpieces for surface roughness instruments have been developed [4]; however, we do not

know of research on robotization and self-propulsion for roughness measurement instruments. Furthermore, in this research, we develop a measuring unit to improve the accuracy of the roughness measurement. Weight reduction of the robot is essential to enable self-propulsion and smooth motion; however, the measurement accuracy of the measuring robot deteriorates as its stiffness and stability decrease as a result of the lightweight structures. Therefore, we propose a measuring unit using electromagnets. In this research, we design and develops the mechanism and structure for the measuring unit. The effectiveness and capability of the developed measuring unit are examined through experiments. From the results of the measuring experiments, standard deviations of the roughness parameter value, Ra, were improved from one third to half by using the measuring unit with electromagnets.

2. Precision Measuring Robot

In this research, we designed and developed a prototype of a precision measuring robot. In earlier studies, we presented a basic concept and conceptual design for the precision measuring robot [5, 6]. Figure 1 shows the developed prototype precision measuring robot in this research. Figure 2 shows the 3D CAD model of the prototype precision measuring robot as a schematic diagram. Specifically, the precision measuring robot is a roughness measurement instrument that is capable of self-propulsion by crawlers. The size of the robot is 400 mm long, 280 mm wide, and 220 mm high. Additionally, the primary structure of the robot consists of aluminum plates and frames for weight reduction. As shown in Figs. 1 and 2, the crawlers for self-propulsion are arranged on both sides of the main body of the robot, and the surface roughness measuring unit is located at the center of the robot. The crawlers are driven by two geared motors (TG-47G-SG-50-HA, TSUKASA Electric Co., Ltd.) and eight sprocket wheels. The main components of the precision measuring unit are a contact-type surface roughness measuring sensor, a drive unit for the roughness measuring sensor, electromagnets, and a vertically moving unit for the roughness sensor, drive unit, and electromagnets. The details of the prototype precision measuring unit are introduced in the following section.

Electronic circuits for controlling the crawlers and the roughness measuring unit are arranged on top of the robot at the rear. A microcontroller in the electronic circuits uses Arduino, which is an open-source electronics platform based on hardware and software [6]. As shown in Fig. 3, the transmission of control commands to the electronic circuits of the precision measuring robot and reception of measured results by the precision measuring robot are performed wirelessly by a Bluetooth connection.

3. Precision Measuring Unit Using Electromagnets

In this research, we designed and developed a prototype precision measuring unit for improvement of measurement accuracy.

In general, precision measurement instruments are designed such that the stability and stiffness of the instrument are high, because high measurement accuracy is a top priority. However, improving the stiffness causes the instrument to be heavy. In contrast, a robot must be lightweight, because the motion of the robot becomes disabled if the weight of robot is designed as heavy as a precision measurement instrument with high stiffness. However, the measurement accuracy of the precision measuring robot deteriorates, because robotization of a precision measurement instrument involves a

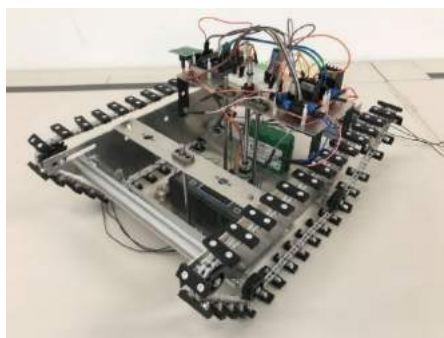


Fig. 1 Prototype precision measuring robot for roughness measurement.

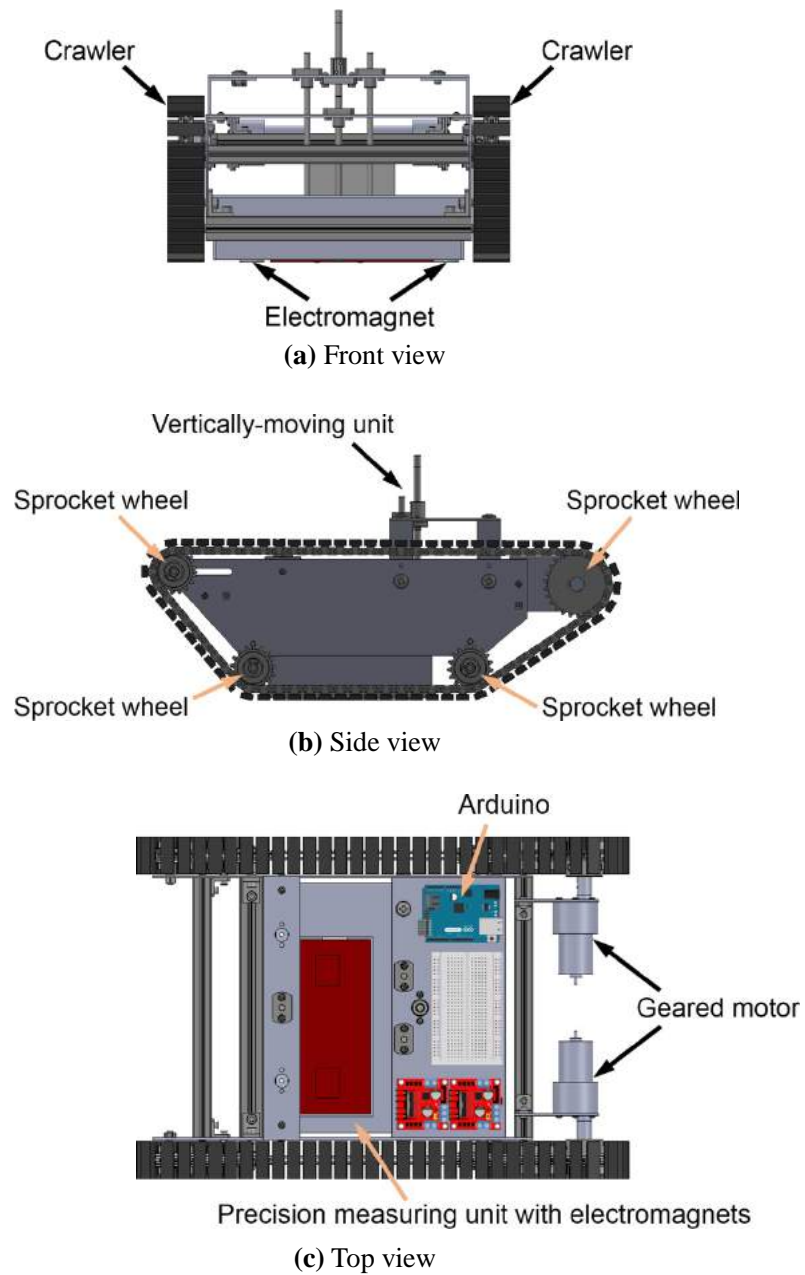


Fig. 2 Schematic diagram of prototype precision measuring robot.

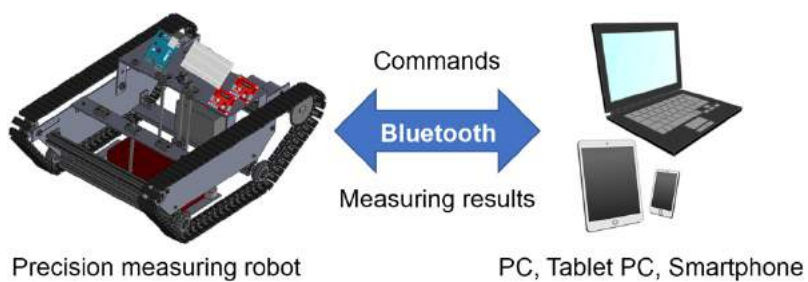
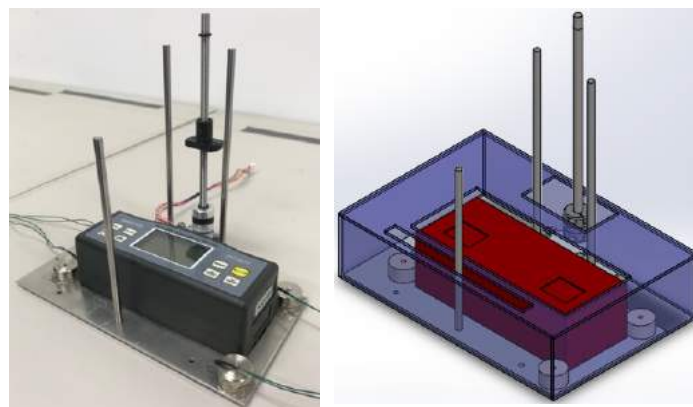
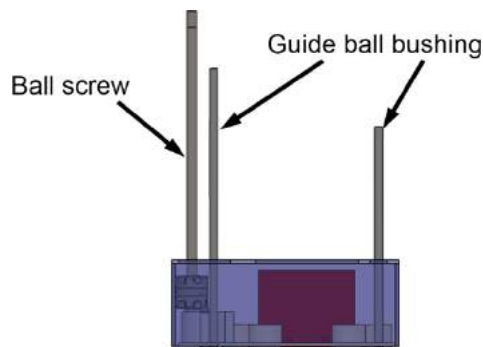


Fig. 3 Radio communication via Bluetooth.

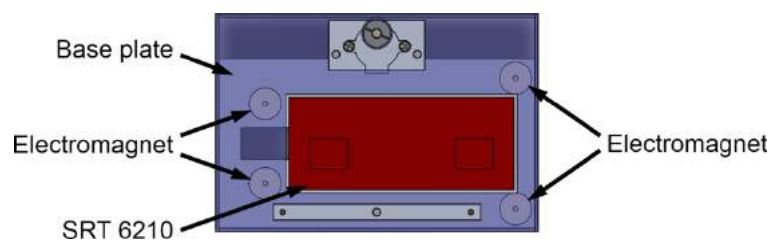
decreased stability and stiffness associated with the weight reduction. Therefore, we devised an application of electromagnets for the precision measuring unit to solve this problem and develop a prototype of the precision measuring robot. Figure 4 shows the internal structure of the prototype precision measuring unit. The measuring unit has three guide ball bushings and one ball screw coupled to a geared motor. The measuring unit is vertically moved by the ball screw. The unit has four electromagnets (Uxcell Co., Ltd., 12 V, 0.24 A, 25 N of magnetic force, and 20 mm diameter), two of which are located at the corner positions of the rectangular base plate of the measuring unit. The electromagnet attracts the measuring machine and the measuring surface during measurement. We consider that the electromagnet can suppress vibration of the measuring machine unit at the time of measurement. The other two are located at nearby positions of both sides of the roughness sensor to improve measuring accuracy. In the present study, the contact-type surface roughness measuring sensor and the drive unit for the sensor were not developed; consequently, a portable surface roughness tester SRT 6210 (Nihon Sonatest Advanced Inspection Technology Inc.) was utilized. When measuring roughness, the stylus slides on the measuring surface. The stylus detects irregularities on the measure-



(a) Perspective view



(b) Side view



(c) Top view

Fig. 4 Internal structure of the precision measuring unit using electromagnets.

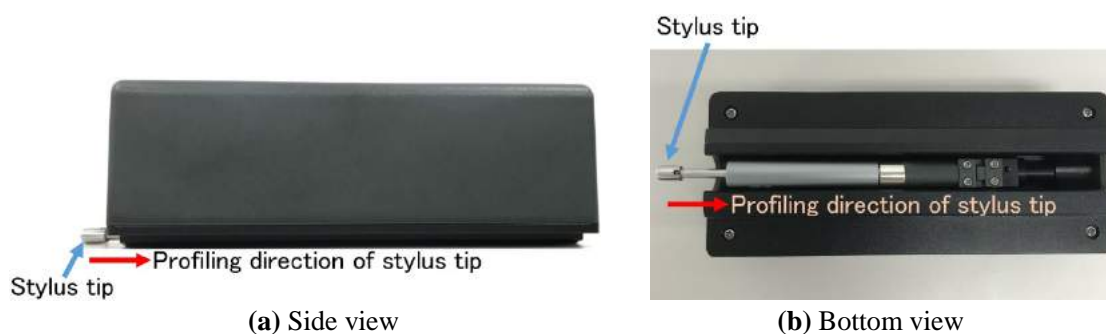


Fig. 5 Stylus of the surface roughness tester SRT 6210

Table 1 Specification of the surface roughness measuring instrument [7, 8]

Parameters	Ra, Rz, Rq, Rt
Measuring Range	Ra, Rq: 0.005 - 16.00 μm
	Rz, Rt: 0.020 - 160.0 μm
Accuracy	$\leq 10\%$
Fluctuation of display value	$\leq 6\%$
Sensor	Test Principle: Inductance type
Radius of Probe Pin	5 μm
Material of Probe Pin	Diamond
Dynamo-measurement of Probe	4 mN(0.4 gf)
Probe Angle	90 degrees
Vertical Radius of Guiding Head	48 mm
Maximum driving stroke	17.5 mm
Cutoff length (l)	0.25 mm / 0.8 mm / 2.5 mm optional
	sampling length = 0.25 mm, $V_t = 0.135$ mm/s
	sampling length = 0.8 mm, $V_t = 0.5$ mm/s
Driving speed	sampling length = 2.5 mm, $V_t = 1$ mm/s
Profile digital filter	Filtered Profile: Gauss
Evaluation length	5 cut-off

ment surface. The roughness parameter is calculated by analyzing the unevenness of the measured surface. The stylus is operated by the measuring unit. The position of the stylus is shown in Figure 5. The measurement principle of the roughness sensor is a method of converting stylus deviations into electrical signals with a piezoelectric element. Commands to, and results from, the measuring unit are transmitted and received via Bluetooth wireless radio. Table 1 lists the specification of the surface roughness measuring instrument.

4. Experiment

This paper presents a basic experiment for the precision measuring robot. The robot elevates the measuring unit after each roughness measurement, and thereafter, moves to a next position. Subsequently, after movement to the next position, the robot measures the surface roughness at the position by lowering the measuring unit. Table 2 lists the roughness measurement results obtained using the developed precision measuring robot. Experiments were performed on a cast iron precision surface plate, and surface roughness parameters Ra, $Rz_{1/5}$, and Rq [9, 10] were measured. For

inspection of the precision of the robot, the parameters were measured 10 times at each of two different positions—A and B. To verify the validity of the measuring unit with electromagnets, measurements were taken with the electromagnets turned on and off at each position. As listed in Table 2, the measurement result is reasonable because it is within the accuracy of Table 1. When the electromagnets are turned off, the average measurement results for position A are Ra is 0.287 μm , RZ_{JIS} is 0.812 μm , Rq is 0.364 μm ; and those for position B were Ra is 0.217 μm , RZ_{JIS} is 0.615 μm , and Rq is 0.264 μm . When the electromagnets are turned on, the average results for position A are Ra is 0.284 μm , RZ_{JIS} is 0.804 μm , Rq is 0.366 μm ; those for position B are Ra is 0.213 μm , RZ_{JIS} is 0.603 μm , and Rq is 0.266 μm . To verify the validity of the measuring unit and electromagnets, the standard deviations and ranges of the measurement results are also shown in Table 2. When the electromagnets are turned from off to on, the standard deviations of Ra are improved from 5.6 nm to 2.4 nm at position A, and from 4.1 nm to 1.0 nm at position B. Similarly, the standard deviations of RZ_{JIS} are improved from 15.8 nm to 6.9 nm at position A, and from 11.3 nm to 3.0 nm at position B. The standard deviations of Rq are improved from 9.3 nm to 4.5 nm at position A, and from 3.0 nm to 1.8 nm at position B. Moreover, when the electromagnets are turned from off to on, the ranges of Ra are improved from 21.0 nm to 7.0 nm at position A, and from 14.0 nm to 3.0 nm at position B. Similarly, the ranges of RZ_{JIS} are improved from 60.0 nm to 19.0 nm at position A, and from 38.0 nm to 9.0 nm at position B. The ranges of Rq are improved from 33.0 nm to 13.0 nm at position A, and from 10.0 nm to 6.0 nm at position B. From these experimental results, we consider that the use of the measuring unit with electromagnets results in reduction of measurement variation. Table 3 lists the results of measuring similar measurement points on a different surface roughness measuring machine SJ 210 (Mitutoyo Corporation) [11]. Comparing the measurement result by SRT 6210 when the electromagnets are turned off with the measurement result by SJ 210, Ra and Rq are the same, and RZ_{JIS} is not the same. However, the

Table 2 Measurement results of roughness parameters Ra, RZ_{JIS}, and Rq by the developed precision measuring robot, and validity of the measuring unit and electromagnets.

Times	Position A						Position B					
	Ra μm		RZ _{JIS} μm		Rq μm		Ra μm		RZ _{JIS} μm		Rq μm	
	Electromagnet		Electromagnet		Electromagnet		Electromagnet		Electromagnet		Electromagnet	
	OFF	ON	OFF	ON	OFF	ON	OFF	ON	OFF	ON	OFF	ON
1st	0.276	0.289	0.782	0.817	0.342	0.371	0.207	0.211	0.587	0.597	0.257	0.262
2nd	0.283	0.282	0.801	0.798	0.355	0.364	0.214	0.213	0.606	0.603	0.262	0.265
3rd	0.289	0.282	0.817	0.798	0.366	0.366	0.217	0.214	0.616	0.606	0.264	0.267
4th	0.291	0.286	0.823	0.811	0.366	0.373	0.218	0.214	0.619	0.606	0.266	0.267
5th	0.297	0.286	0.842	0.811	0.375	0.371	0.217	0.214	0.616	0.606	0.264	0.267
6th	0.284	0.284	0.804	0.804	0.366	0.369	0.221	0.214	0.625	0.606	0.266	0.267
7th	0.286	0.282	0.811	0.798	0.369	0.362	0.217	0.213	0.616	0.603	0.265	0.266
8th	0.284	0.282	0.804	0.798	0.364	0.362	0.22	0.212	0.622	0.600	0.267	0.267
9th	0.289	0.283	0.817	0.801	0.369	0.364	0.218	0.213	0.619	0.603	0.266	0.268
10th	0.289	0.283	0.817	0.801	0.369	0.36	0.221	0.213	0.625	0.603	0.267	0.268
Average	0.287	0.284	0.812	0.804	0.364	0.366	0.217	0.213	0.615	0.603	0.264	0.266
Standard deviation	5.6	2.4	15.8	6.9	9.3	4.5	4.1	1.0	11.3	3.0	3.0	1.8
Range	21.0	7.0	60.0	19.0	33.0	13.0	14.0	3.0	38.0	9.0	10.0	6.0

Table 3 Results of roughness parameters Ra, RZ_{JIS}, and Rq by SJ 210.

Times	Position A			Position B		
	Ra μm	RZ _{1/5} μm	Rq μm	Ra μm	RZ _{1/5} μm	Rq μm
1st	0.284	1.098	1.756	0.195	0.819	0.253
2nd	0.286	1.149	1.836	0.192	0.777	0.25
3rd	0.285	1.178	1.841	0.195	0.796	0.253
4th	0.285	1.159	1.842	0.195	0.783	0.253
5th	0.285	1.174	1.851	0.196	0.800	0.255
6th	0.286	1.208	1.868	0.196	0.843	0.255
7th	0.287	1.202	1.897	0.197	0.804	0.256
8th	0.287	1.238	1.923	0.197	0.821	0.256
9th	0.287	1.229	1.914	0.197	0.813	0.257
10th	0.288	1.246	1.940	0.198	0.797	0.254
Average	0.286	1.188	1.867	0.196	0.805	0.254
Standard deviation nm	1.2	45.8	54.2	1.7	19.4	2.0
Range nm	4.0	148.0	184.0	6.0	66.0	7.0

standard deviation by SJ 210 is higher than SRT 6210. Therefore, the result of RZ_{1/5} cannot conclude which surface roughness measuring machine is correct.

5. Conclusion

We designed and developed a precision measuring robot. Moreover, a measuring unit with using electromagnets was proposed, and its effectiveness and capability was confirmed through experiments. The main conclusions obtained in this study are as follows:

- 1) In this study, a precision roughness measuring robot was proposed as a new precision roughness measurement instrument, and it was designed and developed. To the best knowledge of authors, this research is the first that introduces a precision geometrical measuring robot that is a mobile surface roughness instrument with mobility.
- 2) We proposed using electromagnets to mitigate the measurement accuracy deterioration of the measuring robot due to the decrease in stiffness and stability. The prototype precision measuring unit using electromagnets was designed and developed.
- 3) The proposed measuring unit with electromagnets can improve the standard deviations of roughness parameters Ra, RZ_{1/5}, and Rq from one third to half, or greater. Because the effect of utilizing electromagnets for measurement accuracy improvement was confirmed through a basic experiment, the idea of this research is considered valid and efficacious.

Our plans for future work are as follows: 1) The authors will analyze the frequency characteristics of the precision measuring robot and the measuring unit with electromagnets. The effect and mechanism of the electromagnets will be examined and clarified by both experimental and numerical analysis. 2) The authors will design and develop an optimized measuring robot and unit by using the frequency analysis results. 3) Demonstration experiments with the developed precision measuring robot will be performed in industrial fields for commercialization.

Acknowledgment

A part of this work was supported by the JKA Foundation Research Project Number 2017M-102, Japan. The authors would like to thank the JKA Foundation.

References

- [1] Ken Onishi, Yukifumi Kohata, Noriko Onishi and Kimihiro Shinoyama, "Development of manipulators for nuclear power plants' maintenance and an hierarchical open system," Journal of the robotics society of japan, Vol. 34, No. 4, pp. 280-290, May. 2016.
 - [2] Seungho Kim and Chang-Hwan Choi, "The robotic technology applications on nuclear power plants in Korea," Journal of the robotics society of japan, Vol. 23, No. 5, pp. 548-551, July 2005.
 - [3] Lynne E. Parker and John V. Draper, "Robotics applications in maintenance and repair," Handbook of Industrial Robotics, 2nd Edition, edited by Shimon Nof, pp. 1-16, Mar. 1999.
 - [4] Kosaka Laboratory Ltd., "Non-contact surface roughness measuring instrument," <https://mect-japan.com/2017/visitor/information.php?ChargeNo=134>, [accessed 18 August 2018].
 - [5] I. YOSHIDA, K. TANAKA, and H. KIM, "Precision measurement robot for assisting efficiency improvement of energy plant," The Hyper-Interdisciplinary Conference 2018, TEPIA Advanced Technology Gallery, Tokyo, Japan, vol. 7, P-9, p. 84, 2nd- 3rd, Mar. 2018.
 - [6] I. YOSHIDA and K. TANAKA, "Development of Precision Measuring Robot of Crawler Type and Feasibility Study of Measuring Unit for Improvement of Measurement Accuracy," The 7th International GIGAKU Conference (IGCN2018), Nagaoka University of Technology, Niigata, Japan, RD-002, p. 15, 5th- 6th, Oct. 2018.
 - [7] Arduino homepage, <https://www.arduino.cc/>, [accessed 1 September 2018].
 - [8] AIT inc., "SRT-6210 manual Ver. 2402," pp. 1-18, 2012.
 - [9] AIT inc., "SRT-6210 Home Page," <http://www.ait-ultrasonic.jp/details1122.html>, [accessed 10 January 2019].
 - [10] ISO 4287:1997/ Amendment. 1: 2009, "Geometrical Product Specifications (GPS) – Surface Texture: Profile Method – Terms, Definitions and Surface Texture Parameters," Apr. 1997.
 - [11] JIS B 0601:2013, "Geometrical Product Specifications (GPS) – Surface Texture: Profile Method – Terms, Definitions and Surface Texture Parameters," Mar. 2013.
 - [12] Mitutoyo Corporation, "Surface Roughness Measuring Machines Home Page," <https://www.mitutoyo.co.jp/products/hyomen/hyomen.html>, [accessed 10 January 2019].
- (Received: 17 October 2018, Accepted: 13 March 2019)*

Effect of Ground Movement Direction on Ultimate Lateral Resistance of Line Alignment Piles in Clay

Quang N. Pham^{1,*}, Satoru Ohtsuka¹, Koichi Isobe² and Yutaka Fukumoto¹

¹Nagaoka University of Technology, 1603-1, Kamitomioka, Nagaoka, Niigata, 940-2188, Japan

²Hokkaido University, 13 Kita, 8 Nishi, Kita-ku, Sapporo, Hokkaido, 060-8628, Japan

*E-mail: s155066@stm.nagaokaut.ac.jp

This study estimated the ultimate lateral resistance of pile group against horizontal ground movement by using two-dimensional rigid plastic finite element method (RPFEM). The effect of ground movement direction on the ultimate lateral resistance was investigated through the case studies. According to the results, it can be seen that changes in both the ultimate lateral resistance and the failure mode of ground around piles were observed. The impact of the pile spacing on load bearing ratios was studiously investigated. Since each pile in the group affects other piles, it leads the load bearing ratio significantly to depend on pile positions such as the front or back piles. Moreover, the load bearing ratio of each pile went up with an increase in pile spacing, but it was different remarkably among piles. The load bearing ratio varied with the directions of the ground movement.

1. Introduction

Pile foundation is designed not only to carry a vertical load of superstructures, but also to resist a horizontal load and a bending moment. In earthquake engineering, the examination of lateral resistance of pile group against horizontal movement of ground is an important task in the design of pile foundation. These days, the design value for lateral resistance of pile has increased as an increase in measured ground response displacement of clayey soils during earthquakes. It makes the design of pile foundation mainly severe on economical aspect. Therefore, it is crucial to assess the ultimate lateral resistance of piles against large horizontal ground movement since it provides an extreme condition of design on load applied to pile.

Several studies reported the ultimate lateral resistance of single pile such as Broms et al. (1964), Randolph and Houlsby (1984). Broms (1964) studied the slip line method to calculate the ultimate lateral resistance of single pile in the range of $8.28 c_u$ - $12.56 c_u$ for various pile sections under smooth and rough conditions on the interface between pile and soils, in which c_u is un-drained shear strength of soil. Chen et al. (1994), Chen and Poulos et al. (1997), Georgiadis and Sloan et al. (2013) used the numerical analysis to calculate the ultimate lateral resistance of pile groups. However, most of the previous studies analyzed the limit load for the prescribed load applied to the piles. Hence, the past work focused on the ultimate lateral resistance of single piles because the load applying to each pile in a pile group was not known prior to an analysis. This study newly defines the boundary condition for assessment of ultimate lateral resistance of pile groups against horizontal ground movement. The author simulated the pile-soil system by employing a two-dimensional rigid plastic finite element analysis based on the upper bound theorem. Rigid plastic finite element method (RPFEM) has been applied to geotechnical engineering by Tamura et al. (1987) and developed for frictional material as Tamura et al. (1991). In this method, the limit load is calculated without any assumption on potential failure modes. The method is effective in computing the ultimate lateral resistance of pile group against horizontal ground movement in clayey soil.

In this study, the pile-soil system is simulated for rough condition on the interface between pile and soils under two-dimensional condition. The ultimate lateral resistance of the pile group is affected by many factors, such as pile spacing, number of piles, and directions of the ground movement. However, only a few studies have considered the effect of loading direction on the ultimate lateral

resistance such as Georgiadis et al. (2013), Zhao et al. (2017). They demonstrated the change in the total ultimate lateral resistance and the failure mode of ground around the pile. The effect of the number of piles arranged in a row was not considered. This study investigated the effects of the directions of ground movement on the ultimate lateral resistance by increasing the number of piles in a group. Load bearing ratios of piles in groups are calculated by adjusting the pile spacing.

2. Rigid plastic finite element method

Tamura (1991) developed the rigid plastic constitutive equation for frictional material. The Drucker-Prager's type yield function is expressed as follow.

$$f(\boldsymbol{\sigma}) = \alpha I_1 + \sqrt{J_2} - k = 0 \quad (1)$$

where I_1 is the first invariant of stress σ_{ij} and $I_1 = tr(\sigma_{ij})$ in which extension stress is defined positive.

J_2 is the second invariant of shear stress s_{ij} and $J_2 = \frac{1}{2} s_{ij} s_{ij}$ and the coefficients, $\alpha = \frac{\tan \phi}{\sqrt{9 + 12 \tan^2 \phi}}$

and $k = \frac{3c}{\sqrt{9 + 12 \tan^2 \phi}}$ are the material constants in which ϕ is internal friction angle and c is cohesion

under the plane strain condition. The volumetric strain rate is expressed as follows:

$$\dot{\epsilon}_v = tr(\dot{\boldsymbol{\epsilon}}) = tr\left(\lambda \frac{\partial f(\boldsymbol{\sigma})}{\partial \boldsymbol{\sigma}}\right) = tr\left(\lambda \left(\alpha \mathbf{I} + \frac{\mathbf{s}}{2\sqrt{J_2}}\right)\right) = \frac{3\alpha}{\sqrt{3\alpha^2 + \frac{1}{2}}} \dot{\epsilon} \quad (2)$$

where λ is an indetermine multiplier and \mathbf{I} is the unit stress tensor. The strain rate $\dot{\boldsymbol{\epsilon}}$ which is purely plastic component should satisfy the volumetric constraint condition as follow:

$$h(\dot{\boldsymbol{\epsilon}}) = \dot{\epsilon}_v - \frac{3\alpha}{\sqrt{3\alpha^2 + \frac{1}{2}}} \dot{\epsilon} = \dot{\epsilon}_v - \eta \dot{\epsilon} = 0 \quad (3)$$

in which $\dot{\epsilon}_v$ and $\dot{\epsilon}$ indicate the volumetric strain rate and the norm of strain rate, respectively. The parameter η is defined in Eq. (3). The rigid plastic constitutive equation is expressed by Lagrangian method after Tamura (1991) as follows:

$$\boldsymbol{\sigma} = \frac{k}{\sqrt{3\alpha^2 + \frac{1}{2}}} \frac{\dot{\boldsymbol{\epsilon}}}{\dot{\epsilon}} + \beta \left(\mathbf{I} - \eta \frac{\dot{\boldsymbol{\epsilon}}}{\dot{\epsilon}}\right) \quad (4)$$

where β represents a Lagrangian multiplier which indicates the equilibrating stress satisfying the yield function expressed by Eq.(1). Moreover, the constraint condition on strain rate is introduced into the constitutive equation directly with the use of penalty method (Hoshina et al. (2011), Quang et al. (2018)). The stress-strain rate relation for the Drucker-Prager's yield function is expressed as follow:

$$\boldsymbol{\sigma} = \frac{k}{\sqrt{3\alpha^2 + \frac{1}{2}}} \frac{\dot{\boldsymbol{\epsilon}}}{\dot{\epsilon}} + \kappa \left(\dot{\epsilon}_v - \eta \dot{\epsilon}\right) \left(\mathbf{I} - \eta \frac{\dot{\boldsymbol{\epsilon}}}{\dot{\epsilon}}\right) \quad (5)$$

where κ is a penalty constant. FEM with this constitutive equation provides the equivalent equation of the upper bound theorem in plasticity so that this method is called as RPFEM in this study. It is noted the property of this constitutive equation that the relationship between stress and strain rate is specified. The norm of strain rate is substantially indeterminate since the limit state of structure is focused. Stress is determined for normalized strain rate using its norm. Hoshina et al. (2011) introduced the constraint condition on external work into the equilibrium equation by using the penalty method. They reported that more rational results were obtained by the developed method than by methods in previous works. The use of the penalty method is advantageous in that it can shorten the computation time and lead to stable computational results. Since this study focuses on cohesive soils, as mentioned above, the constitutive equation is limited to the von Mises yield function where the

ground is frictionless and deforms under a constant volume. The rigid plastic constitutive equation is simple and effective for assessing the limit state of the ground due to the advantage of not using an uncertain elastic modulus for the ground.

3. Ultimate lateral resistance of line alignment piles

3.1 Analysis boundary condition of model under plane-strain condition

Figure 1 shows two ways to simulate pile-soil system under different boundary conditions. The typical finite element mesh and the boundary condition of single pile against horizontal ground movement are shown in model (a). The soil and pile were assumed as rigid perfectly plastic material, with the following properties: the undrained shear strength of soil was $c_u=100$ kPa and the internal friction angle of soil was $\phi=0^\circ$, while the shear strength of pile material was $c_p=50000$ kPa and the internal friction angle of pile was $\phi=0^\circ$. Analyses were performed for a pile diameter of $D=0.6$ m. In particular, the outer boundary elements perpendicular to the direction of ground movement employ rigid elements to simulate the homogeneous ground movement. A uniform distributed load was applied at all nodes of the rigid outer boundary elements to define the prescribed load and the load -

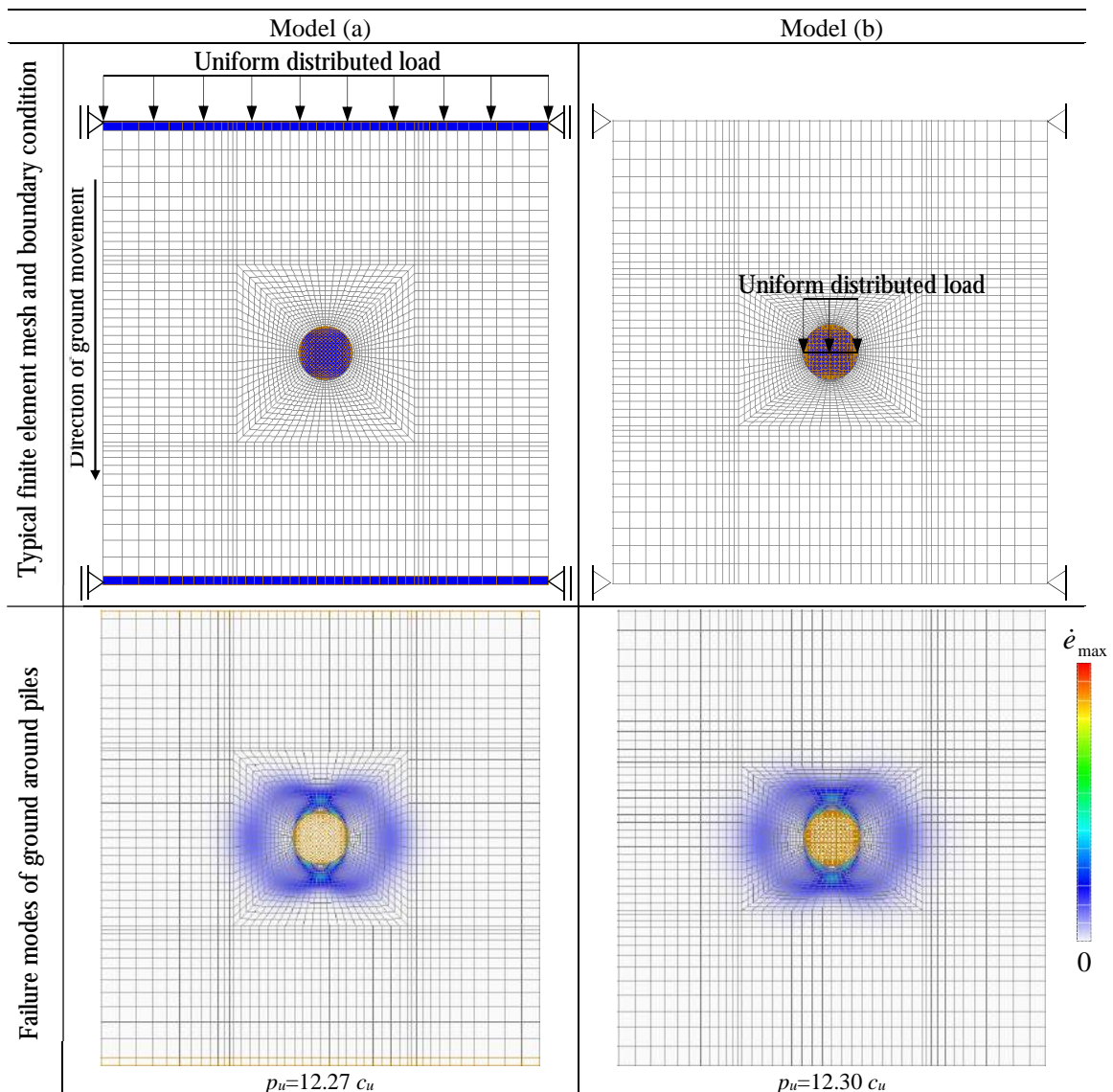


Fig. 1 Boundary conditions and failure modes of single pile in two models

coefficient. The ultimate lateral resistance was assessed by computing the limit value for this load coefficient, and be set up with the started load factor of 1. The center of the pile was set as a fixed velocity boundary condition and the reaction of the piles was calculated to analyse the load bearing ratio. Moreover, the distance from the center of the pile to four boundary surfaces was set at more than $10.0D$ to avoid the effect of boundary conditions on the failure mode of the ground around pile. Model (b) shows the second boundary condition for directly applying the load on pile as the previous works. The center of pile was set with the free condition but the four boundary surfaces were set by a fixed condition. The analysis was performed by applying the uniform distributed load at all nodes of the pile diameter.

The obtained results of strain rate distribution for two models are shown in Fig. 1. The norm of the strain rate presented contour lines in the range of $\dot{\epsilon}_{max} \sim \dot{\epsilon}_{min} (= 0)$. The distribution of $\dot{\epsilon}$ shows the failure mode of the ground reflecting pile-soil interaction effect. Figure 1 shows similarly to the failure mode of single pile in both boundary conditions. The failure mode of ground around pile is observed in the range of $1.5D$ - $2.0D$ from the center of pile and same the slip-line of Broms (1964), Georgiadis and Sloan (2013). The ultimate lateral resistance of single pile generally obtained a close value as $12.27 c_u$ for the model (a), $12.30 c_u$ for the model (b), in which the total resistance is normalized with the length of the pile diameter. The difference in ultimate lateral resistance is about 0.24% and probably due to the difference in finite element meshes. These values are almost similar $11.95 c_u$ of Georgiadis and Sloan (2013). The difference may be caused by the fact that they employed different models, namely, the soil and the pile were modeled as linear elastic-perfectly plastic and linear elastic materials in their work.

In model (a), the obtained value of single pile was observed to coincide with model (b) and the previous work. It proved that the method proposed for assessment of the ultimate lateral resistance of piles is rational and accurate. Hence, model (a) is effective to calculate not only total ultimate lateral resistance of piles, but also load bearing ratio of piles

3.2 Effect of direction of ground movement on ultimate lateral resistance.

As mentioned above, the purpose of this study is to investigate the effects of the direction of ground movement on ultimate lateral resistance by considering the pile number. The ultimate lateral resistance was systematically computed for changes in the pile spacing where the spacing s is the distance between the centers of two piles. The horizontal direction angle is defined as the angle between the direction of ground movement and the pile to pile axis, and varies from 0 to 90 degrees. This study used the average ultimate lateral resistance of piles to discuss the effect of the direction of ground movement. The average ultimate lateral resistance (q/c_u) of piles is expressed as q/c_u to indicate the normalized value by the undrained shear strength of clay c_u . The average ultimate lateral resistance q (kN/m^2) is subsequently calculated by dividing the total ultimate lateral reaction force Q (kN/m) by the pile diameter and the number of piles.

Figure 2 shows the relationship between the average ultimate lateral resistance and the pile spacing for an increase in pile number. The ultimate lateral resistance of the pile is normalized by the length of the pile diameter. As a result, since the setting of shear strength and the pile diameter does not affect the ultimate lateral resistance. In the case of two-pile, the average ultimate lateral resistance reduced almost proportionally to the decrease in direction angle of ground movement in the range of $1.0D$ - $3.0D$ and it coincided with that of single pile in the range of $4.0D$ - $6.0D$ in pile spacing. While the average ultimate lateral resistance increased non-linearly with an increase in pile spacing for all direction cases. In the case of 90 degrees, the average ultimate lateral resistance was achieved slightly higher than that of single pile in the range of nearly $1.0D$ - $1.75D$. It is because the intermediate ground between two piles behaved as a rigid block as shown in Fig. 3(a). It seems appropriate that the average ultimate lateral resistance was the greatest in case of 90 degrees, since the substantial distance of pile spacing projected to the perpendicular plane against the ground movement was the largest even if the pile spacing is the same. However, as the failure mode of the pile-soil system varied depending on the pile spacing, the peak value in average ultimate lateral resistance was obtained at pile spacing of around $1.25D$. The trend to locally form the peak value was observed for other inclination angles at around pile spacing of $1.25D$. In the case of three-pile and four-pile groups, the obtained results also show

the similar trend with that of two-pile group in Figs. 2(b), (c). However, the difference in average ultimate lateral resistance between the case of 90 and 0 degrees increased with an increasing number of piles. In the case of 90 degrees, the average ultimate lateral resistance of pile obtained the same for pile spacing despite number of piles. However, in the case of 0 degrees, the average ultimate lateral resistance was shown to vary with the number of piles and to decrease with an increase in the number of piles. The effect of the number of pile on the trend in ultimate lateral resistance against pile spacing

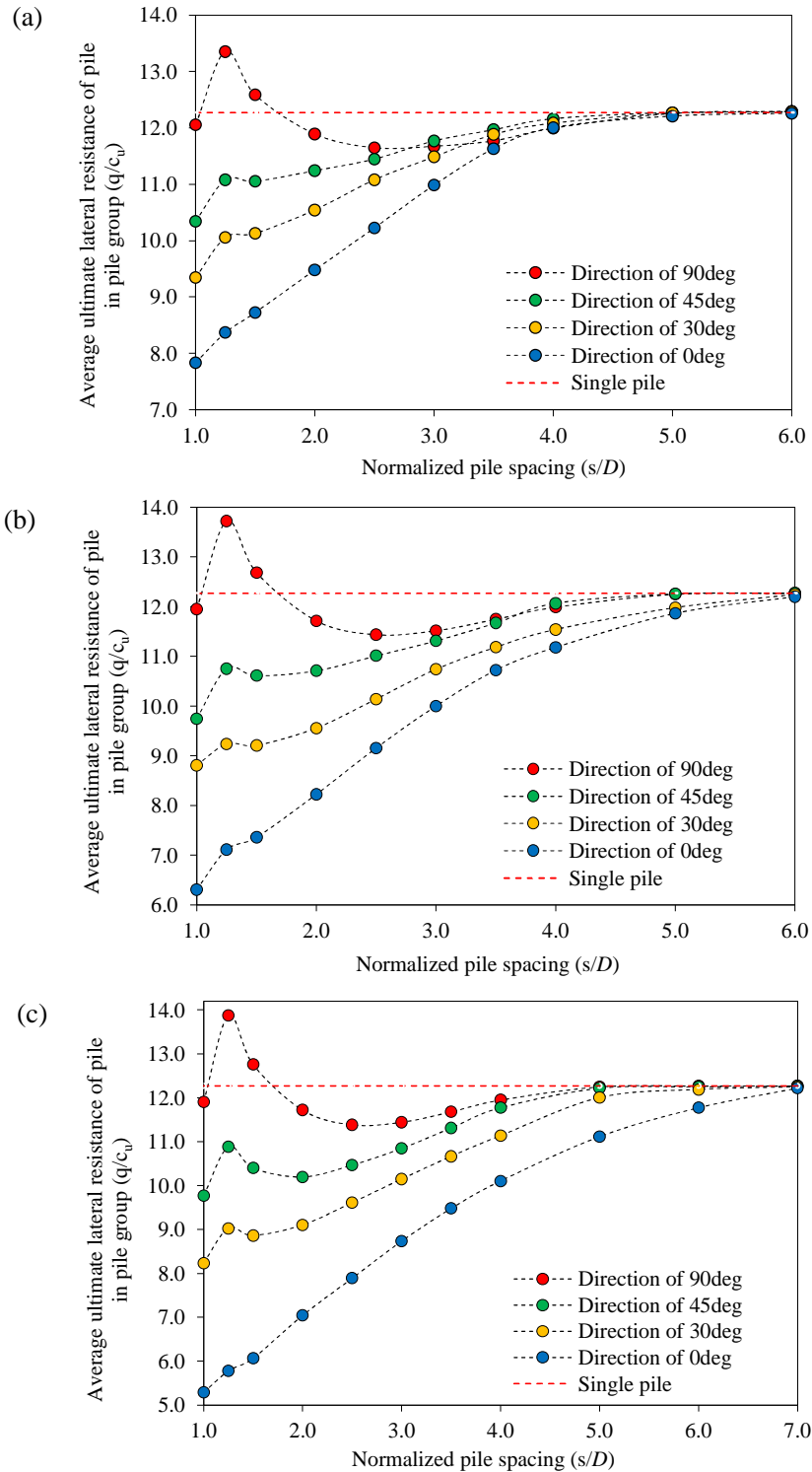


Fig. 2 Average ultimate lateral resistance of piles: (a) two-pile, (b) three-pile and (c) four-pile groups

changed with number of pile, where the range of pile spacing to vary the ultimate lateral resistance became wider. The other cases varying from 0 to 90 degrees were found to exist in between those of 0 and 90 degrees.

As discussed above, the effect of the direction of the ground movement was caused by the change in the failure mode of the ground around the piles. The typical failure modes of two-pile, three-pile and four-pile groups were influenced by the direction of the ground movement at $S=1.25 D$ spacing shown in Fig. 3. In case of 0 and 90 degrees, the intermediate ground of piles did not yield any plastic deformation, whereas it clearly yielded the plastic deformation in case of 45 degrees. It indicates the shearing of intermediate ground took place despite the same pile spacing with the case of 0 and 90 degrees. It is interesting that the failure mode changed due to direction of ground movement in spite of smaller pile spacing, besides the ultimate lateral resistance varied continuously between the values of 0 and 90 degrees. From Figs. 3(a) to 3(c), it is apparent that the area of failed ground became wider as the number of piles was greater. The failure zone of ground around pile was observed about $3.0 D$ - $3.5 D$ from the center of pile for two-pile group, $4.5 D$ - $5.0 D$ for three-pile group and $5.5 D$ - $6.0 D$ for four-pile group.

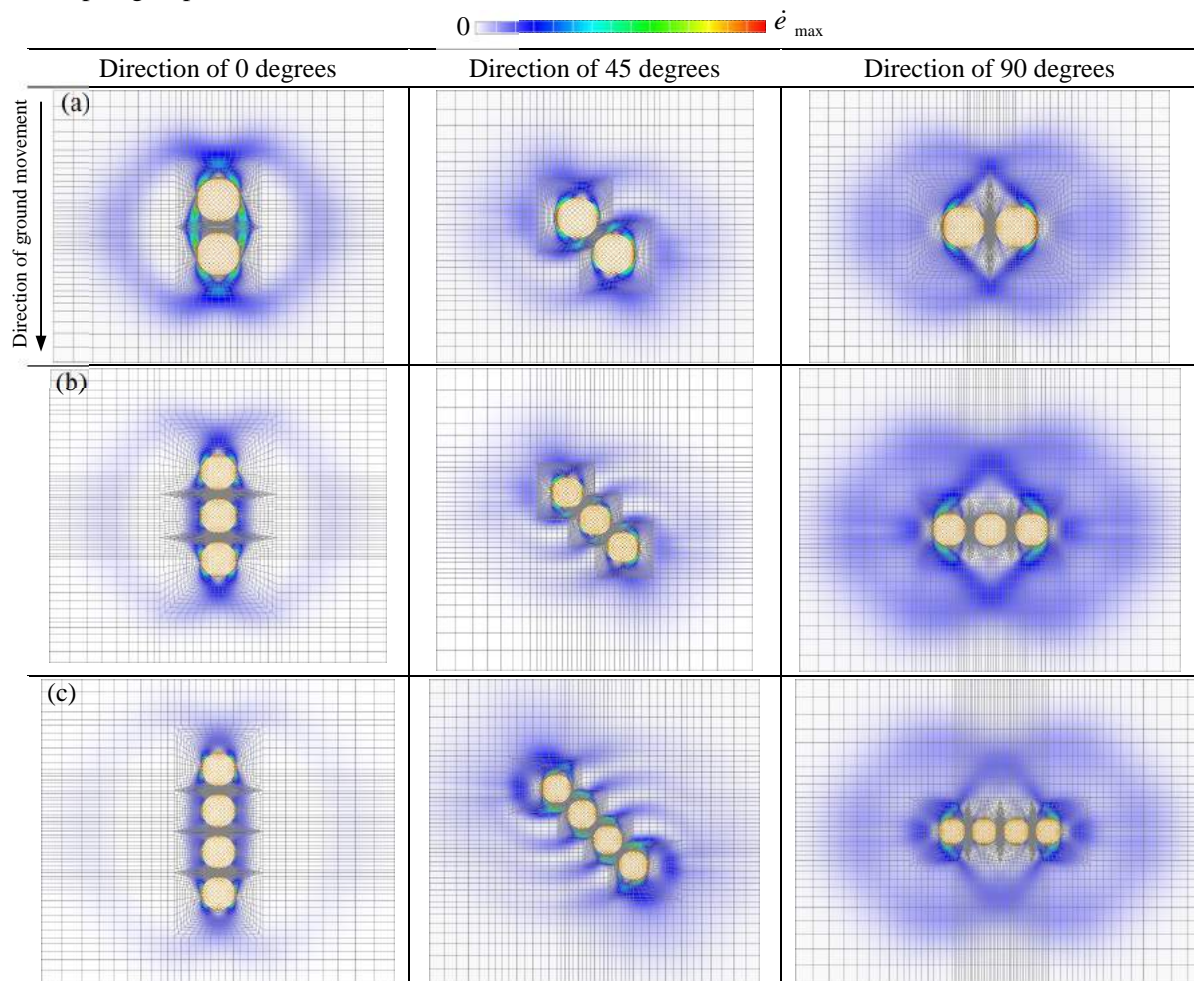


Fig. 3 Failure modes of pile groups at $S=1.25 D$ in cases of 0, 45 and 90 degrees, respectively
(a) two-pile, (b) three-pile and (c) four-pile groups

4. Load bearing ratio of piles in the pile groups

In order to better understand the effect of the ground movement direction on the pile behaviour, the lateral resistance of each pile in a group is calculated. The ratio of the lateral resistance of each pile to that of a single pile is defined as the load bearing ratio. The obtained results show significant

difference among piles in groups. The load bearing ratios were often less than 1.0 and showed the same trend as to increase with a rising pile spacing. Table 1 and 2 express the summary of obtained results on load bearing ratio of piles for two-pile and three-pile group in various direction of ground movement. It can be observed that the load bearing ratio significantly depend on the pile spacing and the direction of ground movement.

Table 1. Summary of load bearing ratios in case of 0 and 90 degrees

Group size	Pile spacing	Load bearing ratio		
		1st pile	2nd pile	3rd pile
 0deg.	1.5D	0.76	0.67	
	2.0D	0.81	0.73	
	3.0D	0.93	0.86	
	4.0D	0.99	0.96	
	5.0D	1.00	0.99	
 90deg.	1.5D	1.03	1.03	
	2.0D	0.97	0.97	
	3.0D	0.95	0.95	
	4.0D	0.98	0.98	
	5.0D	1.00	1.00	
 0deg.	1.5D	0.72	0.52	0.57
	2.0D	0.86	0.54	0.61
	3.0D	0.94	0.75	0.76
	4.0D	0.97	0.91	0.85
	5.0D	1.00	0.98	0.92
 90deg.	1.5D	1.04	1.02	1.04
	2.0D	0.98	0.90	0.98
	3.0D	0.98	0.85	0.98
	4.0D	1.00	0.94	1.00
	5.0D	1.00	1.00	1.00

Table 2. Summary of load bearing ratios in case of 45 degrees

Group size	Pile spacing	Load bearing ratio					
		1st pile		2nd pile		3rd pile	
		x	y	x	y	x	y
 Direction of ground movement	1.5D	0.04	0.93	0.05	0.87		
	2.0D	0.03	0.94	0.04	0.90		
	3.0D	0.03	0.97	0.03	0.95		
	4.0D	0.02	1.00	0.03	0.99		
	5.0D	0	1.00	0	1.00		
 Direction of ground movement	1.5D	0.02	0.92	0.07	0.79	0.03	0.89
	2.0D	0.02	0.93	0.06	0.80	0.03	0.91
	3.0D	0.01	0.96	0.04	0.87	0.01	0.93
	4.0D	0	1.00	0.03	0.98	0	0.99
	5.0D	0	1.00	0	1.00	0	1.00

In the case of 0 degrees, the two-pile and three-pile were investigated. The ratios of the front pile were achieved greater than that of the back pile. The difference in the load bearing ratios of the piles was significantly large. While the difference was greatly observed at a small pile spacing, and less than at large pile spacing. It is noted that the load bearing ratio of middle pile was the smallest as the pile spacing was small in the group of three-pile.

In the case of 90 degrees, the two-pile and three-pile were calculated. The load bearing ratio of each pile was obtained generally close to a single pile. The variance in the ratios was comparatively small among the piles despite the pile spacing. In the computation results, the load bearing ratio of the center pile was obtained smaller than that of the 3rd pile in case of 0deg, besides less than that of the outer pile in case of 90deg. It is caused by overlapping degree in shear zones for adjacent piles. These results agreed well with the model tests of Miao et al. (2008).

In the case of direction of 45 degrees, the same trend in load bearing ratios was obtained as in the case of 90 degrees. However, it is interesting that two orthogonal components existed in the reaction force, in which the x and y component indicate the perpendicular and the parallel components to the direction of the ground movement, respectively. The x component of reaction was generally very small in comparison to the y component of reaction. Hence, the load bearing ratio of the piles almost coincided with the y component of reaction.

5. Conclusions.

The conclusions of this study are as follows:

1. The ultimate lateral resistance of isolated single pile was obtained about $12.27 c_u$ for the perfectly rough piles in clayey soils. The failure zone of the ground around the pile was found to be in range of $1.5D-2.0D$ from the center of the pile, and almost similar to the results of Broms (1964).
2. In the case of the piles in a row considering the pile number, the effect of the direction of the ground movement on the ultimate lateral resistance was widely investigated. It can be seen that the ultimate lateral resistance varied greatly depending on the direction of the ground movement and the number of pile. For the piles in a row orthogonal to the ground movement, the ultimate lateral resistance of each pile was larger than that of a single pile at small pile spacing. On the contrary, for the piles in a row parallel to the direction of ground movement, the ultimate lateral resistance of each pile decreased proportionally to the decrease in pile spacing. In addition, the failure zone of ground around the piles became wider as the number of pile increased.
3. The load bearing ratio of each pile was computed in detail with the changes in the direction of ground movement. It varied among the piles by reflecting the directions of the ground movement.

References

- [1] Broms, B.B. Lateral Resistance of Piles in Cohesive Soils. Journal of the Soil Mechanics and Foundations Division. ASCE. 90 (2), 27-63 (1964).
- [2] Chen, L.T. and Poulos, H.G. Piles Subjected to Lateral Soil Movements. J. Geotech. Geotech. Eng. ASCE. 123 (9), 802-811 (1997).
- [3] Georgiadis, K., Sloan S. W., Lyamin A.V. Effect of loading direction on the ultimate lateral soil pressure of two piles in clay. Géotechnique. 63 (13), 1170-1175 (2013).
- [4] Hoshina, T., Ohtsuka, S. and Isobe, K. Ultimate bearing capacity of ground by rigid plastic finite element method taking account of stress dependent non-linear strength property. Journal of Applied Mechanics. 6, 191-200 (2011). (in Japanese)
- [5] Quang, N.P., Ohtsuka, S., Isobe K., Fukumoto Y. Group effect on ultimate lateral resistance of piles against uniform ground movement. Soils and Foundations. 58(6), 1-14 (2018).
- [6] Tamura, T., Kobayashi, S. and Sumi, T. Rigid Plastic Finite Element Method for Frictional Materials. Soils and Foundations. 27 (3), 1-12 (1987).
- [7] Zhao, Z., Kouretzis, G., Sloan, S.W. and Gao, Y. Ultimate lateral resistance of tripod pile foundation in clay. Computer and Geotechnics. 92, 220-228 (2017).

(Received: 9 October 2018, Accepted: 18 December 2018)

High Temperature Gas Cooled Reactor Regulation Development – Operation & Maintenance Perspective

I Wayan Ngarayana^{1,2*}, Kenta Murakami¹

¹*Department of Nuclear System Safety Engineering, Nagaoka University of Technology,
1603-1 Kamitomioka-machi, Nagaoka 940-2188, Japan*

²*National Nuclear Energy Agency of Indonesia
PUSPIPTEK Area, Serpong, South Tangerang, Indonesia*

**e-mail: ngarayana@batan.go.id*

Abstract. Demands for better safety, security, safeguard and economic aspects have led to the emergence of innovative nuclear reactor designs. One of the new designs is the High Temperature Gas Cooled Reactor (HTGR). HTGR and including all of the Generation IV nuclear reactors have a safety paradigm that is completely different from current nuclear reactor technology. Since most of the nowadays commercial Nuclear Power Plants (NPPs) operating in the world are based on water coolant reactor technology, the development of HTGR makes the current regulations will no longer suitable. Regulation is already known to have a strong correlation with operation & maintenance optimisation that make the preparation of the new regulation become very important. As the part of that purpose, this study is conducted in order to prepare the more flexible regulatory framework for operation & maintenance activities but without overriding the safety aspects. The safety functions of HTGR are investigated by adopting the graded approach and examine the importance of each function. The regularly operating systems having high safety importance are identified, and the reliability models of these systems are discussed. Furthermore, a detailed reliability model of a regular system in an existing light water reactor is prepared to conduct a numerical demonstration on the application of risk information for operation & maintenance. This study indicates that the current graded approach methodology is not suitable. Therefore, new graded methodology should be proposed as the part of future HTGR reliability-based regulation development.

Keywords: nuclear, power, plant, HTGR, Generation IV, operation, maintenance, reliability, regulation

1. Introduction

Base on the Power Reactor Information System (PRIS) provided by International Atomic Energy Agency (IAEA), in the end of 2018 there are 454 on operation commercial NPPs [1]. From all of those NPPs, about 97% of them are water coolant based NPP. The rests are 3 Fast Breeder Reactors (FBR) and 14 Gas Cooled Graphite Moderated Reactor (GCR). Those NPPs supplying about 298.65 GW world energy demand [2]. Unfortunately, about 63% of them already more than 30 years old which their operation must be extended soon by following ageing management requirements or be decommissioned and replaced with the new one.

As a part of the old NPP replacement and the need of massive energy in some developing country especially in China and India, there are about 56 under construction commercial NPPs around the world that is dominated by water coolant based reactors [1]. The interesting thing is one of the under-construction reactors are Generation IV nuclear reactor based on High Temperature Gas Cooled Reactor (HTGR) technology that is located in China [3]. China able to become the first home of the commercial demonstration Generation IV reactor not only because they need massive energy supply for their strong economic development [4], but because of their regulation. China's regulatory body

relatively easier to give license for the new type of nuclear reactor [5].

Regulation is the key points of nuclear safety. But on the other side, regulation is well-known as a factor which is very influential on the costs that must be incurred for the NPP starting from the license, construction, operation, to the decommissioning [6]. The structure of the regulation system effecting on the length of the process to get the license. Additional costs also arise due to the presence of a number of non-nuclear permits that must be taken care. At the time of construction, nuclear regulation and such other regulation such as labour and environment licenses are also very influential on investment and overnight costs. On the operation stage, different regulations greatly affect the freedom of the operator to utilize operational & maintenance optimisation [7].

Since most of the NPP technology adopted around the world is currently based on water coolant reactor technology, causing almost all IAEA standards also based on that technology. In fact, developed regulations based on water coolant reactors are not suitable to be used to regulate other types of the reactor including Generation IV NPPs. Therefore, studies and efforts to develop the regulatory framework to support the implementation of Generation IV NPP are needed.

In our previous study, we found that although many techniques, methods and strategies have been developed in the effort to optimize NPP operation and maintenance, most of them could not be applied due to constraints on regulatory issues [7]. As part of the commercialisation, the regulation also will become the important thing of HTGR development. Therefore, the study in this article has been conducted in order to harmonize the interests of operators in carrying out optimal operation & maintenance against the interests of regulators in providing safety assurance. For that purposes, on the rest of this article, Section 2 will be started with the explanation of the basic concept of HTGR and its safety function identification. Section 3 describing the methodology used in this study. Section 4 discussing the study result. And finally, on Section 5 this article will be closed by the conclusion.

2. Basic Concept of HTGR

HTGR is an advanced development of the Gas Cooled Reactor (GCR) technology. GCR uses carbon dioxide gas as its primary coolant. One disadvantage of carbon dioxide as a coolant is at a relatively high operating temperature. Oxidation of carbon dioxide against moderator graphite can be ruled out only at temperatures below 675°C [8]. At higher temperatures, carbon dioxide undergoes radiolytic oxidation which produces carbon monoxide and attacks graphite so that it has the potential to accelerate the degradation process. Therefore, to produce higher operating temperature around 900°C, HTGR adopts Helium as its cooler. As an inert gas, helium does not react to graphite and other reactor components which make it one of the determinants in their inherent safety concept.

Base on the Generation IV International Forum (GIF) system arrangements and memoranda of understanding as of January 2014, China, Europe Union, France, Japan, South Korea, Switzerland and USA are the active countries doing research on HTGR as the part of Generation IV reactor development [9]. GIF has also agreed on two types of HTGR designs, prismatic and pebble beds as the standard basis of Generation IV HTGR technology. The major difference between them is only in their core design. The prismatic core design is arranged exactly like GCR which consists of fuel pellets which are inserted into the cladding and then put in such a way in a graphite block arrangement in a pressure vessel reactor. In the other side, pebble bed type HTGR has a hollow core that is reinforced by the structure of graphite and reactor pressure vessels on the outside. The fuel itself is shaped like tennis balls and are inserted into the hollow core. Unlike the prismatic type whose fuel is replaced within a certain period of time and requires the shutdown condition, the pebble bed reactor has an online fuelling capability where the pebble fuel experiences rotation in several rounds until it actually becomes spend fuel. Both designs also have control of reactivity that can be inserted in a hole located in the side of the reflector. As a backup, several spherical reactivity controls are also prepared to force shut down the reactor.

Although has different core design, both of prismatic and pebble bed HTGR using similar fuel, moderator and cooling concepts. Both HTGR types use Tristructural-isotropic (TRISO) spherical fuel particle as the smallest part of its fuel component. Graphite is used as the neutron moderator, reflector also has the function as the core structure. Helium gas is chosen as the cooling system because of its inert characteristic that will able to minimize the degradation because of the chemical reaction between core components with the cooler. The combination of TRISO fuel, graphite moderator and helium

create an inherent safety design that is the main requirement of the Generation IV nuclear reactor. The similarity and differences between those design furthermore can be seen in Fig. 1.

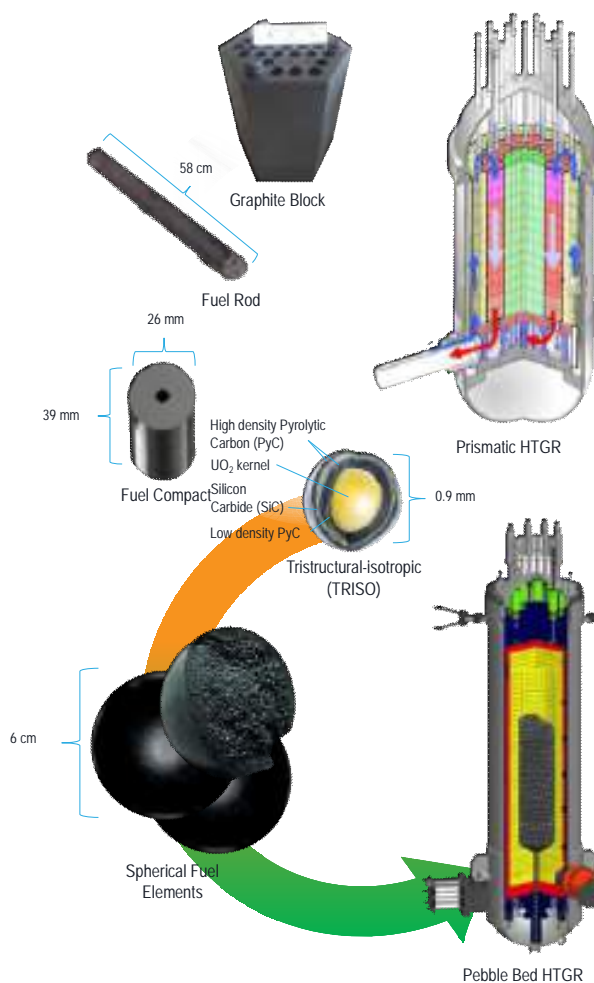


Fig. 1 Pebble bed reactor design and prismatic reactor design

The main purpose of nuclear safety is to protect humans and the environment from the potential of ionizing radiation risk [10]. To achieve this goal, there are three fundamental safety functions in the nuclear reactor must be followed, including controlling reactivity, heat removal and radioactive confinement [11]. Those fundamental safety functions are also followed by HTGR design.

As the part of inherent safety feature, TRISO fuel of HTGR consist of low enrichment uranium or plutonium. The fission material is coated by three-layer, high-density Pyrolytic Carbon (PyC), low-density PyC, and Silicon Carbide (SiC) with the size only about 0.9 mm. Low density with high porosity PyC layer able to capture almost all the fission products. The next layers consist of high-density PyC and SiC become the next deterrent against the release of fission products. The use of large amounts of graphite material both in the TRISO fuel layer and as a moderator neutron, the reflector and also the structure gives negative reactivity coefficient, low power density, and high thermal conductivity characteristics. All of these characteristics cause the reactor temperature to never exceed the predetermined threshold even without inserting control rod [12]. The characteristics of helium that are not easy to react reduce the potential for core degradation due to corrosion and explosive gas generation as can occur in a water-cooled reactor. Based on numerical and experimental studies, even station blackout or loss of cooling accident, decay heat removal process is capable to keep the fuel from exceeding its design temperature limit [13] [14].

Although control rod is not too important as the safety system because of its inherent safety

capability, it is still needed to control the reactor power base on the demand. Both prismatic and pebble bed HTGR use B₄C material as their control rod that can be inserted on the hole beside the reflector. In the case of loss of cooling accident, the core reactor power and temperature will become transient below the safety limit [12]. As the backup, control rod is possibly needed to return the reactor back to normal condition faster and avoid component degradation due to excessive temperatures exposure. The backup reactivity control of prismatic HTGR is designed base on B₄C pellets that can be inserted into the channels bored in the control rod blocks. The pebble bed HTGR be equipped with B₄C pebbles that can be inserted as the reactivity control backup system.

Prismatic and Pebble Bed type HTGR has their own advantages and disadvantages, but to maintain inherent safety design integrity, both usually designed no more than 600 MWth. In the other side, although Pebble Bed HTGR has the capability to do online refuelling, some studies argue that friction on its fuel management system makes the limitation on the suitable design of Pebble Bed HTGR become no more than 250 MWth for each reactor core. Friction between pebble during the operation was reported has increased dust production which has the potential to shorten filter life on the cooling systems [15]. To archive better performance, some new HTGR supported technologies are still needed to be developed, such as fuel handling assembly, neutron start-up handling systems, helium gas compressor improvement, reserve shutdown system, helium gas leakage detector, helium gas handling, gas turbine technology, etc. [16]. Those developing technology should get special attention in the reliability study and regulation development.

3. Methodology

The ultimate purpose of our study is to establish appropriate safety graded approach of HTGR to support regulation development. For that purpose, we are doing some stage of study starting from literature study, applying current standards and guidance that usually used for LWR, developing new methodology if needed, and finally establishing and proposing the appropriate graded approach for the real graded approach examination.

This article is part of our preliminary study and because of that, the methods used are adopted directly from current IAEA publications. IAEA has published some standards, guidance and technical report for graded approach purposes. One of that publication is IAEA TECDOC 1740 regarding graded approach for management system requirements for nuclear facilities and activities. That publication discussing various types of graded approach techniques that can be followed according to their aims and objectives, starting from the simplest ones using logic diagrams, Total Quality Ranking, Failure Modes, Effects Analysis (FMEA), etc [17]. On this part of the study, we will only be applying two of them, simply applying the logic diagrams provided by that publication, and utilising FMEA technique supported by FMEA standard IEC 60812.

Logic diagram like can be seen on Fig. 2 will be used as the first method to classifying HTGR Systems Structures and Components (SSCs) become four classes, safety class 1 as the highest important SSCs, safety class 2 as the important SSCs, safety class 3 as the less important SSCs and the last class 4 as the non-safety related SSCs.

Base on IEC 60812 standard, there are some stages should be done to do safety graded approach by using FMEA, but mainly can be classified become two, the analysis of FMEA itself by using an appropriate table, and doing critical analysis qualitatively by using Risk Priority Number (RPN) or quantitatively by using Criticality Number [18]. Based on the standard, FMEA analysis should be carried out in a group of experts. But due to limited resources and in its purpose in fulfilling the objectives of the study, the analysis is only done in a limited study group with a small number of SSCs. After completing the FMEA analysis we had chosen RPN instead of Criticality Number to calculate the safety graded approach. This is because the calculation of RPN is much easier than the calculation of Criticality Number. On some perspective, Criticality Number is better than RPN but the detail of failure rate, failure mode and operation time of each SSCs shall be known. As the new technology, reliability data for HTGR is very limited and only available for some generic components that make Criticality Number calculation become less suitable for this purpose. In the other side, qualitatively graded approach by using RPN is very simple by multiplying between Occurrence (O), Severity (S) and Detectability (D).

$$RPN = O \times S \times D$$

Before calculation, firstly, Occurrence, Severity and Detectability ranking shall be established on the same grade, for example by using 10 scales like can be seen in Table 1, 2 and 3 that are adopted from IEC 60812 [18] and US Army FMEA Guidance [19]. The other scale also can be used as long as between Occurrence, Severity and Detectability has the same scale.

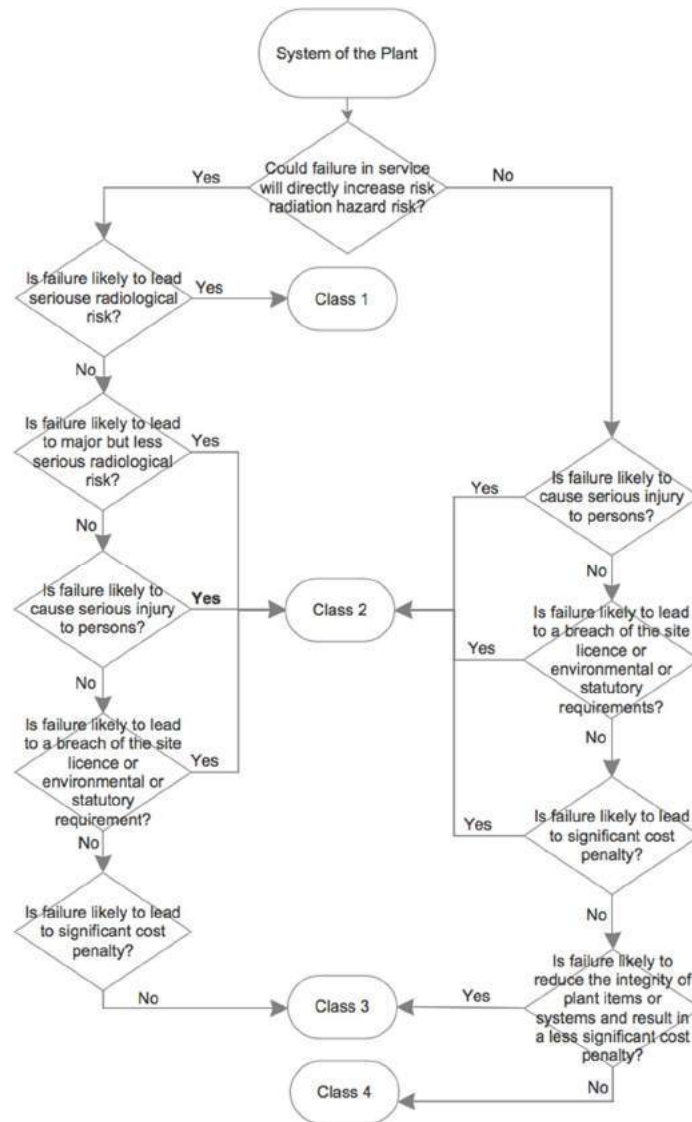


Fig. 2 NPP SSCs safety classification method [17]

Table 1 Occurrence classification

Ranking	Probability	Comments
1	$\leq 1 \times 10^{-5}$	Remote probability of occurrence; unreasonable to expect failure to occur
2	1×10^{-4}	Very low failure rate. Like past design that has, had low failure rates for given volume/loads
3	5×10^{-4}	Low failure rate based on similar design for given volume/loads
4	1×10^{-3}	Occasional failure rate. Like past design, had similar failure rates for given volume/loads
5	2×10^{-3}	Moderate failure rate. Like past design having moderate failure rates for given volume/loads
6	5×10^{-3}	Moderate failure rate. Like past design having moderate failure rates for given volume/loads

7	1×10^{-2}	High failure rate. Like past design having frequent failures that caused problems
8	2×10^{-2}	High failure rate. Like past design having frequent failures that caused problems
9	5×10^{-2}	Failure is almost inevitable
10	$\geq 1 \times 10^{-1}$	Very high failure rate and almost certain to cause problems

Table 2 Severity classification

Ranking	Effect	Comments
1	None	No discernible effect
2	Very minor	Effect of failure nearly negligible
3	Minor	Failure only cause minor problem on the part(s) of SSC
4	Very low	Local problem maybe occurs but do not affect the operation
5	Low	Item operable but comfort item(s) operable at a reduced level of performance.
6	Moderate	Item operable but comfort/convenience item(s) inoperable.
7	High	Item still operable but level of performance is decrees.
8	Very high	Loss of primary function of SSC
9	Hazard with warning	Very high severity ranking when a potential failure mode affects safe SSC operation and/or involves non-compliance with government regulation with warning
10	Hazard without warning	Very high severity ranking when a potential failure mode affects safe SSC operation and/or involves non-compliance with government regulation without warning.

Table 3 Detectability classification

Ranking	Detection probability	Comments
1	1/10+	Very easy to be detected and usually accurate
2	1/20	Easy to be detected and accurate
3	1/50	High to moderate detectability
4	1/100	Moderate detectability
5	1/200	Moderate to low detectability
6	1/500	Low detectability
7	1/1000	Able to be detected with low accuracy
8	1/2000	Hard to be detected and usually not accurate
9	1/5000	Very hard to be detected and usually not accurate
10	1/100000	Almost impossible to be detected

As the linguistic term, the ranking of Occurrence, Severity and Detectability can be judged by an expert or group of experts easily. Regardless the issues of traditional FMEA which will be discussed later, as the part of this study methodology, RPN FMEA graded approach is implemented as it is like what has been described on the IEC standard and US Army guidance.

4. Result and Discussion

The biggest problem on the HTGR SSC safety graded approach is caused by the availability of the reliability data of each SSC. Based on several kinds of literature there are many reliable methods that can be used for this purpose, such as Fault Tree Analysis (FTA), Reliability Block Diagram (RBD), Bayesian Network, Petri Net, etc. Especially FTA is a mature technique and widely implemented for the nuclear industry. Safety graded approach can be done easily base on FTA by deploying important index concepts, such as by using Birnbaum, Fussell-Vesely, Risk Achievement Worth, and Risk Reduction Value. But the main problem in applying this technique is in the availability of quantitative data. All data reliability of the SSC must be known to calculate the important index. On the other hand, as already mentioned in the methodology above, the qualitative FMEA RPN and logic diagram are one of the few techniques that can be used for safety graded approach and classification without requiring the availability of quantitative data. That is one of the reasons why RPN FMEA is one of the best techniques for technology that is being developed like HTGR.

Even though Prismatic and HTGR pebble beds have the same basic concepts, but because they

have different designs, of course, they also have several different SSCs. To avoid ambiguity and to simplify the study, this graded approach is carried out especially based on High Temperature Engineering Test Reactor (HTTR) design that has been established by the Japan Atomic Energy Agency [20] [13]. HTTR is the prototype of prismatic type HTGR that expected will become the basic technology of the future Japanese commercial HTGR. Simplification of study is also doing by limiting the number of analysed SSCs only for 36 items. But for the real purposes and to get the more realistic result, more detail study by breakdown each SSCs become sub-system, components and parts is needed.

By using the classification methodology in Fig. 2, we found that only 5.6% of SSCs can be categorized as class 1. Most of them, about 64.0% can be classified as class 2, 19.4% class 3 and 11.0% class 4. Fuel and graphite moderator as part of the core structural components become safety class 1. Primary cooling systems, electricity facilities, control system, etc. that usually become safety class 1 on LWR become class 2 on HTGR. Each safety class has meaning as follows. Class 1 is all SSCs that could lead directly to the increase in the radiological hazard risk and is likely to lead to a serious radiological risk. Class 2 is for the SSCs that their failure is likely to lead to major problems, serious injury to persons, lead to significant cost penalty, or lead to a breach of the site license or environmental or statutory requirements but less serious radiological risk. Class 3 is for SSCs that the failure is likely to reduce the integrity of plant items or systems and result in a less significant cost penalty. And the class 4 SSCs is for all of the SSCs that are not quite important from the side view of class 1, 2 and 3.

FMEA analysis has been carried out using the Table 4 that is adopted directly from IEC 60812 standard. To shorten the article, detailed analysis of FMEA is not displayed on this article. After overall SSCs used as study objects are analysed carefully, then criticality analysis has been carried out by adding additional columns on the right side of FMEA analysis sheet as a place to add values for occurrence, severity and detectability for each SSC based on Table 1, 2 and 3. Finally, the RPN of each SSC can be calculated by multiplying those values. The RPN of each SSC and combined with the result of logic diagram classification methodology can then be shown graphically in Fig. 3.

Table 4. FMEA Analysis Sheet

Item ref.	Item description and function	Failure mode	Failure mechanism	Possible failure causes	Local effect	Final effect	Detection method	Compensating provision against failure	Remarks
1.0	Fuel as the main source of fission energy generation	Rupture of TRISO structure	Crack, oxidation, fracture, etc.	Lack of production or quality control/quality assurance	The release of FPs from TRISO structure to graphite fuel compact structure	Increase the release probability of FPs	Batch quality control method on the production and almost impossible to be detected on the operation	Capturing FPs by multiple barriers. If TRISO failure, will be captured by fuel compact, then by fuel rod, graphite block, primary cooling system, etc.	Failure fraction less than 10-4. Major failure begins an about 2200° C and 100% failure at 2400° C. The main radiation release from spent fuel only gamma and neutron.
1.1		Graphite fuel compact degradation	Crack, oxidation, fracture, etc.	Thermal/seismic/chemical shock and degradation	Fuel compact degradation may be causing swelling of the fuel rod, increasing dust	Increase the probability of FPs release and dust on the cooling system	Almost impossible to be detected on the operation, but able to be detected on production and after the operation	If degradation of fuel compact is followed by degradation of previous FPs barrier, then fuel rod or graphite block and another barrier should capture the FPs.	Small fuel compact degradation will give significant impact on safety
1.2		Swelling/rupture/degradation of fuel rod	Ununiform changing of micro and macrostructure	Thermal/seismic/chemical shock and degradation	Stuck of fuel rod on the graphite block	Fatal swelling might cause difficulty in refuelling or maintenance activities	Almost impossible to be detected on the operation, but able to be detected on production and after the operation	Graphite block is designed impermanent that make if something happens with fuel rod, entire graphite block moderator can be moved out.	Although problem on swelling of fuel rod can be handled by moving out the graphite block, it will take longer refuelling time and possible increase the FPs release and radiation exposure

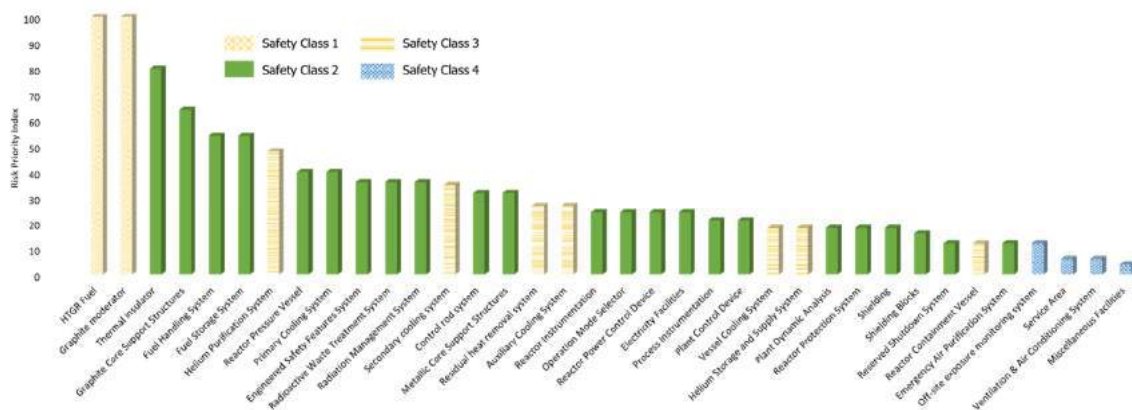


Fig. 3 HTGR SSCs Graded Approach & Classification

Base on RPN calculation, fuel and graphite moderator structure become the most important components considering these components are the key to inherent safety design and become the first and most important fission products barrier. Fuel and graphite moderator then followed by graphite core structure and reactor pressure vessel as the part of core structure become the top most important safety components that should get special attention. Although helium as the coolant also gives the contribution to inherent safety but based on some experiment, the loss of cooling accident will never cause reactor meltdown [12] [14] [21]. Loss of coolant will only effect on the increase of core temperature and the release probability of the fission products. Because of that, cooling systems have not become the topmost safety priority.

However, like can be seen in Fig. 3, the results between the safety classification based on the logic diagram and the RPN FMEA looks not match. This is perhaps because of ambiguity between serious with less serious radiological risk and the licence or statutory requirement on the logic diagram. For example, is redundancy engineered safety systems that become mandatory for LWR. Theoretically, HTGR safety is based on an inherent safety feature that does not have the potential to lead serious radiological hazard if the quality and integrity of inherent safety feature related components are well-preserved. Thus, the main concern must be given to quality control and quality assurance of fuel and core components integrity. As part of the defence in depth and multiple barriers, of course, some safety system function should be prepared. But on the other side that systems should not become overprotective because could increase the overall cost. Based on the pre-feasibility analysis of HTTR, the containment vessel requirement is one of the safety components that possibly can be reduced for the future development because its construction was very costly, but the function looks not too important. Deeper study regarding the possibility of eliminating some HTGR engineered safety features that are currently subject of regulation is needed.

The inconsistency result of those methods is possibly also caused by the limitation of RPN FMEA method itself. As mentioned in IEC 60812, traditional FMEA has several disadvantages, such as the similar weighting between occurrence, severity & detectability cannot provide adequate risk sense, 88% of RPN range is empty (only 120 from 1000 that used) and inadequate RPN scaling with very sensitive with small changes [18]. As a qualitative graded approach, RPN that relies on expert judgment also cannot be separated from two types of uncertainty, epistemic uncertainties and aleatory uncertainties. Lack of knowledge uncertainties arising because our imperfect scientific understanding (epistemic) and uncertainties that for all practical purposes cannot be known in detail or cannot be reduced (aleatory) and combined with the shortcomings of traditional RPN calculations will able to produce graded approach result with very high uncertainty. In the other side, there are also several problems on the expert judgment, such as its very difficult to find a universal expert for all aspect of HTGR technology, every expert has their own subjectivity, and when multiple experts will be used, special treatment should be conducted to catch the “true value”.

To overcome those problems, we are developing a new methodology that is expected able to solve the used of expert judgment and traditional RPN issues. Some studies have been well conducted to solve traditional RPN issues such as by utilizing a database, using mathematical also psychological

approach [22]. From those methods, we feel fuzzy logic theory is good enough to be used to solve traditional FMEA deficiency. Fuzzy logic theory able to work as well as human thinking which is not only based on right and wrong, black and white, or other opposite values. RPN is qualitative graded approach where the judgment is given in the form of linguistic terms. Linguistic terms often have the meaning in the "grey area" between two opposite values. The advantages of fuzzy logic are that it can transform qualitative values into quantitative ones by reaching that grey area. To answer the uncertainty problems from the use of expert judgment, there is also a various method that has been developed by researchers, including behaviour aggregation methods and mathematical aggregation methods [23]. After reviewing each of these methods, we argue that there are several expert judgment aggregation methods that should be used for HTGR graded approach. Behaviourally, the Delphi method by allowing experts to communicate with each other but with some filters is the best. Mathematically, if the "true value" of the evidence cannot be captured by consensus, then fuzzy weighting method should be used. In case there is a "true value" but new robust evidence is available, then Bayes belief theory should be applied.

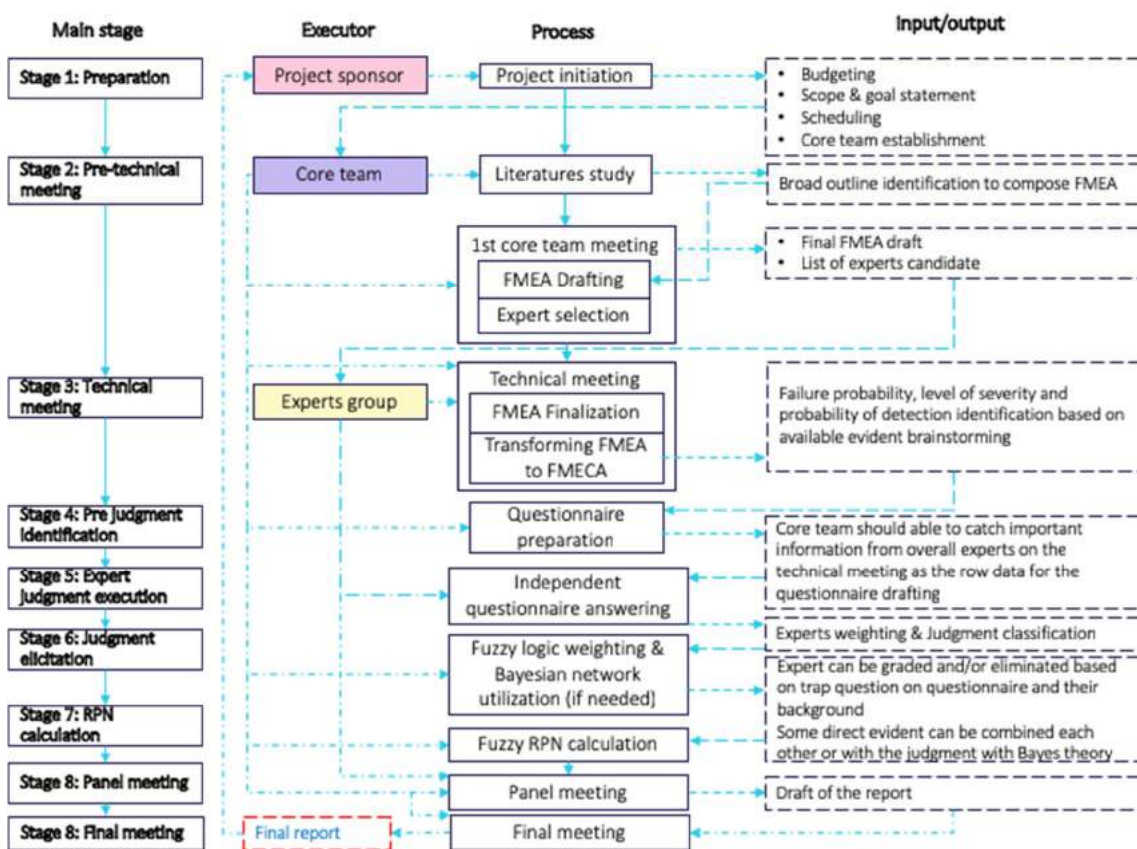


Fig. 4 Proposed Methodology for HTGR Graded Approach

Currently, we are working to do exercise by implementing proposed methodology like can be seen in Fig. 4 for some HTGR SSCs. The major differences on this proposed methodology are located on how "true value" of occurrence, severity and detectability can be captured from multiple experts based on the level of evidence and agreement, also on how to calculate RPN base on fuzzy logic theory. Considering the scope and objective, in this article, we will not discuss this proposed methodology deeply. We would like to discuss it on the other article after all the studies including verification and validation are complete.

5. Conclusion

There are some differences of HTGR safety paradigm impacted on the safe operation &

maintenance activities and make some modification on the current standards & regulations is needed. The main difference is caused by the inherent safety feature that makes it be the first and foremost foundation in safe operation and maintenance activities. By using classification and graded approach methodologies commonly used for LWR, trial graded approach for some HTGR SSCs have been carried out. From that exercise, fuel, graphite structure and core components of HTGR have the highest ranking. But by comparing between classification by using logic diagram and RPN FMEA methodologies, there is some inconsistency that indicates some issues that should be solved. We argue that both the logic diagram and the traditional RPN that we used in this study are too weak to be able to be applied in the HTGR graded approach. Therefore, we are proposing a new method that the validation process and sensitivity analysis is being carried out.

Acknowledgements

The authors give many thanks to Dr Shoji Takada, Dr Etsuo Ishitsuka, and all member of High Temperature Engineering Test Reactor (HTTR) department, Japan Atomic Energy Agency (JAEA) Oarai that have given their support, help and opportunity to learn HTGR technology more deeply from the lessons learned from current High Thermal Test Reactor (HTTR). Some data and perspective we used on this article are based on the discussion that we got from them.

We also give special thanks to the anonymous reviewer for their valuable comment until this article can be published.

References

- [1] International Atomic Energy Agency, "Nuclear Power Reactors in the World," Vienna, 2018.
- [2] International Energy Agency, "World Energy Outlook 2017," *Int. ENERGY AGENCY Together Secure. Sustain.*, 2017.
- [3] G. Zhao *et al.*, "Endurance test of full-scale mock-up helium circulator for HTR-PM," *Nucl. Eng. Des.*, vol. 329, no. April 2017, pp. 20–24, 2018.
- [4] China Nuclear Energy Association, "China's Nuclear Energy Guide 2017," Beijing, 2017.
- [5] Y. Zhou, C. Rengifo, P. Chen, and J. Hinze, "Is China ready for its nuclear expansion?," *Energy Policy*, vol. 39, no. 2, pp. 771–781, 2011.
- [6] World Nuclear Association, "Nuclear Power Economics and Project Structuring," London, 2012.
- [7] I. W. Ngarayana, T. Do, K. Murakami, and M. Suzuki, "Nuclear Power Plant Maintenance Optimisation : Models, Methods & Strategies," Manuscript submitted for publication, 2018.
- [8] B. J. Marsden and G. N. Hall, *Graphite in gas-cooled reactors*, vol. 4, no. April 2015. 2012.
- [9] I. Pioro, Ed., *Handbook of Generation IV Nuclear Reactors*, Woodhead P. Duxford, UK: Elsevier, 2016.
- [10] International Atomic Energy Agency, "Fundamental Safety Principles," *Safety Fundamentals*, vol. 2, no. No.SF-1. p. 37, 2006.
- [11] International Atomic Energy Agency (IAEA) - NS-R-1 and International Atomic Energy Agency, *Safety of Nuclear Power Plants: Design (NS-R-1)*, vol. 1. 2016.
- [12] S. Nakagawa, K. Takamatsu, Y. Tachibana, N. Sakaba, and T. Iyoku, "Safety demonstration tests using high temperature engineering test reactor," *Nucl. Eng. Des.*, vol. 233, no. 1–3, pp. 301–308, 2004.
- [13] T. Nishihara, X. Yan, Y. Tachibana, and T. Shibata, "Excellent Feature of Japanese HTGR Technologies," Tokai-mura, 2018.
- [14] K. Takamatsu *et al.*, "Experiments and validation analyses of HTTR on loss of forced cooling under 30% reactor power," *J. Nucl. Sci. Technol.*, vol. 51, no. 11–12, pp. 1427–1443, Dec. 2014.

- [15] P. W. Humrickhouse, “HTGR Dust Safety Issues and Needs for Research and Development,” Idaho, 2011.
- [16] Y. Shimazaki, F. Homma, H. Sawahata, T. Furusawa, and M. Kondo, “Development of the maintenance technologies for the future high-temperature gas cooled reactor (HTGR) using operating experiences acquired in high-temperature engineering test reactor (HTTR),” *J. Nucl. Sci. Technol.*, vol. 51, no. 11--12, pp. 1413–1426, 2014.
- [17] International Atomic Energy Agency, “Use of a Graded Approach in the Application of the Management System Requirements for Facilities and Activities.” IAEA, Vienna, 2014.
- [18] Commission International Electrotechnical, “IEC 60812: Analysis Techniques for Reliability - Procedure for FMEAs.” International Electrotechnical Commission, Geneva, 2006.
- [19] Department of the US Army, “Failure modes, effects and Criticality Analysis (FMECA) for command, control, computer, intelligence, surveillance and reconnaissance (C4ISR) Facilities,” *US Army*, no. September. US Army, Washington, p. 75, 2006.
- [20] JAERI, “Design of high temperature engineering test reactor (HTTR),” JAERI, Tokai-mura, 1994.
- [21] Y. Fujiwara, T. Nemoto, D. Tochio, M. Shinohara, M. Ono, and S. Takada, “Loss of Core Cooling Test With One Cooling Line Inactive in Vessel Cooling System of High-Temperature Engineering Test Reactor,” *J. Nucl. Eng. Radiat. Sci.*, vol. 3, no. 4, p. 041013, 2017.
- [22] C. Spreafico, D. Russo, and C. Rizzi, “A state-of-the-art review of FMEA / FMECA including patents,” *Comput. Sci. Rev.*, vol. 25, pp. 19–28, 2017.
- [23] K. J. Wilson, “An investigation of dependence in expert judgement studies with multiple experts,” *Int. J. Forecast.*, vol. 33, no. 1, pp. 325–336, 2017.

(Received: 3 October 2018, Accepted: 14 February 2019)

Galet – Geant4 Based Application Templet for Primers

Tsukasa Aso^{1,*}, Wataru Takase², Takashi Sasaki²

¹⁾*Department of Electronics and Computer Engineering, National Institute of Technology, Toyama College, 1-2 Nariya Ebie, Imizu 933-0293, Japan*

²⁾*Computer Research Center, High Energy Accelerator Organization, 1-1 Oho, Tsukuba 305-0801, Japan*

**E-mail: aso@nc-toyama.ac.jp*

Geant4 is a Monte Carlo simulation toolkit to simulate interaction of particles with matter. It has been designed and implemented on objected-oriented technique and C++ programming language. Since Geant4 is distributed as a toolkit, users need to develop their Geant4 applications by themselves. Therefore, the users are required enough expertise about software engineering as well as particle physics. However, many of beginners of Geant4 are not easy to satisfy these requirements. For the purpose of minimizing users' efforts in software developments, Geant4 based application templet (Galet) has been proposed. Galet is a skeleton program to be utilized as a primary code for integrating users' applications. It provides versatile and reusable concrete classes for various applications. In case of the minimum implementation, Galet requires to implement only three classes that are relevant to construction of simulation geometry and scoring of simulated results. Galet was applied to several applications in various field. The efficiency and effectiveness of Galet were verified through those applications.

1. Introduction

Geant4 [1-3] is a general-purpose Monte Carlo simulation toolkit to simulate the passage of elementary particles through and interacting with matter. It provides complementary physics models of particle interactions such as electromagnetic physics, hadronic and nuclear physics, optical photon physics. The energy scale covers ranging from a few eV to TeV. Therefore, it is widely used in various science field such as high energy physics, nuclear physics, space engineering and medical physics. Geant4 has been designed on the object-oriented technology (OOT) and implemented in C++ programming language. The source codes are distributed as a toolkit under the Geant4 software license. The concept is openness that make the design and implementation of the physics open and transparent for users. The toolkit consists of a series of class libraries, in which the classes are designed in a highly reusable and a suitable granular level so that users can customize and replace parts of implementations with their extended components according to the specification of their applications. Such design allows users to incorporate the Geant4 within their own computational framework as well as to develop stand-alone applications. The toolkit approach is one of unique features in Geant4 in comparison with the other Monte Carlo simulation projects [4,5] in which the simulation code is provided as an application program.

The toolkit approach offers many advantages in application developments, however, it requires users to develop their application program by themselves. The users are expected to be experts about software development in OOT and C++ programming. These requirements are regularly acceptable when we assume a large project such as high energy physics experiments. In the project, software group usually consists of experts of Geant4 application developments. The software group designs and develops a specific application program as a simulation framework for the experiment. Many end-users in the project use it for their physics and detector analysis. Eventually, the software group maintains and upgrades the simulation framework by referring feedback from end-users. Same kinds of approach can be seen in medical physics domain such as PTSIM[6] and TOPAS projects [7]. These projects developed the

simulation frameworks for radiation therapy on the collaboration of Geant4 experts and medical physicists. These frameworks have been distributed to many radiation facilities for quality assurance of beam delivery system and dose calculations.

Due to the extendibility and reliability of Geant4, there is growing desire to use Geant4 in not only the large projects but also small projects such as laboratory scale experiments. The in-house simulation tool in small projects will usually have moderate complexity and have rather short lifetime, because the tool will be frequently modified according to the stage of project for applying various analysis methods and/or optimized experimental setups. Unlike to the large projects, developing an in-house simulation tool has to be conducted by end-users without supports from Geant4 experts. In the situation, the end-users are required to serve as Geant4 experts. However, such end-users are not easy to satisfy the requirement, because they are usually beginners of Geant4.

For the purpose of assisting beginners to develop in-house Geant4 applications, the Geant4 application templet (Galet) has been proposed, which is a skeleton program of Geant4 application. In this paper, firstly the brief concepts, design and implementation of Galet are described. Secondly several example applications based on Galet are introduced as practical examples.

2. Methods

2.1 Concepts

The use-case of Galet was defined for an in-house Geant4 application development. We assumed that the end-users develop in-house Geant4 applications by themselves, and they are beginners about Geant4 and OOT software engineering.

Geant4 has many virtual classes to be mandatory implemented for the application. Developing a typical example application requires users to prepare concrete classes in C++ code for defining materials, geometries of simulation space, primary particle conditions, physics processes to be applied for interactions of particles with matter, and scoring functions. These user codes need to be developed on the virtual classes of Geant4 and registered into the application as shown in Fig. 1.

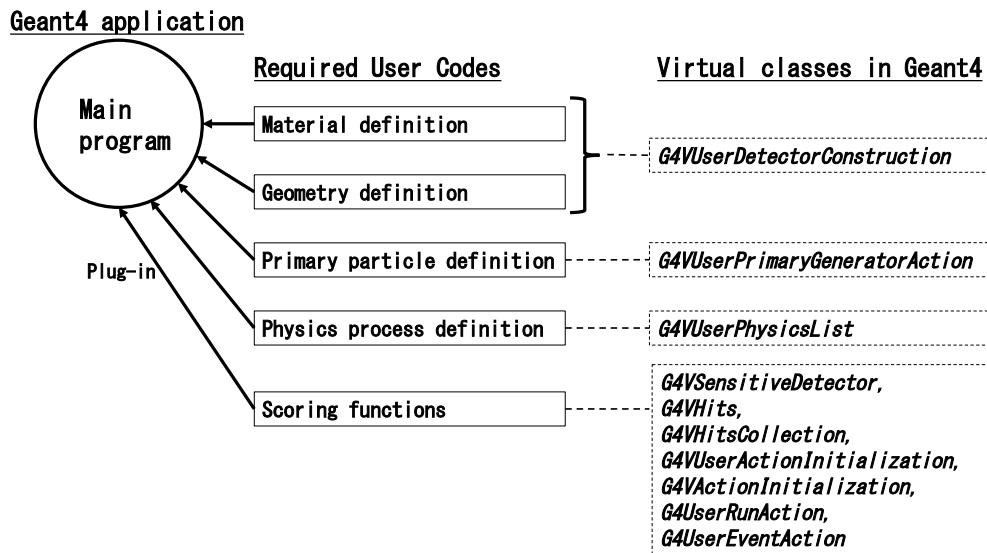


Fig. 1 Schematic diagram about user codes and its virtual classes in Geant4 required for typical Geant4 application development.

Among these virtual classes, only the minimum number of classes should be chosen to be implemented by users, while the other virtual classes should be provided as general-purpose concrete classes in Galet. On this concept, Galet offers users to focus on implementing the experimental geometry setup and the scoring function according to their purpose of simulation, so that the results can be easily achieved in a straightforward way.

For example, the scoring function needs to implement seven classes relating to many stages in the simulation process. Figure 2 shows a schematic view of particle transport in Geant4. A particle is

tracked in the simulation space with steps. Here the step point is determined according to geometrical interfaces and physics interactions. The track information such as particle momentum and position at step is obtained in class `G4VSensitiveDetector` from `G4Track` and `G4Step` instances of Geant4. Since track information in these instances is overwritten in every step, some of the information has to be saved into an instance of class `G4VHit`. Then, the `G4VHit` instance needs to be stored temporary into a collection class `G4VHitsCollection` for later use to calculate physics quantities. Usually, class `G4UserEventAction` is used for calculating physics quantities such as particle flux and total absorbed energy per one primary particle, in which the calculations need all track information including secondary particles in the event. For the purpose of optimizing the simulation efficiency, Geant4 is designed to be capable of calculating such physics quantities directly in classes `G4VSensitiveDetector` and `G4VHit`. However, such optimized implementation usually causes strong dependence on the other classes in the application. Therefore, Galet adopts to provide general-purpose classes of them to store the original track information and postpone the physics quantity calculations at the end of a history in class `G4UserEventAction`. Although, this strategy may have some disadvantages in terms of computational efficiency, however, it is very advantageous at the point of easiness in application developments.

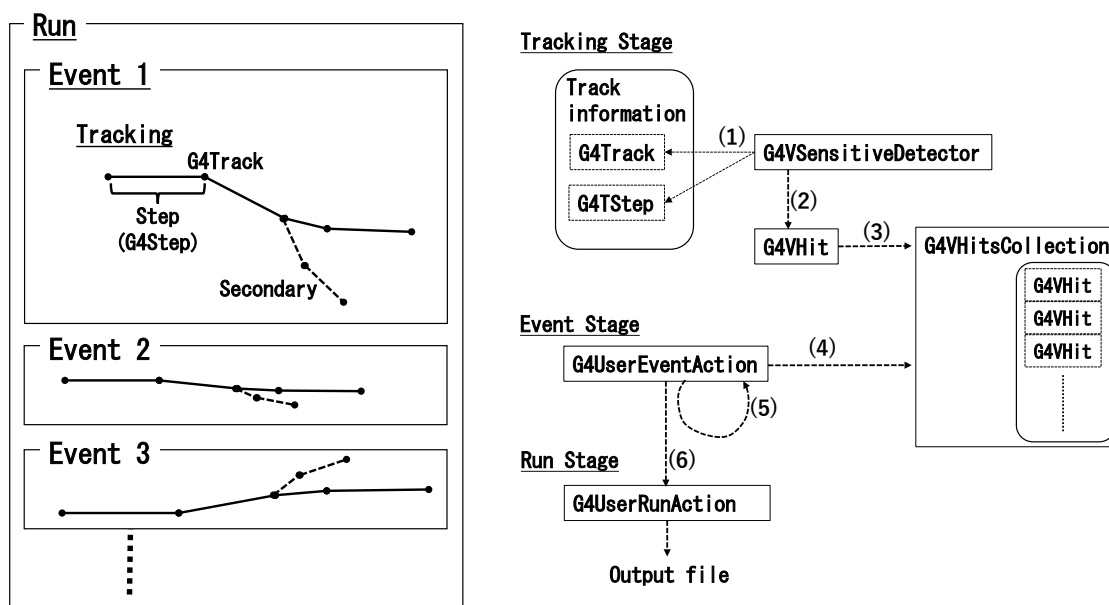


Fig. 2 Overview of simulation stages and the scoring process in Geant4. The stages are categorized to Run, Event and Tracking (left). The tracking stage consists of steps in particle transport. Scoring is processed with virtual classes in Geant4 (right). The scoring process is briefly described as follows. Tracking stage: (1) getting track information from a step, (2) creating a hit instance, and (3) storing the hit instances into a hits collection. Event stage: (4) getting the hit instances from the hits collection, (5) calculating physical quantities from the hit instances, and (6) compiling the physical quantities for events. Run stage: Output the physics quantities to a file.

The users will use Galet as a primary code of Geant4 application developments, and some of them will become experts of Geant4 in future. In order to utilize Galet as a primer of Geant4, Galet exactly follows the manner of Geant4 application development without veiling or replacing original Geant4 functions. This policy also implies that all kinds of modules in Geant4 are acceptable for plug-in so that the product becomes a sophisticated Geant4 application.

2.2 Design and implementation

According to the defined concepts, Galet was developed as a skeleton program of Geant4 application. The virtual classes in Geant4 and the corresponding concrete classes in Galet are listed

in Table 1 for regular application development. In the table, the virtual classes are indicated with italic characters, while the other classes are concrete classes. The three classes with bold characters in Galet stand for skeleton classes that have to be partly implemented by users. The class GaletDetectorConstruction is used for describing a simulation geometry. The classes GaletRunAction and GaletEventAction are used for describing functions of scoring and recording simulation results, in which the former and latter classes are used to define and fill histograms with calculated physical quantities. The minimum application is usually realized by implementing these three classes. In consequence, users are able to efficiently develop their applications by focusing on the simulation geometry and the physical quantities to be achieved.

Table 1 Class relationship between Geant4 and Galet

Geant4 virtual classes	Galet classes
<i>main</i>	Galet
<i>G4VUserPrimaryGeneratorAction</i>	GaletPrimaryGeneratorAction
<i>G4VUserActionInitialization</i>	GaletActionInitialization
<i>G4VUserPhysicsList</i>	GaletPhysicsList GaletPhysicsListMessenger
<i>G4VUserDetectorConstruction</i>	GaletDetectorConstruction GaletDetectorConstructionMessenger GaletMaterialFileConstruction GaletMaterialFileMessenger
<i>G4VUserActionInitialization</i>	GaletActionInitialization
<i>G4UserRunAction</i>	GaletRunAction
<i>G4UserEventAction</i>	GaletEventAction
<i>G4VSensitiveDetector</i>	GaletSD
<i>G4VHit</i>	GaletHit
<i>G4VHitsCollection</i>	GaletHitsCollection

In addition to these three classes, simulation conditions for a primary particle generator, physics processes, geometries and materials have to be defined. Galet provides concrete classes for this purpose. Those classes are designed to be versatile and reusable for various applications, and implemented with messenger classes to provide user-interface (UI) commands. Therefore, the configurations can be changed by using UI commands without modifying the source code.

Galet uses G4GeneralParticleSource (GPS) of Geant4 for primary particle generator in class GaletPrimaryGeneratorAction. The GPS provides variety of UI commands to specify primary particle parameters. For example, energy spectral, spatial and momentum distributions of primary particle can be flexibly assigned to configure primary source conditions.

The classes for physics-list registration and material definition are taken from PTSIM code. The physics-list defines a set of physics processes with the interaction types and models. The classes GaletPhysicsList and GaletPhysicsListMessenger configure the physics-list by registering physics constructors by using UI commands. The physics constructors are referred from the Geant4 referenced physics-list, in which the physics constructors are categorized as electromagnetic physics, hadron physics, radioactive decay physics, optical photon physics etc. In each physics category, several models are available. For example, the physics constructors of electromagnetic physics are available for standard, Livermore, Penelope and DNA models. The DNA model is an extension of electromagnetic physics that is applicable down to eV scale and water radiolysis. One of these models is chosen by users according to the specification of simulation.

The material definition is managed in classes GaletMaterialFileConstruction and GaletMaterialFileMessenger. Materials in NIST material database are created by specifying the material name in UI command. User-defined materials are also created by specifying the name of data file in which the recipe of material is described in ASCII format.

The scoring is the most complicated part of application developments for beginners, because it relates to geometry structure, physics processes and particle transports. The classes GaletSD and GaletHit are designed to be versatile enough for various applications. The instance of GaletSD will

be attached to the scoring volume in class GaletDetectorConstruction. When a particle track comes into the scoring volume, it creates and stores an object of GaletHit as a temporal memory of track information. Each instance of GaletHit memorizes track identification number, positions, time, particle identification number, kinetic energy, deposited energy, deposited dose, volume identification number, created physics process type, created position, step length etc. Any kinds of distributions and physics quantities needed for analysis can be derived from the information in GaletHit instances.

Galet uses the class G4AnalysisManager of Geant4 in classes GaletRunAction and GaletEventAction. The G4AnalysisManager is used for assembling simulation results into histograms and/or database. The output format is chosen from CERN ROOT Analysis tool, XML and CSV by compile option.

3. Results and Discussion

The usage of Galet has been tested on educational and research projects [8-12], in order to ensure efficacy and expendability of Galet in various application developments. Four example applications from those projects are introduced in following sections.

3.1 Galet-Edu

Galet-Edu stands for Galet for education in radiation simulation. Authors have been organizing the KOSEN-KEK summer internship for computing in radiation researches since 2016 by the support of Cooperative and Supporting Program for Researches and Educations in Universities in KEK. By 2018, total 18 KOSEN students have participated the internship and experienced a Galet application development. The students were from various departments such as electricity, machinery, electronics and computing. Although most of students had not experienced about Geant4 and C++ programming until the internship, the students could engage on developing a simulation of NaI(Tl) detector on Galet in one day practice as shown in Fig. 3.

They created materials of NaI(Tl) by mixing atoms according to mass fractions in literature, and implemented the simplified geometry of NaI(Tl) detector (Fig. 4) in class GaletDetectorConstruction. The primary particle was set to be Cs-137 and placed at a certain distance along to the coaxial line of the detector by using GPS commands. Instead of simulating scintillating photons, deposited energy in the NaI(Tl) crystal was simply accumulated to obtain the energy spectrum. In class GaletEventAction, the energy fluctuation of detector response was emulated by using a random generator of Gaussian distribution corresponding to the energy resolution of the detector, and taken account to the accumulated energy deposit per decay. The students performed simulations with various experimental conditions. Then the students analyzed the number of counts in the full energy peak in the spectrum by using CERN ROOT analysis tool. Figure 5 shows an example energy spectrum in NaI(Tl) detector simulation with the fitting result by Gaussian and exponential composite function.

Although these students were beginners of Geant4 and C++ programming language, they could develop a Geant4 application on Galet within one day practice. It implies that Galet is an efficient primary code to develop a simple Geant4 application for beginners.



Fig. 3 Snapshot of internship in 2018. Total of 8 students engaged on developing NaI(Tl) detector simulation based on Galet-Edu code.

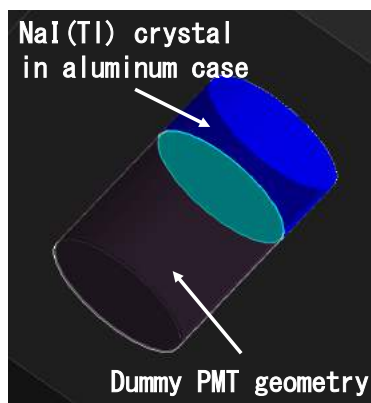


Fig. 4 Simple NaI(Tl) detector geometry in Galet-Edu including a NaI(Tl) crystal in aluminum case and a dummy photomultiplier tube (PMT).

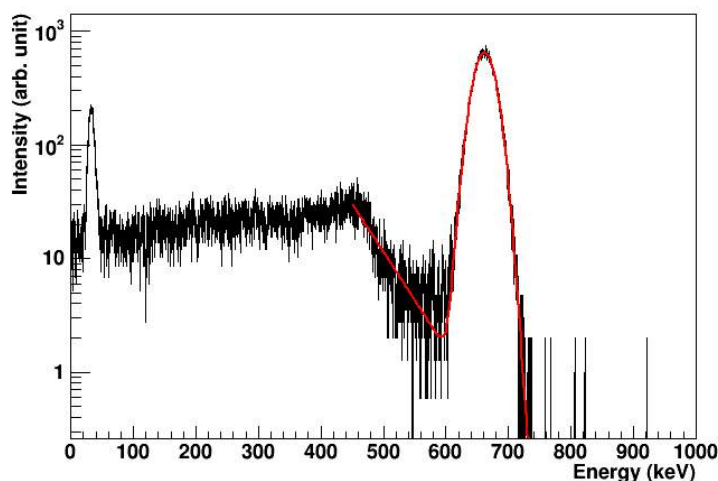


Fig. 5 Example energy spectrum of Cs-137 in NaI(Tl) detector calculated in Galet-Edu simulation. The red line shows a fitting result of the full energy peak.

3.2 Galet-HPGe

Galet-HPGe is a Galet application of high purity germanium (HPGe) detector. It was developed for verifying the conventional sum-peak method [13-15] and the modified sum-peak method [16,17] in radioactivity determination. These methods are absolute measurement techniques which can be applied to radionuclide emitting more than one gamma-rays in cascade.

Galet-HPGe simulation modeled a HPGe detector and a lead shielding box as shown in Fig. 6. The geometries were implemented in class GaletDetectorConstruction. The geometric parameters were taken from the datasheets of GMX-25190 Ortec. The HPGe is an open-ended coaxial photon detector of n-type. The HPGe crystal was specified as a scoring volume. In class GaletEventAction, the energy spectrum was calculated by accumulating the deposited energy in the scoring volume, and the energy resolution was taken into account according to the energy dependent response function obtained from measurements. Since the radioactive decay physics in Geant4 version 10.02 did not take into account the angular correlation between gamma-rays in Co-60 disintegration. We developed a primary generator to produce two gamma-rays according to the angular correlation function $\bar{w}(\theta)$ of Co-60 and replaced GPS with it in class GaletPrimaryGeneratorAction.

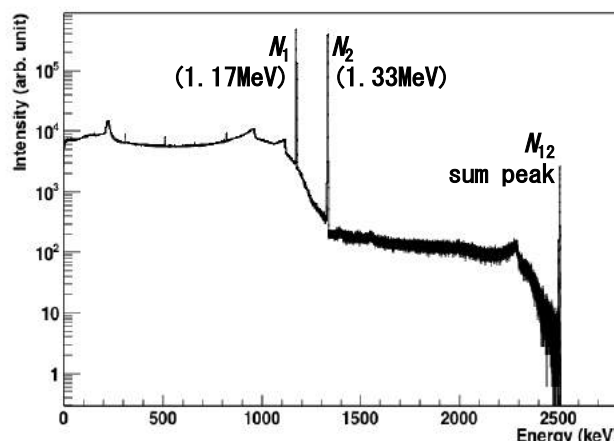
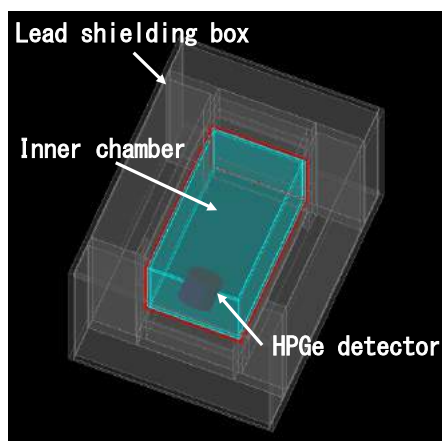


Fig. 6 Galet-HPGe geometry modeled a **Fig. 7** Example energy spectrum of Co-60 gamma-rays in HPGe simulation.

An example energy spectrum of Co-60 in the simulation is shown in Fig. 7. Here N_1 , N_2 and N_{12} in the figure stand for the number of counts in each full energy peak for 1.17 MeV, 1.33 MeV and sum peak, respectively. The simulation for a Co-60 point source was repeated by changing the source-to-detector (S-D) distance. The simulated results were normalized by assuming the actual number of decays to be 10,000. The modified sum-peak method is demonstrated in Fig. 8. The figure shows the dependence of $N'_0 = (N_1 N_2 / N_{12}) \bar{w}(0)$ on N_1 with $\bar{w}(0)=1.111$. The simulated points were fitted by a quadratic function and the number of decays was calculated as a value at the intersection of $N_1 = 0$. As shown in the figure, the calculated value is consistent with the actual number of decays in the simulation. The detail implementation and discussion about the verification of the modified sum-peak method are described in [8].

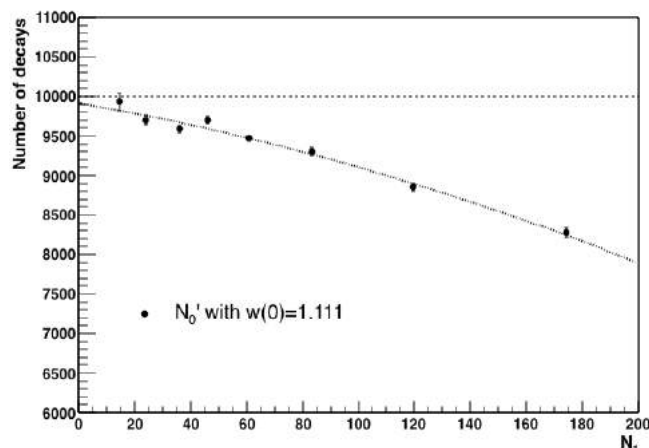


Fig. 8 Demonstration of the modified sum-peak method by using the results of Galet-HPGe simulation. The series of data points show the dependence of N'_0 on N_1 . The activity is calculated as a value of N'_0 at $N_1 = 0$.

3.2 Galet-LSC

Liquid scintillation counter (LSC) is used for a quantitative measurement of radioactivity, and it is especially useful for low energy beta decay radionuclides such as tritium. In measurements, radioactive sample is dissolved into a liquid scintillation cocktail in a vial. The radioactivity is quantified by counting the number of flashes of scintillation lights within a certain time period.

However, counting efficiency varies with the quench level of the sample, which depends on efficiency of energy transfer from the released beta ray in decay to the solute in liquid scintillator. The quenching decreases the number of generated scintillation photons. Therefore, compensation of count rate loss is essential to determine the radioactivity. In order to study the dependence of counting efficiency on quench level, Galet-LSC was developed.

Galet-LSC modeled LSC system for measurements based on liquid scintillation counting. The geometric parameters were taken from the LSC-5100 manufactured by Hitachi, Ltd. It consists of two photomultipliers (PMTs) installed around an optical chamber as shown in Fig. 9. These geometries were described in class GaletDetectorConstruction. Additionally, the optical properties were assigned to materials and the surface of optical chamber, in order to simulate propagation of optical photons that account for reflection and refraction at geometrical boundaries. C-14 or H-3 was chosen for a primary particle and randomly generated inside the scintillation cocktail volume by GPS. The physics-list consists of radioactive decay, electromagnetic and optical photon physics. The radionuclide emits a beta ray in radioactive decay physics. Then, optical photon physics generates scintillation photons isotropically along to the beta ray trajectory and transports those photons inside the optical chamber. The default yield of scintillating photons (Y) was set to 10 photons/keV for the material of liquid scintillator. An instance of GaletSD was attached to both PMT windows to be scoring volumes. In class GaletEventAction, scintillating photons at the PMT windows are randomly sampled according to the quantum efficiency of PMT, and those are accumulated as a PMT signal in one decay. The final pulse height in double coincidence method was calculated as the sum of two PMT signals by requiring more than certain number of photons detected in both PMTs.

Example distributions of C-14 pulse height spectra in two scintillation photon yields are demonstrated in Fig. 10. Here the unit of pulse height is given in the number of scintillating photons of two PMTs in one decay. The counting efficiency is defined by a ratio of the number of double coincidence events on the number of decays. The dependence of counting efficiency on scintillating photon yields was studied in previous research as shown in Fig. 11. The detailed simulation and analysis in comparison with C-14 and H-3 measurements are described in [9,10].

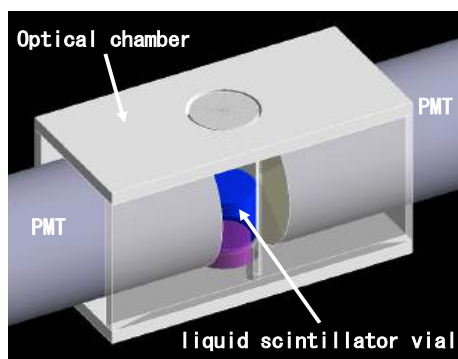


Fig. 9 Galet-LSC geometry modeled LSC-5100 system manufactured by Hitachi, Ltd. The system consists of sample vial filled with liquid scintillator, optical chamber and two PMTs.

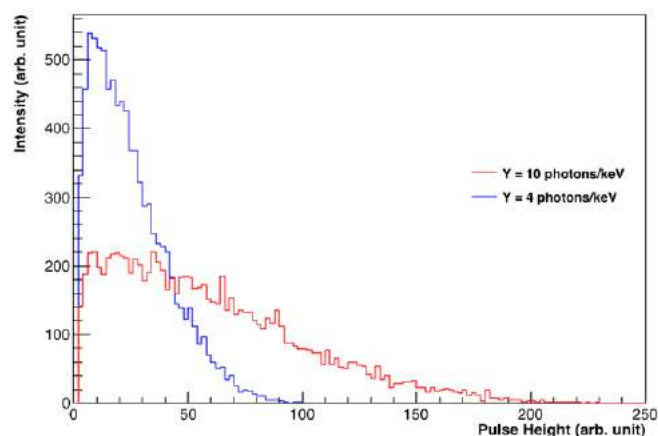


Fig. 10 Example pulse height spectra of C-14 in Galet-LSC simulation. The scintillating photon yields with $Y = 10$ photons/keV (red) and 4 photons/keV (blue) were chosen in the simulation for demonstrative purpose.

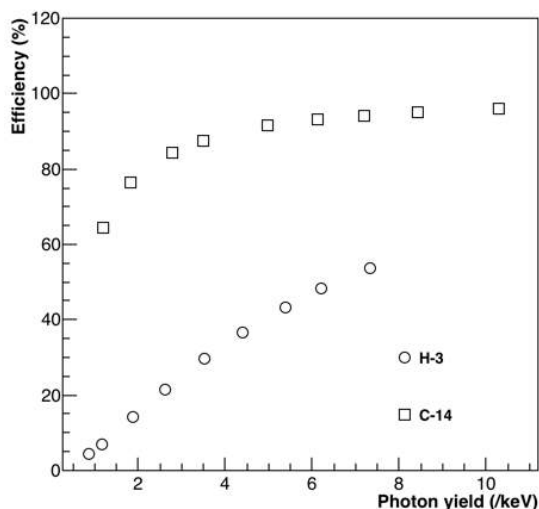


Fig. 11 Example results about dependence of counting efficiencies in H-3 and C-14 on photon yields achieved with Galet-LSC simulation.

3.4 Galet-DNA

Geant4-DNA is an extension of Geant4. It has been developed by Geant4-DNA project [18-21] for studying DNA damage caused by radiations. The interactions are newly taken into account for low energy electromagnetic reactions of electrons and protons with water, water radiolysis, diffusions and bimolecular reactions of radicals. The energy covers ranging from a few hundred MeV down to eV. These interactions concern to DNA strand breaks through direct and indirect processes, which mean the direct energy transfer from charged particles and the bimolecular interactions of radicals with the molecules in DNA. Many simple examples are supplemented in Geant4 source code to explain how to use the Geant4-DNA functions one by one.

Galet-DNA is our on-going project to develop a comprehensive application for studying DNA damages by utilizing Geant4-DNA functions. Especially we focus on DNA damages caused by low energy and low rate electrons. In such radiations, both direct and indirect processes contribute comparably. Therefore, the physics-list needs to include both physics constructors for the low energy electromagnetic interactions and the chemical reactions, i.e. G4EmDNAPysics and G4EmDNAChemistry packages in Geant4-DNA. In addition, the geometry of DNA and protein molecular structure need to be imported into the simulation with a commonly used description format.

We integrated Galet-DNA simulation by referring the parts of “chem3”, “chem4” and “pdb4dna” example codes in extended medical example in Geant4-DNA. These example codes show how to visualize trajectories of chemical species in chemistry processes, how to access the information of free radicals, and how to construct a geometry from the protein data bank (PDB) [22], respectively. The classes in Galet-DNA are classified into Galet original layer, intermediary layer and Geant4-DNA layer. The schematic module structure and representative classes in Galet-DNA is shown in Fig. 12.

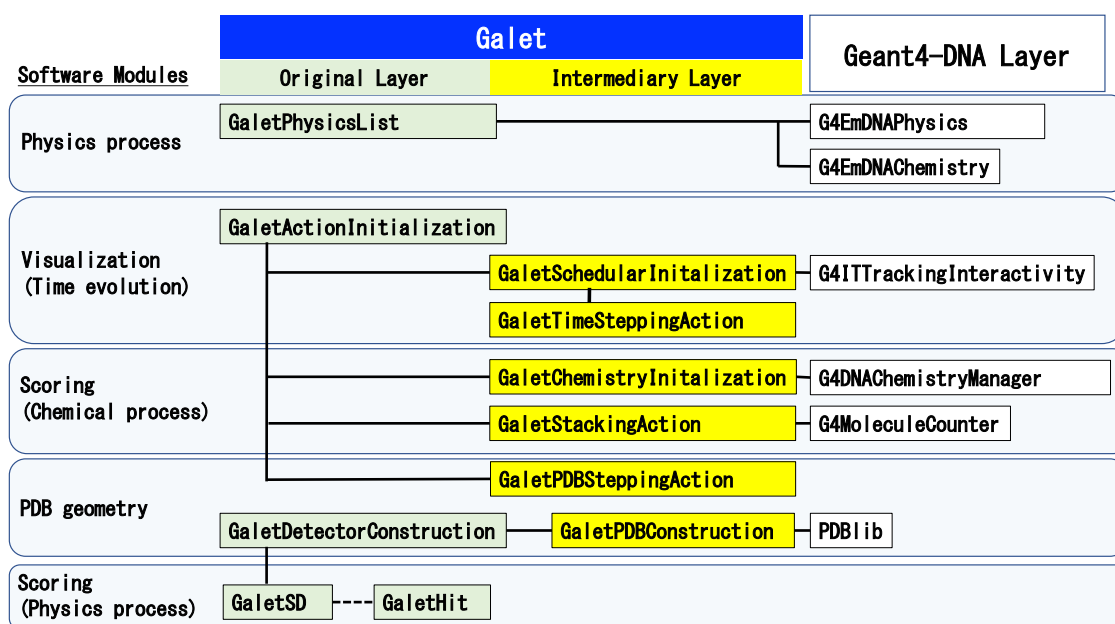


Fig. 12 Schematic module structure and the representative classes in Galet-DNA. The classes in green and yellow filled boxes are Galet-DNA classes, while the classes in white filled boxes are Geant4-DNA classes. The classes in intermediary layer of Galet-DNA indicated in yellow filled boxes were additionally introduced for importing a PDB geometry and analyzing reactions of free radicals.

The modules for physics processes, geometries and scoring relevant to physics interactions were successfully implemented on the original Galet framework, while we additionally introduced six classes in intermediary layer of Galet-DNA. The class names of these intermediary classes are shown in the figure with yellow filled boxes. The classes in the PDB geometry module, GaletPDBConstuction and GaletPDBSteppingAction, are used for importing geometric parameters from PDB database and discriminating associate hits among molecules in the PDB geometry. The other classes in intermediary layer are for accessing time and space information of free radical species produced in chemical reactions of Geant4-DNA. The outcomes of particle transport are stored in instances of GaletHit and G4MoleculeCounter relevant to physics and chemistry processes, respectively. These instances are retrieved from the class GaletEventAction for further analysis and recording.

Examples of a DNA geometry and radical trajectories in Galet-DNA are shown in Fig. 13 and Fig. 14. Here the structure of a B-DNA dodecamer was imported from PDB data base, and the radicals were produced in water radiolysis by injecting a 1 keV primary electron. Because Galet exactly follows the manner of Geant4 software development, integrating the Geant4-DNA functions into Galet-DNA was simple and straightforward.

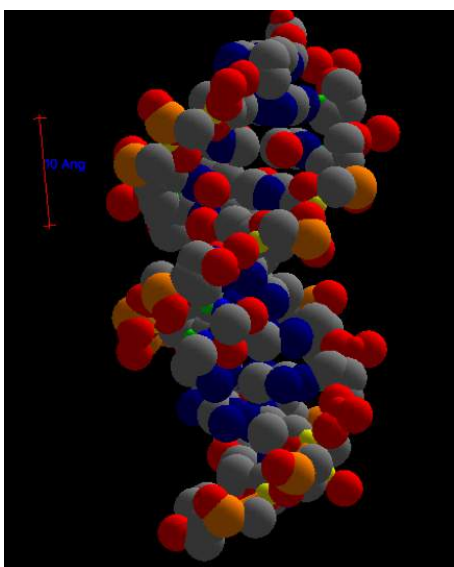


Fig. 13 Geometry of DNA strand pair with atomistic view imported from PDB database in Galet-DNA. The spheres with gray, red, blue, yellow and orange stand for elements of C, O, N, S and P, respectively.

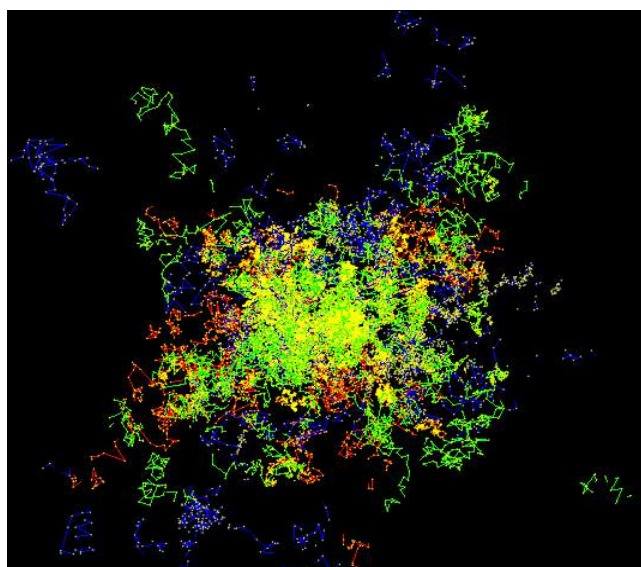


Fig. 14 Example simulation of Galet-DNA. A 1 keV electron was injected in water. The tracks in red, green and blue lines stand for trajectories of radicals with negative, neutral and positive charges such as OH^- , H_2O_2 and H_3O^+ , respectively.

4. Conclusion

Galet minimize users' effort in Geant4 application developments by providing the skeleton program with versatile concrete classes. The extendibility and efficacy of Galet have been validated through the developments of various example applications. Since Galet exactly follows manner of Geant4 simulation toolkit, it can be utilized by beginners as a primer code of Geant4 application developments, that has more important meaning in educating beginners to Geant4 application developers. Furthermore, Galet is useful for developing an integrated simulation software with extensions such as Geant4-DNA, as well as mock simulation software for rapid prototyping.

Acknowledgments

This work was partly supported by JSPS KAKENHI Grant number 18K11650, 17H01084 and 17K07006.

References

- [1] S. Agostinelli et al., "Geant4 – a simulation toolkit", Nucl. Instrum. Meth., A506, pp. 250–303, 2003.
- [2] J.Allison et al., "Geant4 developments and applications", IEEE Trans. Nucl. Sci., 51, no. 1, pp. 270-278, 2006.
- [3] J. Allison et al., "Recent developments in Geant4", Nucl. Instrum. Meth., A835, pp. 186-225, 2016.
- [4] T. Sato et al., "Features of Particle and Heavy Ion Transport Code System (PHITS) version 3.02", J. Nucl. Sci. Technol., 55, pp. 684-690, 2018.
- [5] D.B. Pelowitz Ed., "MCNPX Users Manual Version 2.7.0", LA-CP-11-00438, 2011.
- [6] T. Akagi et al., "Geant4 based particle therapy simulation framework for verification of dose distributions in proton therapy facilities", Prog. in Nucl. Sci. Technol. , 4, pp. 896-900, 2014.
- [7] T. Akagi et al., "The PTSim and TOPAS projects, Bringing Geant4 to the Particle Therapy Clinic", Prog. in Nucl. Sci. Technol., 2, pp.912-917, 2011.
- [8] T. Aso et al., "Geant4 based Monte Carlo simulation for verifying the modified sum-peak method", Appl. Radiat. Isot., 134, pp.147-150, 2018.

- [9] T. Aso et al., "Validation of Beta Ray Scintillation Spectra in Liquid Scintillation Counter using Geant4 Simulation", IEEE NSS/MIC Conf. Rec., N04-03, 2014.
- [10] T. Aso et al., "Estimation of photon yield in liquid scintillation counter by using Geant4 Monte Carlo simulation", Prog. in Nucl. Sci. Technol., Accepted for publication, 2018.
- [11] M. Hara et al., "Monte Carlo simulation of tritium beta-ray induced X-ray spectrum in various gasses", Fusion Engineering and Design 131, pp.125-129, 2018.
- [12] M. Shoji et al., "Modification of LSC spectra of ¹²⁵I by high atomic number elements", Appl. Radiat. Isot. 139, pp.131-136, 2018.
- [13] G.A.Birnkman et al., "Absolute standardization with a NaI(Tl) crystal-I", Int. J. Appl. Radiat. Isot. 14, pp.153-157, 1963.
- [14] G.A.Brinkman et al., "Absolute standardization with a NaI(Tl) crystal-II", Int. J. Appl. Radiat. Isot. 14, pp.433-437, 1963.
- [15] G.A.Brinkman et al., "Absolute standardization with a NaI(Tl) crystal-III", Int. J. Appl. Radiat. Isot. 14, pp.503-510, 1963.
- [16] Y. Ogata et al., "Development of a modified sum-peak method for activity determination of some gamma emitters", Nucl. Instrum. Meth. Phys. Res., A775, pp.34-40, 2015.
- [17] Y. Ogata et al., "Development of the modified some-peak method and its application", Appl. Radiat. Isot., 109, pp. 354-357, 2016.
- [18] S. Incerti et al., "Geant4-DNA example applications for track structure simulations in liquid water: a report from the Geant4-DNA Project", Med. Phys. 45, e722-e737, 2018.
- [19] M.A Bernal et al., "Track structure modeling in liquid water: A review of the Geant4-DNA very low energy extension of the Geant4 Monte Carlo simulation toolkit, Phys. Med. 31, pp.861-874, 2015.
- [20] S. Incerti et al., "Comparison of Geant4 very low energy cross section models with experimental data in water", Med. Phys. 37, pp.4692-4708, 2010.
- [21] S. Incerti et al., "The Geant4-DNA project", Int. J. Model. Simul. Sci. Comput. 1, pp.157-178, 2010.
- [22] E. Delage et al., "PDB4DNA: implementation of DNA geometry from Protein Data Bank (pdb) description for Geant4 DNA Monte-Carlo simulations", Comput. Phys. Commun. 192, pp.282-288, 2015.

(Received: 29 October 2018, Accepted: 7 February 2019)

Numerical Study on Core Degradation Behavior with TRAC and MCCI Behavior with MELCOR at Fukushima Dai-ichi Nuclear Reactor Accident

Kohei Ueta, Hiep Huy Nguyen, Kazuyuki Takase*

¹⁾Department of Nuclear System Safety Engineering, Nagaoka University of Technology,
1603-1 Kamitomioka-machi, Nagaoka 940-2188, Japan

*E-mail: Takase@vos.nagaokaut.ac.jp

As part of research for clarifying the cause of the Fukushima Dai-ichi nuclear power plant (1F) accident, both phenomena on core degradation and Molten Corium Concrete Interaction (MCCI) were analyzed numerically. Thermal hydraulic behavior in a reactor core during the core degradation was estimated with TRAC-BF1. On the other hand, MCCI behavior was evaluated with MELCOR. From the TRAC-BF1 estimation results, predicted temperature and pressure distributions in the unit 1 of 1F under the different start-up conditions of the reactor core Isolation cooling Condenser (IC) were obtained. Moreover, predicted erosion characteristics on the pedestal of the containment vessel in Boiling Water Reactor (BWR) during MCCI were also estimated by MELCOR (based on the severe accident condition such as 1F).

1. Introduction

At Fukushima Dai-ichi nuclear power plant (1F), scram of the unit 1 to unit 3 was carried out because of the Pacific coast of Tohoku Earthquake happened on March 11th, 2011 2:46 pm. After that, the removal of residual heat was continued via Residual Heat Removal system (RHR) powered by Emergency Diesel Generator (EDG) as substitute for the lost external power source. However, EDG was stopped due to the influence on seismic sea wave reached at 3:37 pm, making the station blackout. At unit 1 to unit 3, the situation that was not capable of to inject water into the reactors had been continued although the cooling was carried out with the actuation of core cooling function without alternating power source. Therefore, the fuel rods were exposed and reactor core meltdowns were happened at those units.

A reactor core Isolation cooling Condenser (IC) is a part of safety equipment for design basis accident for Boiling Water Reactor(BWR)-3 and is able to cool down the steam of the Reactor Pressure Vessel (RPV) using the water stored in its secondary side, and bring back the condensed water into RPV via natural convection. IC has two independent systems of A and B, and external power source is not needed to actuate IC except for opening and closing the valves. IC was actuated automatically and started the reactor core cooling after 300 s of the earthquake occurrence. In order to adjust the cooling rate, IC was stopped after 960 s of the earthquakes occurrence. The operators had controlled the cooling rate (under 55°C/h) of Unit 1 by opening and closing an isolation valve on IC system A until when station blackout occurred by seismic sea wave¹⁻²⁾. After the Direct Current (DC) power of Unit 1 was lost, the operators tried to open the isolation valves, but it was found out that the valve could not be driven due to the blackout. However, it was uncertain about how much the operation of IC influenced the reactor core cooling. Thus, in the present analysis using TRAC-BF1³⁾ which is a transient reactor analysis code, thermal-hydraulics analysis targeted at the unit 1 of 1F was conducted, and the core cooling situation in the reactor after the DC power of Unit 1 was lost was comprehended. Inoperability of High Pressure Coolant Injection system (HPCI) was assumed, the possibility with regard to avoidance or delaying of core melt was considered using only IC.

On the other hand, Molten Corium-Concrete Interaction (MCCI) behavior was considered numerically. As shown in Fig. 1, MCCI is one of the severe accident phenomena and occurs by core meltdown. As a result, corium is relocated from the vessel into the reactor cavity where means the

pedestal of a Reactor Containment Vessel (RCV). The interaction involves melting and decomposition of concrete, chemical reactions between the concrete and corium materials, and heat transfer from the corium to its surroundings. Uranium dioxide, zirconium dioxide, zirconium and stainless steel comprise the core melt. The major constituents of concrete are SiO_2 , CaO , Al_2O_3 , MgO , Fe_2O_3 , K_2O , Na_2O , free water, chemically bound water and CO_2 . When the molten core material contacts the concrete and the temperature of the concrete reaches the ablation temperature, the concrete begins to ablate and a layer of molten concrete or slag forms that separates the solid concrete below from the overlying core melt. Here, one of the most severe issues is the erosion of concrete. Then, the amount of the erosion of concrete at MCCI was predicted with MELCOR. MELCOR is one of severe accident analysis codes and can predict physical phenomena in the reactor related to the severe accident. In the present analysis using MELCOR, some assumptions were defined from severe accident such as 1F. In order to comprehend the tendency of erosion, a prediction of the erosion characteristics on the pedestal of RCV were conducted.

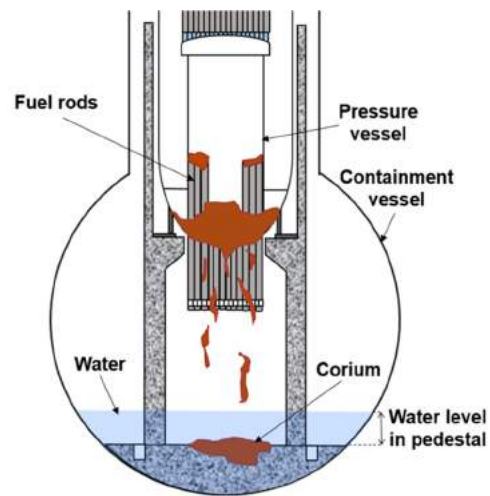


Fig. 1 Schematic diagram of BWR at severe accident

2. Numerical Analysis

2.1 TRAC-BF1 analysis

TRAC-BF1 is a transient reactor analysis code to provide advanced best-estimate predictions of postulated accidents in BWR. Figure 2 shows a nodding diagram of TRAC-BF1 which simply simulates major components of the unit 1 in 1F and consists of a pressure vessel (including fuel assembly, steam-water separator, downcomer, jet pump), water supply system, recirculation system, main steam system, RCV and IC.

RPV was a cylindrical shape with an overall height of 19.6 m and shell inner diameter of 4.8 m. The external wall was assumed to be an insulated wall without thickness, and the thermal conduction from RPV to RCV and thermal capacity of RPV were neglected. The fuel assembly were high-burnup 8×8 and high-burnup 9×9 , which was 68 bodies and 332 bodies, respectively. The axial direction output distribution of fuel was configuring the output at several heights based on the output ratio immediately before the earthquake which listed on the operating record. Besides, the output ratio between fuel assemblies was assumed constant. The water supply system was connected to the top position of downcomer, and the constant flow rate was injected with the water supply flow rate (689 kg/s) and temperature (176.7°C) which are based on the application document for nuclear installation license⁵). From the reactor scram until the station blackout, the injection flow rate was controlled automatically in order to stabilize the water level on the upper side which was about 5 m from the top of reactor core.

RCV was simplified as a cylindrical that has an inner diameter of 17.7 m, and it also assumed the following situations based on the application document for nuclear installation license⁵): spatial volume of RCV was $6,030 \text{ m}^3$, suppression pool water was $1,750 \text{ m}^3$, initial suppression water temperature was 30°C . As the lack of information had restricted the simulation of the flow path resistance, the flow rate of a main steam piping system of IC was defined as 100.6 t/h. Here, it was assumed that IC has the constant heat transfer coefficient of $3,000 \text{ W/m}^2\text{K}$ and the heat transfer capacity of $36.2 \times 10^5 \text{ kcal/h}$. The decay heat of fuel rod was obtained from the open information⁶).

In regard to the main parameter of steady operation before earthquake occurrence, Table 1 shows the comparison with listed values in the application document for nuclear installation license⁵) and calculated values. According to the analysis results, the reactor core coolant flow rate and steam quality at core exit were estimated. As shown in Table 1, the flow rate at core inlet of the construction permit

condition was about 10% smaller than the calculation condition, and the value was vice versa for the case of steam quality at core exit. This was attributed to the deficient adjusting pressure ratio of jet pump. However, the effect of accelerated loss regarding jet pump decrease and the position pressure loss must be dominative after the blackout. The influence on the analysis result after station blackout was considered as small.

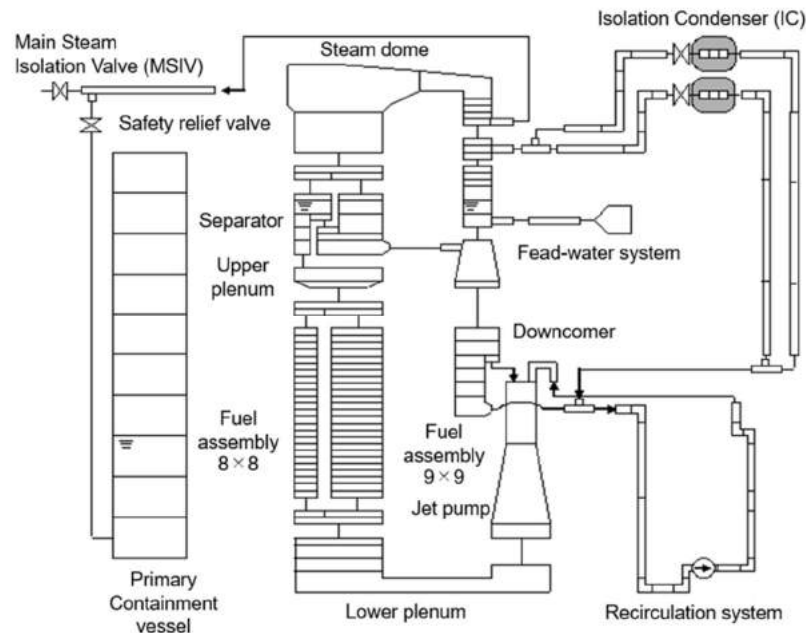


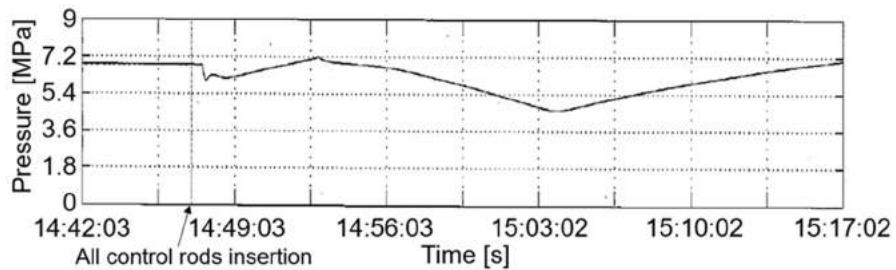
Fig. 2 Noding diagram of TRAC-BF1

Table 1 Comparisons between values in construction permit and calculation conditions

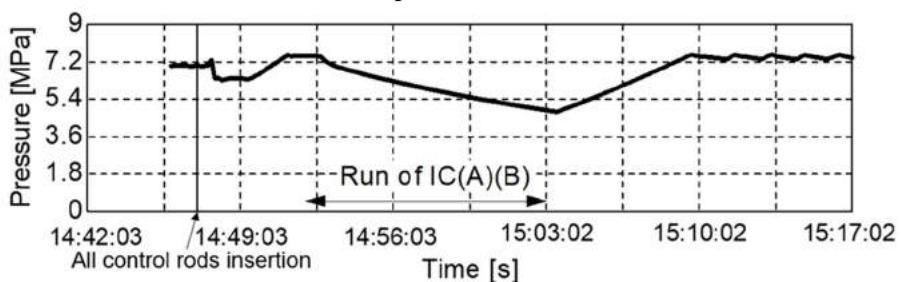
Parameters	Construction permit condition	Calculation condition
Power [MW]	1380	1380
Pressure[MPa]	6.99	7.01
Flow rate at core inlet [kg/s]	6055	6570
Temperature at core inlet [K]	549.2	549.5
Steam quality at core exit [-]	0.116	0.101
Flow rate in recirculation[kg/s]	3028	3355
M ratio of jet pump[-]	1.00	0.95

As for each event and the occurrence time, the essential events were picked out from what was listed in the government report¹⁾. The event time series put in the analysis is shown in Table 2. The all-control rod insertion time after the earthquake was zero. Figure 3 shows the comparisons with the operation record⁴⁾ as regards of the reactor pressure before and after the earthquake and the calculation result. According to the operating record, the both IC (A) and IC (B) were started after 300 s of earthquake occurrence, the reactor pressure was back to around 7.2 MPa by the manual shutdown of IC after its pressure decreased from around 7.2 MPa to 4.5 MPa. Even in the calculation result, the same change was shown and the change on reactor pressure was capable of predicting via IC actuation. With reference to the increase in pressure before IC was turned on and after it was turned off, the

calculation result shows the increase rate about two times as compared with the operating record. The reason was considered that thermal capacity of RPV was neglected in the analysis and the time change on pressure was estimated sharply.



(a) Operation record



(b) Calculation result

Fig. 3 Comparison of pressures between operation record and calculation

Table 2 Event time table

Time	Elapsed time [s]	Event
14:46	-100	Reactor scram
14:47	0	All control rods insertion Main steam isolation valve (Closing)
14:52	300	Isolation Condenser (IC(A)(B)) on
15:03	960	(IC(A)(B)) off
15:17	1800	IC (A) on
15:19	1920	IC (A) off
15:24	2220	IC (A) on
15:26	2340	IC (A) off
15:32	2700	IC (A) on
15:34	2820	IC (A) off
15:37	3000	Station blackout
18:18	12660	IC (A) on
18:25	13080	IC (A) off

The present analyses were carried out three different conditions in order to evaluate the influence on the core cooling with IC. Case 1 is the event simulation described in the government report, which is the condition that the IC was actuated for 7 minutes after 2.7 hours (12,660 s) of the station blackout. On the other hand, Case 2 and Case 3 were just some assumption to the severe accident of 1F and not the real phenomenon. Case 2 was the assumed analytical condition where IC was operable after 1.5 hours (8,400 s) of the station blackout, while Case 3 was the assumed analytical condition in which the IC operated immediately after the earthquake.

2.2 MELCOR analysis

MELCOR is one of severe accident analysis codes and can predict physical phenomena of core meltdown, reactor vessel failure, hydrogen generation, fission product release, etc. in addition to MCCI. In this analysis using MELCOR, the target unit was not defined especially, however some analytical conditions were assumed based on severe accident such as 1F.

Figure 4 shows the present analytical model for the MELCOR analysis. Each component of BWR is simply simulated. In the calculations, two analytical conditions were assumed; one is the dry condition that the pedestal of RCV is no water; another is the wet condition that the pedestal is occupied with water with height of 5 m and temperature of 300 K. In the present calculation, analytical condition can be seen in Table 3 was considered. The initial parameters at MCCI are shown in Table 4. Here, the temperatures related to both oxide layer and metal layer and the initial fuel debris compositions are decided based on Ref. 7-9).

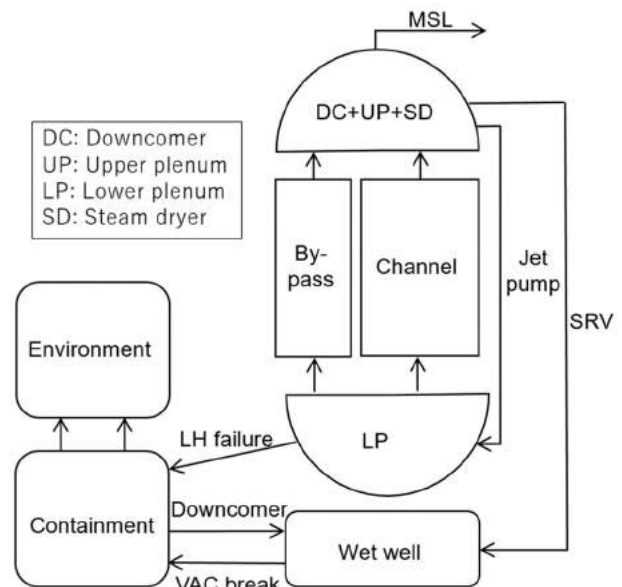


Fig. 4 A calculation model of MELCOR which simply simulates BWR structural components

Table 3 Analytical conditions

Event	Time (s)
Core has uncovered by water	74.66
Core supports plate breaks	3452.35
Failure of lower head, beginning of debris ejection to pedestal	6043.74
MCCI occurs	6044.82

Table 4 Initial parameters at MCCI

Oxide layer temp. [K]	Metal layer temp. [K]	Initial fuel debris compositions [kg]			
		UO ₂	Zr	Stainless steel	Total
3113	2098	96000	19200	15400	130600

3. Results and Discussion

3.1 Predicted Core Behavior

Figure 5 shows the reactor pressure and the reactor water level, maximum temperature of fuel in Case 1. Here, reactor water level which is the quantity of water from the bottom of RPV was obtained via integration. Case 1 simulated an actual phenomenon, the reactor water level was gradually decreased while changing since the steam produced by decay heat was discharged from relief safety valve to RCV. Hence, the reactor core was fully exposed from the coolant due to sharp decrease of the reactor water level after 3 hours (9,800 s).

The result of Case 2 is shown in Fig. 6. This case simulates a situation in which the reactor water level could be maintained via IC actuation while the two-phase flow was forming. In Case 2, for a faster IC operation, the pressure was stabilized (between 6 ~ 7 MPa) while condensing the steam, and the reactor water level was held as high as the height of reactor core. Here, the void fraction of reactor core was around 55%, the two-phase natural circulation flow was formed and the entire fuel rods were able to be cooled down, since the interface between two-phase flow and steam single-phase was situated around the upper steam-water separator. Thus, the melting of the reactor core could possibly be retarded for 8 hours (16 hours if B system is also used) if IC was actuated during forming the two-phase flow natural circulation flow. Besides, the result of Case 2 demonstrates that there was a possibility to avoid the reactor core melt if the water injection was able to be carried out into RPV and secondary side of IC in the interval.

Figure 7 shows the result of Case 3. When IC operates normally, it is found that a meltdown would be avoidable. However, there is a possibility in this analysis that the time change as regards to pressure and temperature etc. was estimated sharply because the thermal capacity of the structure was not considered. Furthermore, the steam dragged by the downcomer was flowed with high void fraction to the underneath plenum since the water injection of coolant from the water supply system was lost. Hence, it was considered necessary to verify the applicability of correlation formula related to carry-under phenomena in particular, since the formation of two-phase natural circulation flow has become an important factor.

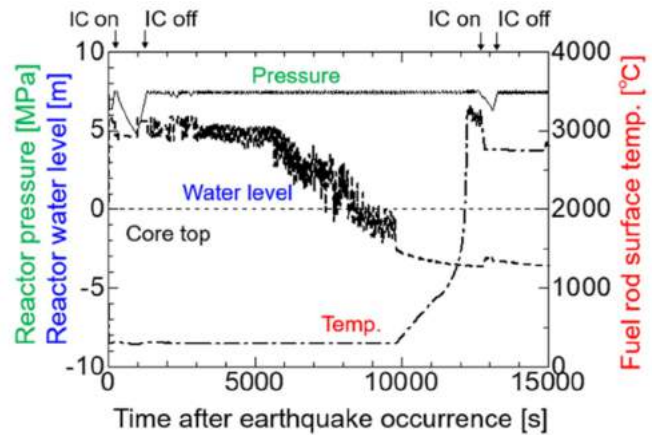


Fig. 5 Case 1: Actual results of unit 1 in 1F

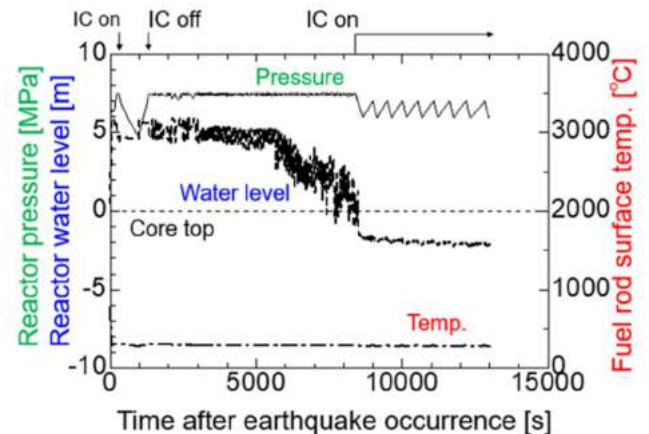


Fig. 6 Case 2: Results when IC is early started

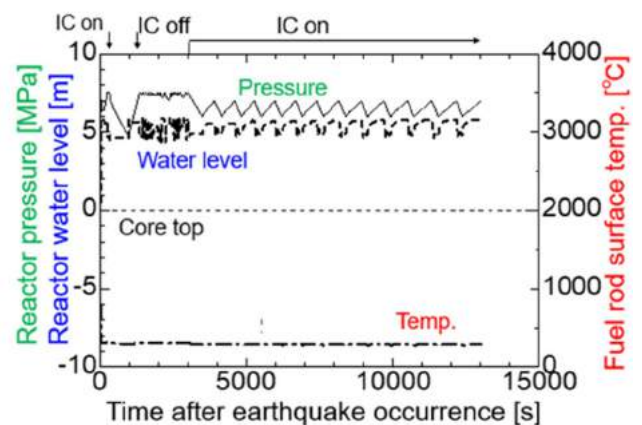


Fig. 7 Case 3: Results when IC is normally started

3.2 Predicted Erosion Rates

The predicted erosion rates of the concrete in the pedestal of RCV by MCCI and their schematic diagrams are presented in Table 5 and Fig. 8, respectively. In Table 5, the predicted erosion rates in the radial direction are 0.307 m for the dry condition and 0.181 m for the wet condition, and similarly, those in the radial direction are 0.213 m for the dry condition and 0.228 m for the wet condition. The predicted erosion rate in the axial direction of the concrete was almost the same for both dry and wet condition. In contrast, the predicted erosion rate in the radial direction of the concrete at the dry condition was 1.7 times higher than that of the wet condition. Furthermore, the erosion as regards radial direction are 0.307 m and 0.181 m, and the erosion as regards axial direction are 0.213 m and 0.228 m, as shown in the dry and wet condition. From this result, the following tendency was expected; the corium spreads in radial direction under the dry condition after falling on the concrete. As this reason, it is expected that since the erosion rate in the axial direction becomes almost the same under both the dry and wet conditions, the dry condition that the temperature in an upper surface of the corium becomes high compared with the wet condition will be remarkable to the erosion in the radial direction.

Table 5 Predicted erosion rates

	Dry condition	Wet condition
Radial direction [m]	0.307	0.181
Axial direction [m]	0.213	0.228

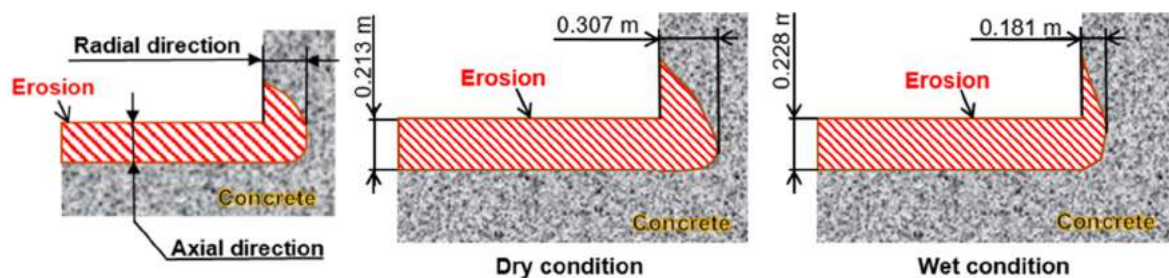


Fig. 8 Schematic diagram of erosion of concrete in pedestal of BWR

4. Conclusions

With regard to the unit 1 of Fukushima dai-ichi nuclear power plant, in order to comprehend the situation of the core cooling in the reactor by the influence of both Pacific coast of Tohoku Earthquake and seismic sea wave, thermal hydraulics analysis was operated with TRAC-BF1. As a result, it was found that the reactor core was able to be cooled down during the formation of two-phase natural circulation if the IC was able to use just after the reactor core started to be exposed. Moreover, MCCI behavior after the core degradation was analyzed numerically with MELCOR. As for two kinds of conditions that the pedestal of RCV is dry and wet, the predicted erosion rates in the axial and radial directions in the concrete of RCV were compared and the difference on the erosion rates between both conditions was clear. In the future, it is planned to improve the prediction accuracy of the present analysis results based on the information which becomes clear with the process of the decommissioning of 1F.

Acknowledgments

We would like to express our gratitude to Dr. Tamai and Dr. Akimoto for their kind cooperation and suitable advices regarding the numerical analysis.

References

- 1) Nuclear Emergency Response Headquarters, Report of the Japanese Government to the IAEA Ministerial Conference on Nuclear Safety - The Accident at TEPCO's Fukushima Nuclear Power Stations —, Nuclear Emergency Response Headquarters, Government of Japan, Jun. (2011).
 - 2) Atomic Energy Society of Japan, Report of “Seminars to investigate the accident at the Fukushima-Daiichi Nuclear Power Station” What were wrong? What should be done from now on?, Atomic Energy Society of Japan, Mar. (2013).
 - 3) J. A. Borkowski, N. L. Wade, TRAC-BF1/MOD1:An Advanced Best-Estimate Computer Program for BWR Accident Analysis, NUREG /CR-4356 (EGG-2626)(1992).
 - 4) Tokyo Electric Power Company, Touhoku Chiho Taiheiyuoki Jishin Hassei Touji no Fukushima Daiichi Genshiryoku Hatsudensho Unten Kiroku oyobi Jiko Kiroku no Bunseki to Eikyo Hyouka nitsuite, Tokyo Electric Power Company, 23 May (2011), [in Japanese].
 - 5) Tokyo Electric Power Company, Fukushima Daiichi Genshiryoku Hatsudensho 1 Gouki no Genshiro Secchi Kyoka Shinseisho, Tokyo Electric Power Company, May (1991), [in Japanese].
 - 6) Tokyo Electric Power Company, Ronai Nenryou no Houkainetsu (Jisingo Yaku Hantoshikan no Henka), News Release, Tokyo Electric Power Company, 26 May (2011), [in Japanese].
 - 7) Nishimura, Satoshi, et al. "Severe accident analysis of a representative LWR plant with MAAP5. 01 and MELCOR2. 1. Comparison of station blackout analysis for a BWR-5/advanced Mark-II containment type plant." *Denryoku Chuo Kenkyusho Hokoku* (2014): 1-4.
 - 8) TEPCO. “Fukushima Dai-ichi Genshiryoku Hatudensyo 1 ~ 3 Gouki no Rosin Zyoutai ni tuite.” http://www.tepco.co.jp/nw/fukushima-np/images/handouts_111130_09-j.pdf (2011), [in Japanese].
 - 9) JNES. “Heisei 21 nendo Zishinzi Revel 2 PSA no Kaiseki (BWR).” <http://kagakucafe.org/jnes000017303.pdf> (2010), [in Japanese].
- (Received: 29 October 2018, Accepted: 14 February 2019)

Basic property of the wind turbine with the circular cylinder blades driven by longitudinal vortex

Yuya Kimura¹, Takumi Sankyo¹, Hayate Kimura¹, Syodai Sugimura¹,
Takahiro Nomura^{1,*}, Shigeru Ogawa¹, Yuji Yamada¹, Tsutomu Takahashi²

¹⁾ Department of Mechanical Engineering, National Institute of Technology, Kure College,
2-2-11 Aga-minami, Kure 737-8506, Japan

²⁾ Department of Mechanical Engineering, Nagaoka University of Technology,
1603-1 Kamitomioka-machi, Nagaoka 940-2188, Japan

*E-mail: nomura@kure-nct.ac.jp

Focusing on a wind turbine driven by a longitudinal vortex invented by Takahashi et al. in 2016, a wind turbine with cylindrical blades driven by a longitudinal vortex was produced experimentally. Wind tunnel experiment was conducted to clarify the basic characteristics of the prototype. As a result, power coefficient curves related to rotational speeds were experimentally obtained by changing the parameters of the number of the cylindrical blades and the thickness of the ring plate.

1. Introduction

Recently, energy shortage is urgent problems to be solved since energy demand are greatly increasing across the world. Therefore it is keenly needed to construct electrical generating systems using renewable energy such as wind and solar power. Among such renewable energy, wind power generation is one of the renewable energies most introduced in the world. The wind turbine can generate electricity day and night and be installed in any electricity demanding areas if it is compact. However, fundamental improvements of the wind turbine are required because Japan has no sufficient installation places especially in the suburbs of metropolitan areas and is frequently exposed to strong winds by typhoons every year. Faced with these circumstances, the authors have focused on the wind turbine with the circular cylinder blades which can maintain sufficient strength with even a small size and conducted basic research to understand its characteristics [1,2]. This wind turbine is a horizontal axis wind turbine driven by a longitudinal vortex, which was originally invented by Takahashi et al.[3] in 2016, and its basic mechanism and fundamental characteristics were investigated by Sakamoto et al.[4,5] and Hemsuwan et al.[6-8]. However there still remain many problems to be solved. For example, in Sakamoto et al.[4], the width of the ring plate is optimal for $w/d=1.0$ and 1.5 from the viewpoint of wind turbine rotation speed, but the diameter and thickness of the ring plate are not shown. Also, by Koide et al.[9] and Kato et al.[10], it is assumed that there is no influence of the thickness of the flat plate at the cross-crossing of the column-flat plate system. They confirmed the range of the thickness of the flat plate from 5 to 22mm, however not all the thicknesses were clarified. For this reason, the paper aims to verify the experimental results of Takahashi et al. and studies the influence of both the number of the cylindrical blades and the thickness of the ring plate behind the cylindrical blades on enhancement of power generation.

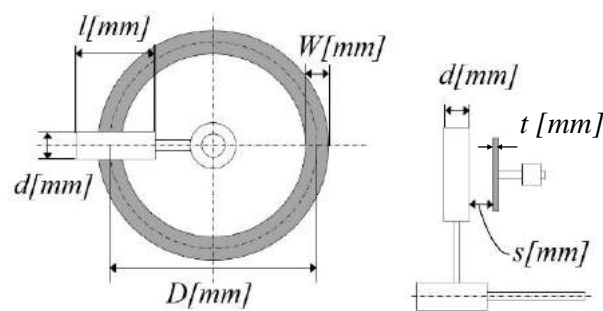
2. Methods of Experiment

2.1 Operating principle of wind turbine

The outlines of produced experiment equipment are shown in **Fig.1**. It's a horizontal axis wind turbine with circular cylinder blades, and a ring plate is arranged behind the circular cylinder blades. Circular cylinder blades are fixed to a rotating shaft, and arranged so that the blades are orthogonal to the wind like the propeller type of horizontal axis wind turbine. Mounting holes for circular cylinder blades were installed at intervals of 30, 36, 45 degrees on the rotating shaft, so that 2, 3, 4, 6, 8, 10, and 12 circular cylinder blades could be mounted according to experimental conditions.



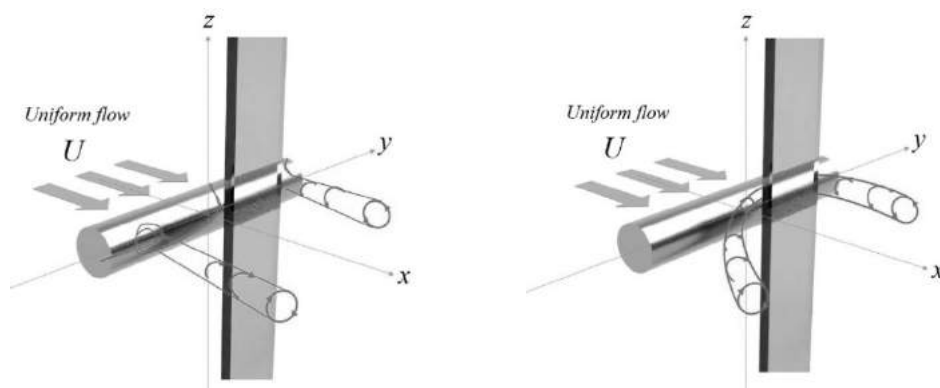
(a) Appearance of experimental equipment



(b) Various parameters

Fig.1 Outline of experimental equipment

When the gap s between the ring plate and the circular cylinder blade is in a certain range, either a trailing vortex or a necklace vortex[9] is generated in the vicinity of the intersection of the circular cylinder blade and the ring plate, as shown in **Fig.2**. When the necklace vortex is formed, the cylinder first swings and then starts to rotate. As a result, the circular cylinder blades steadily rotate at a constant angular velocity, and the steady lift force due to the longitudinal vortex is generated. The rotation direction has the same probability in both clockwise (CW) and counterclockwise (CCW) direction according to the initial rotation direction.



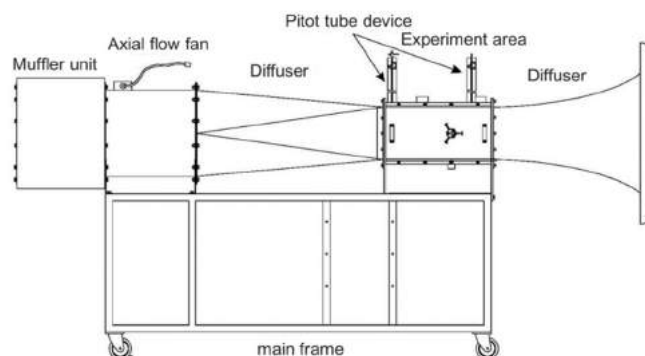
(a) Trailing vortex ($s/d \leq 0.3$)

(b) Necklace vortex ($0.3 < s/d < 0.6$)

Fig.2 Longitudinal vortices generated by flat plate

2.2 Wind tunnel device and Measurement system

The schematic diagram and specification of the wind tunnel experimental equipment used for the experiment are shown in **Fig.3**. This wind tunnel has the open section. Airflows are accelerated in a laminar flow state through the inlet of the diffuser, passes through the experimental area uniformly, and decelerated after passing through the diffuser of the exit side. Wind speeds setting in this wind tunnel experiment were confirmed using a Pitot tube and a hot wire anemometer at the main places in the experiment area without the wind turbine.



Length	3700mm
Depth	1065mm
Height	1900mm
Experiment area	Height 305mm × Depth 305mm × Length 600mm
Flow rate	0~36m/s (0~130km/h)
Control method	Motor drive control
Power supply	3-phase AC200V, 26A, 50/60Hz

Fig.3 Outline of wind tunnel device

Experiments were carried out with the wind turbine setting in the experiment area of the wind tunnel. The rotation number n [rpm], the torque T [Nm], and the power P [W] were measured by a torque meter (UTM -0.2Nm, UNIPULSE Co., Ltd.) and output to the PC through a torque monitor (TM201, UNIPULSE Co., Ltd.). Taking the average value of 1,500 pieces of data are acquired in 5 seconds with this torque monitor enables us to achieve high-accuracy power measurement and its high repeatability. In addition, the rotation number, the torque, and the power were measured by connecting the electromagnetic brake (HB0.5, OGURA CLUTCH Co., Ltd.) to the rotating shaft and controlling the voltage applied to the electromagnetic brake by the power supply unit (AD-8722D, A&D Co., Ltd.). The outlines of the measurement system are shown in **Fig.4**. Furthermore, it is able to confirm whether or not this wind turbine is driven by a longitudinal vortex by comparing each rotation numbers measured in both CW and CCW rotational direction without load and with the same rotation speed.

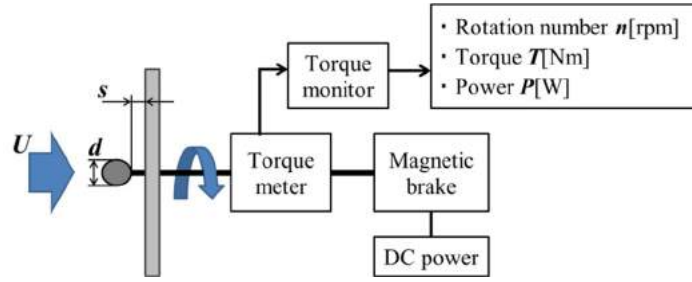


Fig.4 Outlines of the measurement system

2.3 Experimental conditions and Performance index

The experimental conditions are shown in **Table 1**. The ring-shaped flat plate was prepared with two sizes of thickness t of $t = 2.0\text{mm}$ and 5.5mm , and the number of circular cylinder blades N with $N=2, 3, 4, 6, 8, 10,$ and 12 .

Table 1 Experimental conditions

Wind speed U [m/s]	10
Blade diameter d [mm]	20
Blade length l [mm]	60
Gap s [mm]	7.0
Gap ratio s/d [-]	0.35
Ring diameter D [mm]	155
Ring width W [mm]	20
Ring thickness t [mm]	2.0, 5.5
Number of blades N [-]	2, 3, 4, 6, 8, 10, 12

In order to create a λ - C_p curve as an index of the performance of the wind turbine from the rotation speed and the power measured with each wind turbine shape, the tip speed ratio λ and the power coefficient C_p are calculated. The indexes λ and C_p are defined by the equations (1) and (2). Here, ω [rad/s] is the angular velocity, $R = (D + l)/2$ [m] the rotor radius, ρ [kg/m³] the fluid density, and $A (= \pi R^2)$ [m²] the projected area of the wind turbine.

$$\lambda = \frac{\omega R}{U} \quad (1)$$

$$C_p = \frac{P}{0.5\rho U^3 A} \quad (2)$$

3. Results and Discussion

3.1 λ - C_p curve

Fig.5 shows λ - C_p curves with blade number $N = 2, 3, 4, 6, 8, 10$ and 12 were employed as parameters. The main parameters of the wind turbine were used with gap ratio $s/d = 0.35$ and blade length $l = 60$ mm at blade diameter $d = 20$ mm, which were obtained under the optimal conditions in the previous experiments. The λ - C_p curves were evaluated with two types of the ring plate thickness t to compare the fundamental characteristics. Both curves show that C_p has a peak value at a certain speed ratio λ . Focusing on the vicinity of the peak value of C_p , it was found that C_p also increases with blade number $N = 2$ to 8 in case of plate thickness $t = 2.0$ mm. Regarding the thickness $t = 5.5$ mm C_p increases in proportion to blade numbers until $N=10$. This tendency seems due to increasing longitudinal vortices, corresponding to the increase in blade numbers. However, this tendency is restricted to the region where the longitudinal vortices generated from the circular cylinder blades do not interfere with those from other circular cylinder blades with an increase in blade number N .

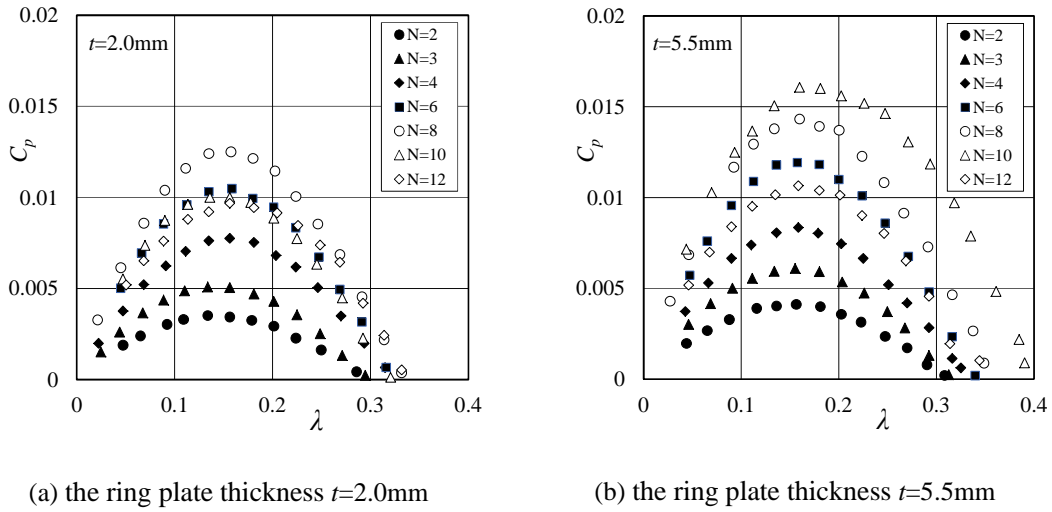


Fig.5 λ - C_p curves for the number of blades N ($s/d=0.35$, $\ell=60\text{mm}$)

3.2 N - $C_{p\max}$ curve

Fig.6. shows the N - $C_{p\max}$ curve obtained by extracting the maximum value $C_{p\max}$ of C_p at each blade number N from the λ - C_p curves in **Fig.5**. There is a tendency that $C_{p\max}$ increase as blade number N . C_p peaks in case of $N = 10$ at $t = 5.5 \text{ mm}$ and $N = 8$ at $t = 2 \text{ mm}$. However, after reaching the peaks $C_{p\max}$ tends to decrease sharply. In addition, compared with the same number of blades N , $C_{p\max}$ is higher as the ring plate is thicker. This shows that the ring plate thickness t affects generation of longitudinal vortex as the driving forces. Depending on the thickness of the ring plate, it is assumed that it influences to develop the necklace-shaped vortex flow in the vicinity of the ring plate. Therefore, it is considered that there exists an optimum ring plate thickness to enhance the wind turbine performance. In the future it is necessary to further conduct experiments by changing the ring plate thickness. In this experiment, the maximum $C_{p\max}$ value is about 0.016 at $N = 10$ and $t = 5.5 \text{ mm}$, but it is lower than the $C_{p\max}$ value currently in practical use as wind power generation. Therefore, it is necessary to examine basic characteristics in more detail and to find out the most suitable combination to increase the $C_{p\max}$ value.

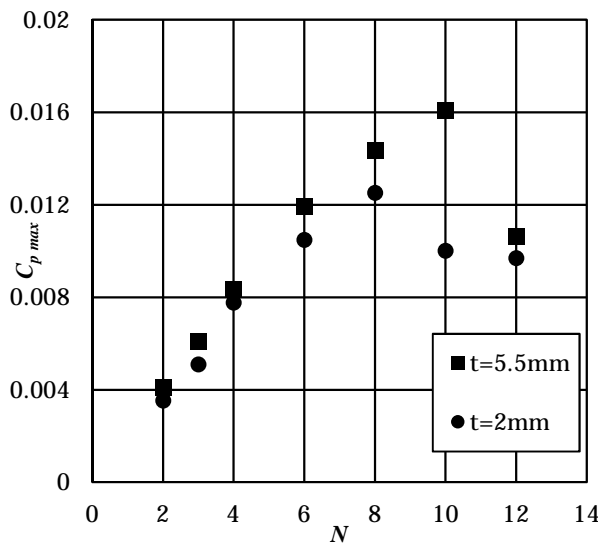


Fig.6 N - $C_{p\max}$ curves for the ring plate thickness t ($s/d=0.35$, $\ell=60\text{mm}$)

4. Conclusion

We manufactured the wind turbine with the circular cylinder blades driven by longitudinal vortex and conducted experiments with a wind tunnel. By examining the λ - C_p curve and the N - $C_{p\ max}$ curve obtained from the measurement values of the rotation speed and the power, with the basic shape of the wind turbine as a parameter, the following basic characteristics were shown.

- 1) Regardless of the ring plate thickness t , C_p increases as the number of blades N increases. However, the increasing tendency is that there is a limit number of blades N related to the ring plate thickness t , and when N exceeds the limit value, C_p does not increase.
- 2) Comparing $C_{p\ max}$ to the same number of blades N , it was found that $C_{p\ max}$ is larger as the thickness t of the ring-shaped flat plate is larger. Since this is a comparison with two kinds of plate thickness this time, it is necessary to further experiment by changing plate thickness further.

Acknowledgments

This study has been supported from “NUT grant for collaborative research with Colleges of Technology”.

References

- [1] S. Ogawa et al., “Study on horizontal type turbine driven by longitudinal vortex system,” The 14th International Conference on Motion and Vibration Control, no. A-05, pp.249-250, Aug. 2018.
- [2] S. Ogawa et al., “A new horizontal wind turbine with a circular cylinder driven by longitudinal vortex system,” Conference on Modelling Fluid Flow (CMFF’18) The 17th International Conference on Fluid Flow Technologies, no. CMFF18-096, pp. 1-7, Sep. 2018.
- [3] T. Takahashi et al., “A novel wind / water turbine with circular cylinder blades driven by steady lift force caused by longitudinal vortex,” JSME Fluids Engineering Conference, no. 0617, Nov. 2016.
- [4] K. Sakamoto et al., “Performance test of a novel wind turbine propeller with circular blades driven by longitudinal vortex,” JSME Fluids Engineering Conference, no. 0618, Nov. 2016.
- [5] K. Sakamoto et al., “Enhancement of efficiency of a new horizontal type turbine driven by longitudinal vortex,” 9th JSME-KSME Thermal and Fluids Engineering Conference, TFEC9-1421, Oct. 2017.
- [6] W. Hemsuwan et al., “Longitudinal vortex wind turbine: effect of the blade lengths,” Fluid-Structure-Sound Interactions and Control, Springer, pp.117-123, May. 2018.
- [7] W. Hemsuwan et al., “Lift force generation of a moving circular cylinder with a strip plate set downstream in cruciform arrangement: floe field improving in tip-ends,” International Journal of Aeronautical and Space Sciences, 19(3), pp.606-617, Aug. 2018.
- [8] W. Hemsuwan et al., “A longitudinal vortex wind turbine: numerical study,” Journal of Wind Engineering and Industrial Aerodynamics, 180, pp. 213-230, Sep. 2018.
- [9] M. Koide et al., “Vibration control for a circular cylinder by a strip-plate set downstream in cruciform arrangement (2nd report, generation and suppression of vortex excitation on elastically supported cylinder),” Transactions of the Japan Society of Mechanical Engineers. B., vol. 75-752, no. 08-0591, pp. 123-131, Apr. 2009.
- [10] N. Kato et al., “Vibration control for a circular cylinder by a strip-plate set downstream in cruciform arrangement (1st report, influence of downstream strip-plate on the shedding of longitudinal vortices from fixed system),” Transactions of the Japan Society of Mechanical Engineers. B., vol. 73-728, no. 06-0029, pp. 49-56, Apr. 2007.

(Received: 12 October 2018, Accepted: 7 February 2019)

Observation of Three Dimensional Nanostructures Fabricated by Two-Photon Polymerization Method

Son T. Nguyen^{1,†,*}, M. A. Hariz B. Mohd Pauzi^{1, †}, Tadachika Nakayama², Tsuyoshi Takahashi¹, Kenya Moriya², Yoshinori Tokoi³, Hisayuki Suematsu², and Koichi Niihara²

¹*Department of Creative Engineering, National Institute of Technology, Kushiro College, 2-32-1 Otanoshike-Nishi, Kushiro 084-0916, Japan*

²*Extreme Energy-Density Research Institute, Nagaoka University of Technology, 1603-1 Kamitomioka-machi, Nagaoka 940-2188, Japan*

³*Department of Electrical and Electronic System Engineering, National Institute of Technology, Nagaoka College, Nishikataki-machi 888, Nagaoka 940-8532, Japan*

[†]*these authors contributed equally to this work*

^{*}*E-mail: son@kushiro-ct.ac.jp*

The development in three-dimensional (3D) printing technology has enabled the ability to fabricate micromachines (MEMS) with feature size smaller than 100 nm. In this research project, a MEMS system with piston and filter for cracking bacterial cells and recovering useful precious chemical substances inside was fabricated by two-photon polymerization method. The structure of the created MEMS will be observed and analyzed with a high resolution scanning electron microscope. Then, the MEMS will be put into an experimental electric field to induce the movement of the piston. The piston can destroy the bacterial cell and release precious matter. The useful matters will pass through the filter of MEMS and will be collected at the other end of the system for further research purposes.

1. Introduction

The recovery of precious nanoparticles like palladium (Pt), selenium (Se), silver (Ag) or gold (Au), etc., accumulated in bacterial cell has attracted many interest of scientists because of their potential in nanofabrication, catalytic production, biomedical and environmental applications [1-4]. There are several methods which have been applied to extract those precious matter from bacterial cell. The extraction is mostly conducted via biology and chemical routes, like wet heat sterilization process [5] or bioreduction method [4, 6]. However, there have been very limited attempt to extract the precious particles via physically route though it would be low-cost and environmental friendly. The difficulty in precisely controlling a physical impact on a small objects at bacteria cell level is the main reason for this limitation.

In recent decades, nanofabrication has continuously developed and obtained remarkable achievements. One of these achievements is the application of two-photon absorption (TPA) method in three-dimensional (3D) printing technology [7-8]. Different from the case of single photon absorption, in TPA the illuminated polymer simultaneously absorbs two photons of near Infrared (IR) light. This method enables laser beams to be focused on a very small area called voxel as small as 65 nm. By using this technique, scientists and engineers can fabricate micro-level 3D structures which features smaller than 100 nm. This can give some clue to solve the above problem about physically extracting nanoparticles from cell.

In the present research, a micromachine (MEMS) containing a piston-and-filter system was 3D-printed with TPA method. From scanning electron microscopy observations, it was concluded that a honeycomb filter with a minimum hole diameter of 3.9 μm was successfully fabricated. The piston then can be induced by electric field to move and breakdown a bacteria cell and extract its precious matter through filtering holes (see Fig. 1). Our group has many experience in manipulating the motion of inorganic/organic microparticles in electric field [9-12]. Recently, we have been successful in fabricating a microcar that can be well-controlled in electric field [13]. The current research objective

is to find out whether the MEMS can be smoothly controlled by electric field inducement.

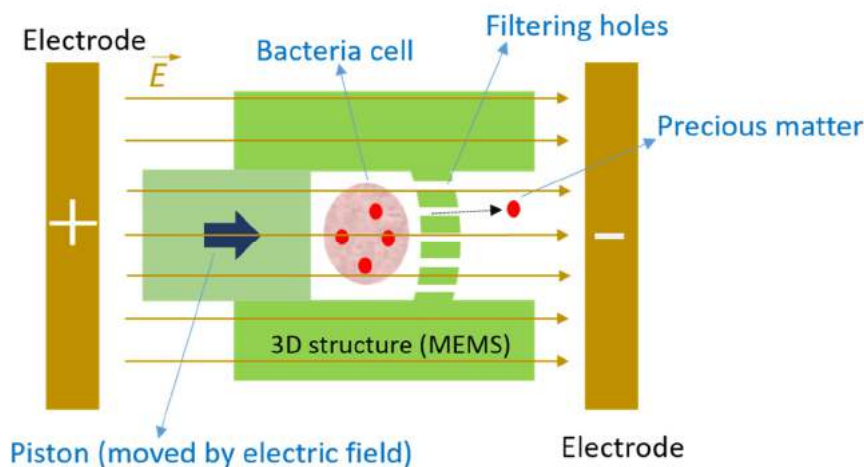


Fig. 1 Schematic illustration of 3D structure motion control by electric field to extract precious matter from bacteria

2. Experiment

In this research, the 3D microstructure was designed by a solid modeling computer-aided design (CAD) software (SolidWorks 2012, Dassault Systemes, France). The MEMS have micrometer dimensions, which are $150\ \mu\text{m}$ (length) \times $100\ \mu\text{m}$ (width) \times $80\ \mu\text{m}$ (height) for the microfilter, and $96\ \mu\text{m}$ (length) \times $55\ \mu\text{m}$ (diameter) for the piston. Filtering holes have hexagonal shape with $6.9\ \mu\text{m}$ of maximal diameter and $4.0\ \mu\text{m}$ of minimal diameter. The holes are arranged with honeycomb pattern because this structure has high strength and firmness [3] and the thickness of vertical walls between the holes is $0.7\ \mu\text{m}$. Figure 2 shows the design and dimensions of the microfilter and piston (see Fig. 2).

This design was used to fabricate the MEMS by using a micro 3D-printer (Photonic Professional GT, Nanoscribe, Germany). IP-G780, a commercial photoresist from the same company, was used as the material for printing the 3D microstructures. The printing process were conducted at Nagaoka University of Technology, then the fabricated 3D structure were then sent back to National Institute of Technology, Kushiro College for further observation and analysis. The fabricated MEMS was observed by an optical microscope (BX51M, Olympus, Japan) and a field-emission Scanning Electron Microscope (JSM-7001 FA, JEOL Ltd., Japan). Before scanning electron microscopy (SEM), sample was cleaned with ethanol in a sonication bath and then sputtered with gold by a fine coater (JFC-1600, JEOL Ltd., Japan) to avoid the charge-up effect on the sample surface.

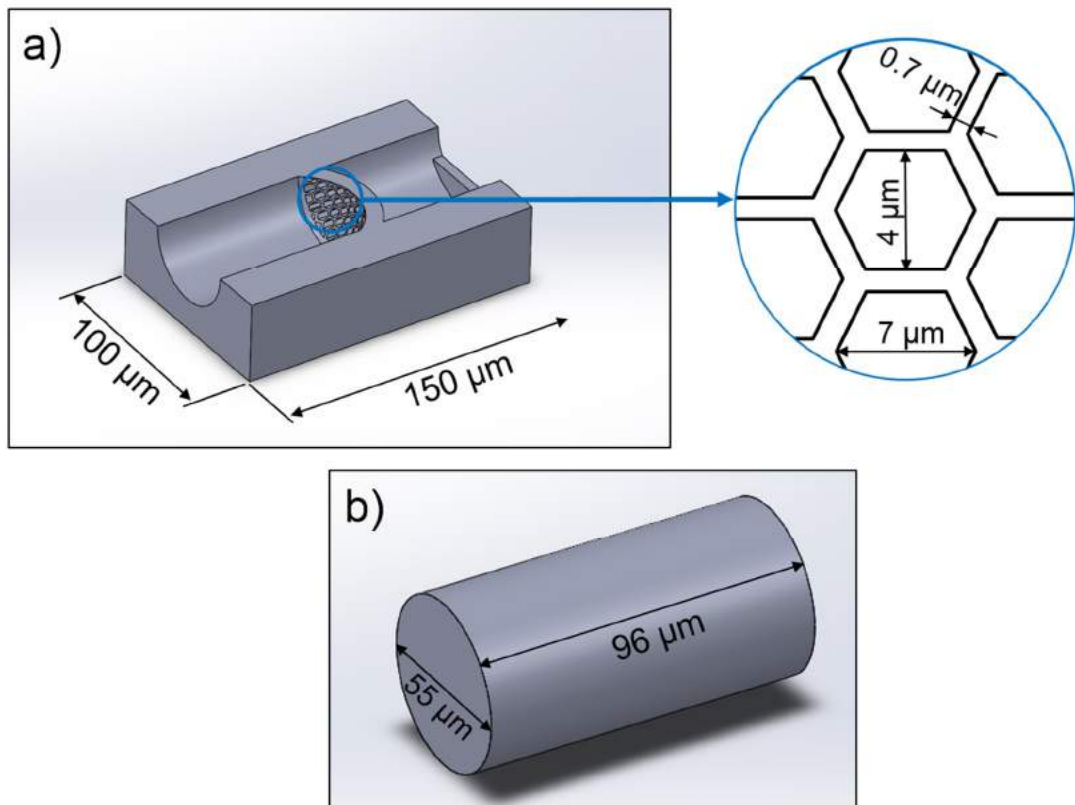


Fig. 2 Micromachine (MEMS) designed by Solidworks 2012: a) microfilter; b) piston

3. Results and Discussion

The optical micrographs of the filter and piston are shown in Fig. 3. The dimensions of the microfilter and piston was also measured to compare with those of the original design. Dimensions of the these structures were measured directly on the micrographs, showing that the microfilter is 151 μm (length) \times 102 μm (width), and the piston is 151 μm (length) \times 102 μm (width). These measurements are in consistent with the dimension from the original CAD design, confirming the high precision of the printing process.

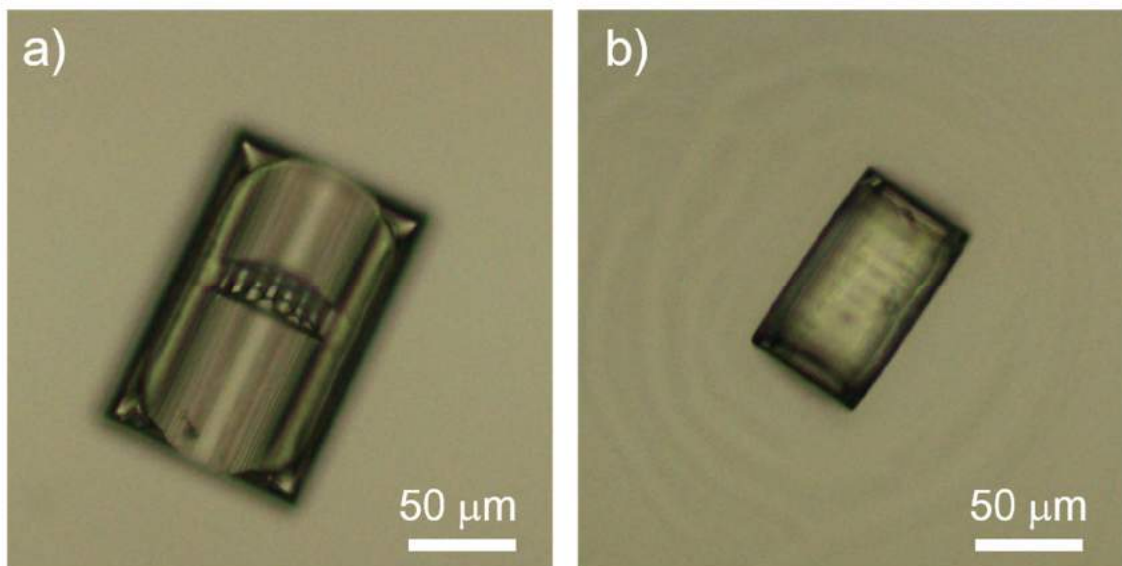


Fig. 3 Optical micrograph of the 3D-printed microstructures: a) microfilter and b) piston

The microstructure of the filter and the piston was investigated more carefully with the SEM observation to verify if there are any artifact on the 3D-printed microstructure. As shown in Fig. 4, several small artifacts appear on the surface of microfilter. Except a small artifact located at the entrance that may cause hindrance to the movement of the piston, other artifacts appear outside its moving path thus can be considered negligible.

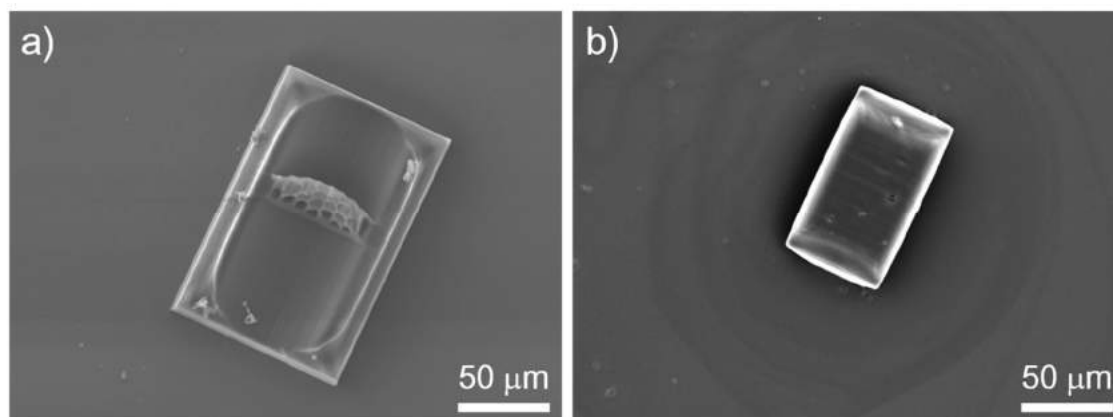


Fig. 4 SEM micrographs (top view) of the 3D-printed microstructures: a) microfilter and b) piston

These SEM micrographs in Fig. 4 confirms that the dimensions of microstructures are the same with those measured by optical micrographs (Fig. 2). In Fig. 5, the same structures were observed when the samples tilted 30 degree of angle to the horizontal plane, revealing the height of the microfilter, which is estimated around 77 μm by geometry calculation. This is approximate to the height of the original 3D design.

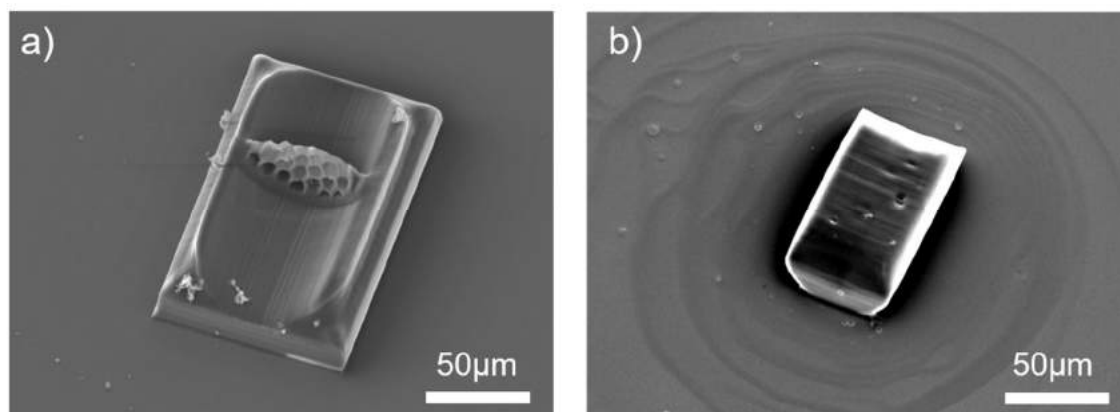


Fig. 5 SEM micrographs (tilt 30°) of the 3D-printed microstructures: a) microfilter and b) piston

Fig. 6 shows the microstructure of the filtering holes array. The sample was also tilted 30 degree to reveal the hexagonal shape of the hole and the honey comb structure or the array. The holes are confirmed well-shaped with hexagonal morphology, and their inner walls contain just a few artifacts whose small size may not hinder the transmittance of precious particles through the holes in filtering process. The average minimal diameter and maximal diameter estimated from the micrographs, are 3.9 μm and 7.2 μm , respectively. The inner wall between the holes, is thickest as 0.5 μm and thinnest as 0.8 μm . These parameters are in acceptable range of the deviation from the original design (see Fig. 2). In addition, it is confirmed that there is no any cracks or flaws appear on the filtering holes array as well as on the whole structures.

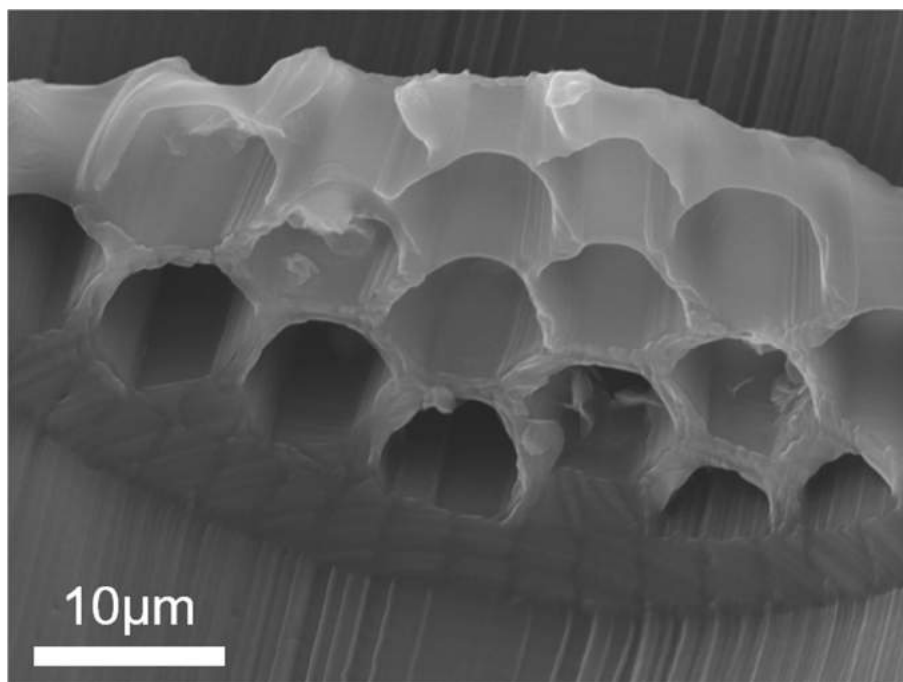


Fig. 6 High resolution SEM micrograph (tilt 30°) of the filtering holes array

Thus, we can conclude that the 3D-printing process of the MEMS was quite precise, and this MEMS is ready to be employed in filtering process.

4. Conclusion

In this paper, a MEMS designed for extracting precious matter on bacteria cell has been successfully fabricated by 3D-printing using TPA method. The sizes of the microfilter and piston are in consistent with the 3D design by SolidWorks, indicating that 3D-printing process was very precise. In addition, SEM observation confirmed that the honeycomb morphology of filtering holes was well-printed. The present results enable us to utilize this piston-and-filter system for sterilization applications. The next steps for this research are to apply an electric field onto the MEMS to control the piston movement, then employ that to extract the precious particles from bacteria cell. These experimental works are being conducted at Kushiro College and planned to be reported in future articles.

Acknowledgments

The authors are grateful to Mr. T. Eguchi of National Institute of Technology, Kushiro College for his assistance in SEM observation. This work was supported by Nagaoka University of Technology (NUT) Grant for collaborative research with National Institute of Technology (NIT).

References

- [1] Narendra Kulkarni and Uday Muddapur, "Biosynthesis of Metal Nanoparticles: A Review", *J. Nanotechnology*, vol. 2014, Article ID 510246, 2014.
- [2] Matthew D. Yates et al., "Extracellular Palladium Nanoparticle Production using *Geobacter sulfurreducens*", *ACS Sustain. Chem. Eng.*, vol. 1(9), pp. 1165-1171, 2013.
- [3] Praveen Sonkusre et al., "Improved Extraction of Intracellular Biogenic Selenium Nanoparticles and their Specificity for Cancer Chemoprevention", *J. Nanomed. Nanotechnol.*, vol. 5(2), Article ID 1000194, 2014.
- [4] Kevin Deplanche et al., "Involvement of hydrogenases in the formation of highly catalytic Pd(0) nanoparticles by bioreduction of Pd(II) using *Escherichia coli* mutant strains", *Microbiology*, vol. 156, pp. 2630-2640, 2010.

- [5] P. J. Fesharaki et al., “Biosynthesis of selenium nanoparticles using *Klebsiella pneumoniae* and their recovery by a simple sterilization process”, *Brazilian Journal of Microbiology*, vol. 41(2), pp. 461–466, 2010.
- [6] M. Gericle and A. Pinches, “Biological synthesis of metal nanoparticles”, *Hydrometallurgy*, vol. 83, pp. 123-140, 2006.
- [7] M. G. del R. Herrera Salazar et al., “Fabrication of Micro Three Dimensional Structures by Two Photon Polymerization with SiO/Resin”, *Advances in Science and Technology*, vol. 100, pp. 93–99, 2017.
- [8] Linjie Li and John T. Fourkas, “Multiphoton polymerization”, *Materials today*, vol. 10, no. 6, pp. 30-37, 2007.
- [9] H-B. Cho et al., “Self-assemblies of linearly aligned diamond fillers in polysiloxane/diamond composite films with enhanced thermal conductivity”, *Compos. Sci. Tech.*, vol. 72(1), pp. 112-118, 2011.
- [10] S. T. Nguyen et al., “Linear assembly of oxidized surface treated nanodiamonds in polymer-based nanohybrids by electric field inducement”, *Materials Science Forum*, vol. 761, pp. 107-111, 2013.
- [11] Genki Onishi et al, “Demonstration of motion control of ZrO_2 microparticles in uniform/non-uniform electric field”, *Jpn. J. Appl. Phys.*, vol. 57, 02CB11, 2018.
- [12] M.T.T. Huynh et al., “Electrical property enhancement by controlled percolation structure of carbon black in polymer-based nanocomposites via nanosecond pulsed electric field”, *Compos. Sci. Tech.*, vol. 154, pp. 165-174, 2018
- [13] M. G. del R. Herrera Salazar et al., “Development of Electrically Driven Microcar Using Two Photon Microfabrication”, presented at Annual Meeting of the Ceramic Society of Japan, Tokyo, Mar 2016.

(Received: 29 October 2018, Accepted: 20 December 2018)

Optimization of Mirror Magnetic Fields in a Permanent Magnet ECR Ion Source for Generation of Multi-Charged Aluminum Ions

Tsubasa Nakamura^{1,*}, Shinji Yamada², Takumi Tomonari³, Ayumu Inagaki⁴, Hiroya Uyama⁵,
Yuta Wada⁶, Toyohisa Asaji⁷, Kazumasa Takahashi⁸, Toru Sasaki⁸

¹⁾ Department of Electronic-Mechanical Engineering, National Institute of Technology, Oshima College,

²⁾ Department of Electronic and Information Technology System, National Institute of Technology, Oshima College,

³⁾ Department of Mechanical-Environmental System, National Institute of Technology, Oita College,

⁴⁾ Department of Mechanical Engineering, National Institute of Technology, Oita College,

⁵⁾ Department of ECDesign Engineering Course, National Institute of Technology, Toyama College,

⁶⁾ Department of Nuclear System Safety Engineering, Nagaoka University of Technology,

⁷⁾ Department of Mechanical Engineering, National Institute of Technology, Toyama College,

⁸⁾ Department of Electrical, Electronics and Information Engineering, Nagaoka University of Technology,

1091-1 Komatsu Suo-Oshima-tyo, Yamaguchi, Japan 742-2193

*E-mail: d814@oshima-k.ac.jp

We assumed the development of ion injection technology as a background in the semiconductor manufacturing process. We carried out the study aiming at optimization of Ar⁷⁺ and improvement of the generation efficiency. By lowering the pressure in the chamber, the electric current of Ar⁷⁺ was about 130 nA. It improved to approximately 10 times in comparison with previous results. When we changed the magnetic field by a solenoid coil, it improved to about 3.6 times in comparison with that without any change. The improvement of the optimization and generation rate was able to be accomplished than the above. In addition, following three parameters affect the generated ion beam electric current: confinement time of the ion, ions charge state and electronic density and plasma volume.

1. Introduction

In semiconductor manufacturing, ion injection to dope the substrate material has become an indispensable technique in recent years. Among the semiconductor industries, in particular, the market for power semiconductors is growing rapidly. Power semiconductor production and related techniques have become indispensable for electricity conversion and control. Development of a technique for ion injection of aluminum to SiC, which is the substrate material, has become the key for performance improvement of these devices. In this study, we aimed at developing a technology for generation of aluminum multi-charged ions, with improvement of the ion beam current and reduction of the acceleration voltage of the device. The main features of the study are as follows: 1) The ionization energies of Ar⁷⁺ and Al⁴⁺ are nearly same (Ar⁷⁺: about 124 eV, Al⁴⁺: about 120 eV). Therefore, we detect Ar⁷⁺ ion, which is in gaseous state. 2) We improve the ion beam electric current of Ar⁷⁺.

2. Electron Cyclotron Resonance Ion Source

An electron cyclotron resonance (ECR) ion source has been developed as a high intensity multivalent ion beam supply device. Characteristics can be changed by using a semiconductor element and irradiating ions, and material strength can be improved. Therefore, the ECR ion source device is currently used in a wide range of fields. Especially, the ECR ion source is an indispensable technology for ion implantation in semiconductor manufacturing and has played a key role in activating the power semiconductor market in recent years.

The ECR ion source confines the plasma in the chamber and uses a permanent magnet to introduce microwaves into the chamber. Electrons in the plasma are then accelerated by electron cyclotron resonance. This device constantly removes electrons from atoms and ions to generate multi-charged ions.

Multi-charged ion refers to a state in which two or more electrons are removed from the atom. As the number of electrons removed increases, it becomes easier to accelerate them. Plasma is formed by the generated ions and electrons coexisting in the chamber; the ions and electrons are separated by applying voltage to the chamber, and only the ions are extracted as a beam. Multi-charged ions are more easily accelerated than normal ions, so if the multi-charged ions are increased in number and stabilized, the acceleration voltage applied during ion implantation can be lowered, which reduces the cost. Therefore, studies multi-charged ions are currently being undertaken.

In a typical ECR ion source, the magnetic field is formed by a set of solenoid coils (mirror magnetic field) and 6 pole magnets and the plasma are confined. On the other hand, the Oshima-ECR ion source used in our laboratory has a ring-shaped permanent magnet and an 8-pole permanent magnet. In addition, three solenoid coils are used that can adjust the magnetic field in the chamber. Thus, the ability to adjust the magnetic field in the chamber is one of the features of the Oshima-ECR ion source [1]. The Oshima - ECR ion source is used in our laboratory to generate multi-charged ions.

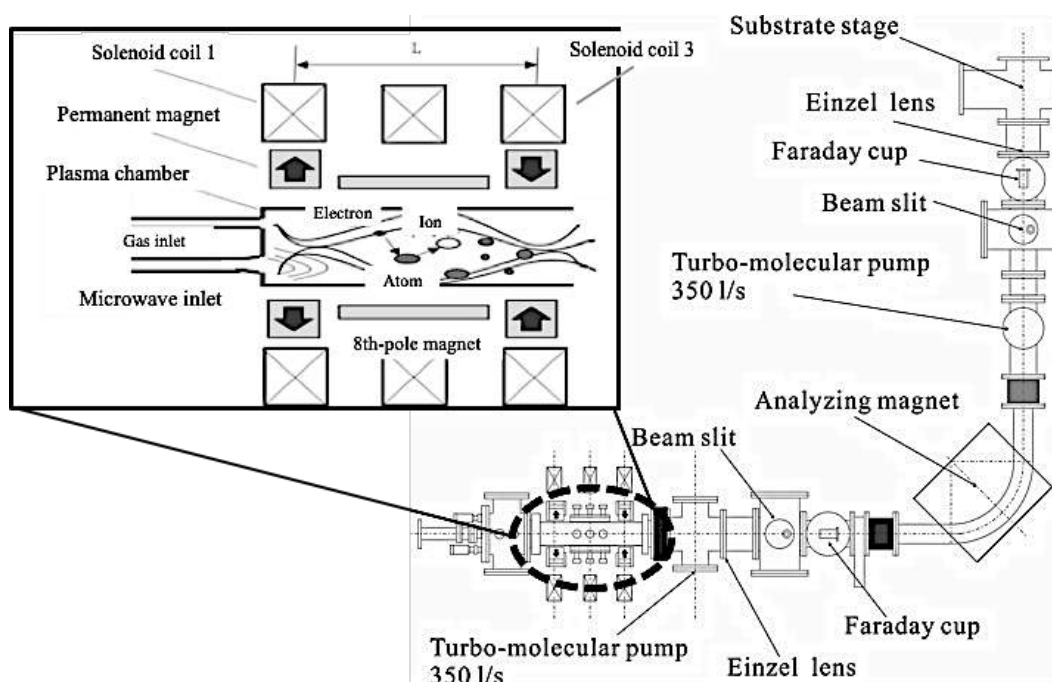


Fig. 1 Schematic view of the Oshima-ECR ion source

3. Experimental Setup

The experimental procedure is explained with reference to the schematic of the Oshima-ECR ion source shown in Fig. 1.

While keeping the Oshima-ECR ion source at vacuum (about 10^{-5} Pa), plasma is generated at the lower left ECR ion source. As a buffer gas for this purpose, argon gas is flowed at 0.01 sccm (standard cc/min); this is because the ionization energy of Al^{+4} (about 120 eV) is close to that of Ar^{+7} (about 124 eV) and therefore, the Oshima-ECR ion source can generate Al^{4+} theoretically, by observing Ar^{7+} . Ar gas is not necessary to vaporize it. Ar gas is not necessary to vaporize it to ionize. Thereafter, a microwave (2.45 GHz) is applied to generate plasma in the chamber. Then, a high voltage is applied into the chamber, and multi-charged ions generated in the chamber are extracted by electron cyclotron resonance.

The extracted multi-charged ions consist of various components and are passed through an analysis magnet. The emergent ion beam is measured in a Faraday cup to determine the ion beam electric current.

The ion beam electric current can be optimized in the Oshima-ECR ion source through adjusting the magnetic field in the chamber by using solenoid coils. Figure 2 shows the change of the magnetic field in the chamber. In addition, the background of the Figure 2 is shown the figure of the chamber. The reason is to make it easy to understand the magnetic field distribution in the chamber (positional relationship with Z axis.). This figure indicates that when the electric current flowing in solenoid coil 1 increases, the magnetic field of the chamber (the microwave applying side) becomes strong; as the electric current of solenoid coil 3 increases, the magnetic field (the drawer electrode side) becomes weak.

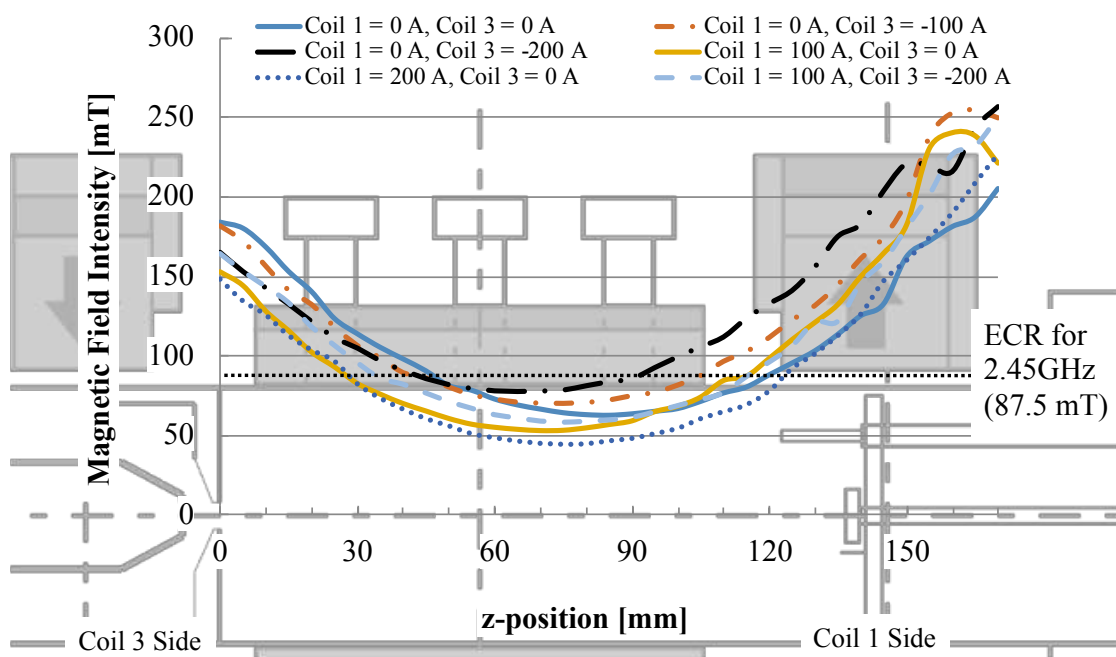


Fig. 2 Magnetic field change in the chamber

4. Experiment Parameters

On the upstream side of the Oshima-ECR ion source, we added a turbo molecular pump (Osaka Vacuum Equipment Manufacturing TG 50 F), as shown in Fig. 3, to lower the vacuum pressure in the chamber and minimize the buffer gas flowing into the chamber.

As a result, it was possible to lower the pressure in the chamber for generating plasma from 7.71×10^{-5} Pa (before expansion) to 2.73×10^{-5} Pa (after expansion).

Thereafter, argon was used as a buffer gas, and the ion beam current was measured. The experimental parameters are shown in Table 1. For a comparison, the parameters before installing the turbo molecular pump are also listed.

Next, we changed the magnetic field in the chamber in the parameter that optimized in Ar^{7+} (parameter are solenoid coil 1 and 3) and estimated the corresponding change in the ion beam electric current. The experimental parameters are shown in Table 2.

Table 1 Influence of pressure drop in the chamber

	20171027-09 (before expansion)	20171201-01 (after expansion)
Ion source pressure	7.71×10^{-5} Pa	2.73×10^{-5} Pa
Beam line pressure	4.28×10^{-5} Pa	2.69×10^{-5} Pa
Microwave power (I/O)	80 W/6 W	80 W/7 W
Buffer gas/flow rate	Ar/0.01 sccm	Ar/0.01 sccm
Chamber voltage/current	5 kV/2.56 mA	5 kV/1.30 mA
Einzel lens voltage/current	3.8 kV/2.10 mA	3.8 kV/0.70 mA

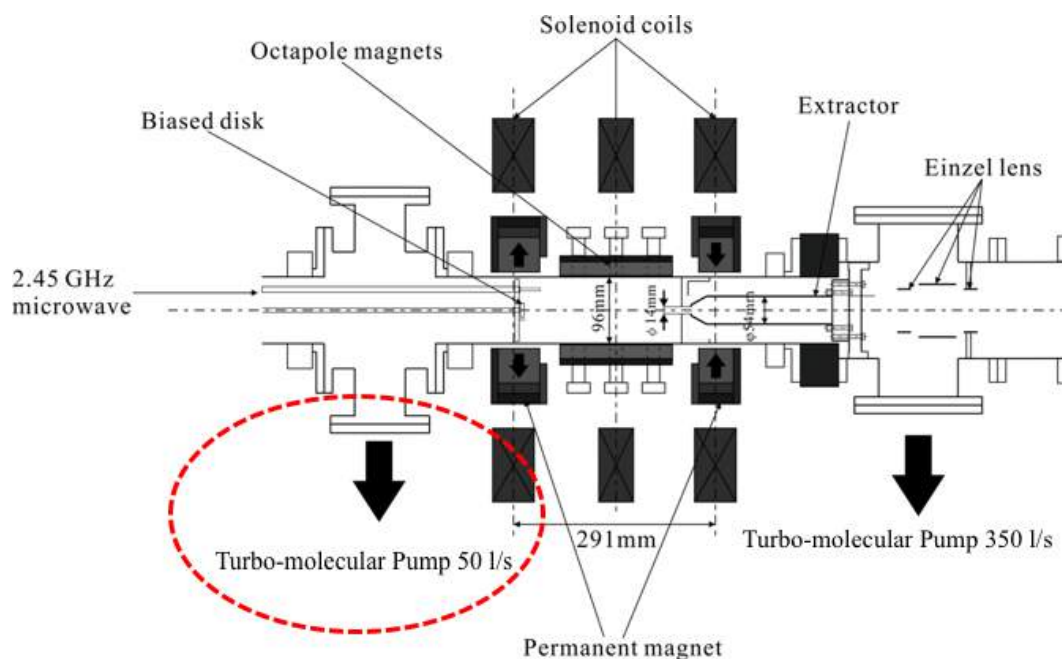


Fig. 3 Setting point of the turbo molecular pump

Table 2 Change in the ion beam electric current when the magnetic field in the chamber is changed

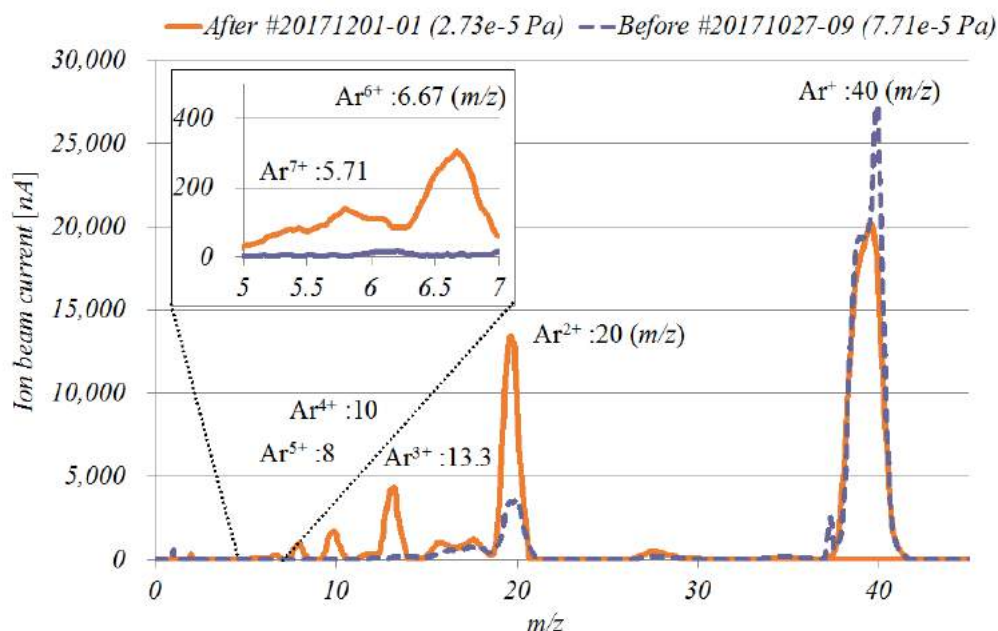
Ion source pressure	1.03×10^{-5} Pa
Beam line pressure	5.74×10^{-5} Pa
Microwave power (I/O)	100 W/6 W
Buffer gas/flow rate	Ar/0.01 sccm
Chamber voltage/current	5.05 kV/1.68 mA
Einzel lens voltage/current	3.52 kV/0.61 mA
Current of solenoid coil 1 and 3	0, 50, 100, 150, 200 A

5. Results and Discussion

5.1. Influence of pressure drop in the chamber

The results are shown in Fig. 4. The ion beam current of Ar^{7+} was about 20 nA before the installation of the turbomolecular pump, and reached about 130 nA after expansion, which is an increase of about 6.5 times. In addition, the generation amount of argon multi-charged ions could be substantially improved.

The reason behind the increase in the amount of generated argon multi-charged ions is as follows. Reducing the pressure in the vacuum chamber reduces the number of molecules in the chamber. Then, the collision frequency with electrons decreases, and the ion lifetime increases. As a result, the ion beam current of multi-charged ions could be improved.

**Fig. 4** Comparison of the argon spectrum waveform.

5.2. Change in the ion beam electric current

We flew an electric current to solenoid coil 1 and 3 and changed the magnetic field in the chamber. An example of the spectrum wave pattern is shown in Fig. 5. The blue line represents 100 A (solenoid coil 1) and 0 A (solenoid coil 3). The red one indicates corresponding values of 100 A and -150 A.

The electric current of Ar⁺⁷ from this result is approximately 50 nA and 100 nA. Thus, a difference of approximately 2 times occurred. This indicates that the ion beam electric current is changed by changing the magnetic field in the chamber.

The change of the ion beam electric current of Ar⁺⁷ when we changed the magnetic field in the chamber is shown in Fig. 6.

When solenoid coil 1 current is constant, it becomes easy to draw the ion beam because the electric current of solenoid coil 3 is large (the magnetic field in the extraction side of the chamber weakens.). Therefore, we expected that the ion beam electric current will increase, but such correlation was not seen. From the result, when the electric current of solenoid coil 3 was -150 A, the ion beam electric current of Ar⁺⁷ was about 100 nA (maximum).

Therefore, in this study, the maximum ion beam current can be obtained when the solenoid coil 1 and 3 are set to 100 A and -150 A, respectively.

The ion beam electric current considers a reason to change by adjusting the magnetic field in the chamber in this way.

The ion beam electric current of the multi-charged ions is calculated using the following equation [2].

$$I_q \cong \frac{1}{2} \frac{n_q q e V \omega l}{\tau_q} \quad (1)$$

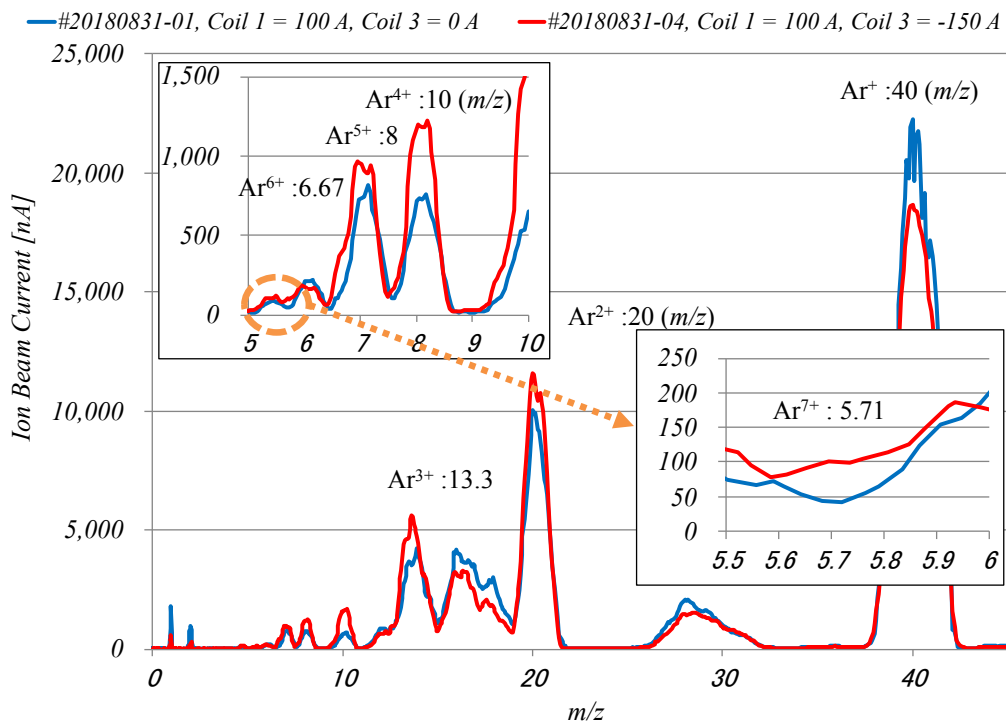


Fig. 5 Spectrum wave pattern example when the magnetic field in the chamber is changed.

Here, n_q is density of the ions of charge state q ; τ_d the confinement time of these ions depending on potential dip $\Delta\phi$; Vol is the part of the hot-plasma volume that maps along the magnetic field lines into the extraction area.

From this equation, if the confinement time of ion is short, the ion beam electric current will increase. Otherwise, it is necessary to increase the density and the plasma volume of atomic value q . Therefore, the magnetic field of the extraction electrode side weakens and the ion enclosure time thereby shortens; thus, the ion beam electric current increases.

The reasons that cause a decrease in the ion beam electric current are stated below.

Assuming plasma charge neutrality

$$n_e = \sum_q n_q q \quad (2)$$

Using this equation and equation 1, we get equation 3.

$$I_q \propto n_e \frac{Vol}{\tau_d} \quad (3)$$

Thus, the production of high-intensity I_q , high-charge-state q ions results in a compromise between the ionization conditions and the plasma confinement condition [2]. In addition, in plasma confined in an electromagnetic field, as for the ion, the possibility of recombination with electrons increases.

As a result, an electron is drawn in the opposite side of the extraction electrode. However, a part is left in the plasma without being drawn under the influence of the magnetic field in the chamber. Recombination with the ion occurs, which is thought to reduce the ion beam electric current.

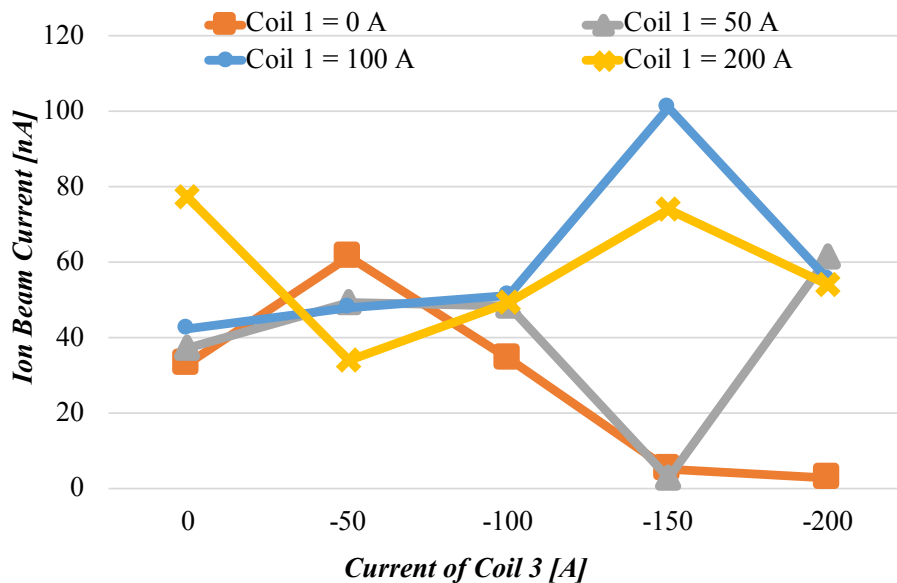


Fig. 6 Change of the ion beam electric current by change in the magnetic field in the chamber.

6. Conclusion

We assumed the development of ion injection technology as a background in semiconductor manufacturing process. We carried out this study for the following purposes. 1) The ionization energies of Ar^{7+} and Al^{4+} are nearly same (Ar^{7+} : about 124 eV, Al^{4+} : about 120 eV). Therefore, we detect an ion of Ar^{7+} which is gas. 2) We improve the ion beam electric current of Ar^{7+} . It succeeded in the detection of Ar^{7+} which we targeted by lowering the pressure in the chamber. The electric current was about 130 nA. Regarding the improvement of the generation of Ar^{7+} , we were able to optimize it by adjusting the magnetic field in the chamber. From the results of this study, a current of about 100 nA maximum is produced when the currents of solenoid coil 1 and 3 are 100A and -150 A, respectively. In addition, following three parameters influence the generated ion beam electric current: confinement time of the ion, ions of charge state and electronic density and plasma volume.

Acknowledgments

This study was supported by the Nagaoka University of Technology (NUT) grant for collaborative research with National Institute of Technology (NIT).

References

- [1] T. Nakamura, et al., Effect of axial magnetic field on a 2.45 GHz permanent magnet ECR ion source, Review of Scientific Instruments, 87(02A737), 2015.12
- [2] R. Geller, Electron Cyclotron Resonance Ion Source and ECR Plasmas, Institute of Physics Publishing, Bristol, p.370, 1996.

(Received: 15 October 2018, Accepted: 22 February 2019)

Purification and Antigenicity Evaluation of Fish-Disease Bacterial Outer Membrane Proteins for Immersion Vaccine Development

Noriyo Mitome^{1*}, Nagisa Hamada², Naoki Yamashita², Seng Eng Khuan³

¹Department of Chemistry and Biochemistry, National Institute of Technology, Numazu College, 3600 Ooka, Numazu city, Shizuoka, 410-8501, Japan

²Department of Chemical and Biological Engineering, National Institute of Technology, Ube College, 2-14-1 Tokiwadai, Ube city, Yamaguchi, 755-8555, Japan

³School of Chemical and Life Sciences, Nanyang Polytechnic, 180 Ang Mo Kio Avenue 8 Singapore, 569830, Rep. of Singapore

*E-mail: mitome@numazu-ct.ac.jp

The pathogenic marine bacterium, *Edwardsiella tarda*, causes the fatal disease, edwardsiellosis, in fish. Owing to the unavailability of a commercial vaccine to prevent infection or the spread of the disease in fish stock, fish farms suffer huge losses during edwardsiellosis outbreaks. Herein, we describe a platform technology, i.e., a nanovaccine, to vaccinate fish and other animals. Nanovaccines require specific antigens, such as the bacterial outer membrane proteins (OMPs) carried around and inside nanoparticles, to act as vaccines. In this study, we developed a rapid and inexpensive method for the isolation and purification of OMPs from marine bacteria and demonstrated the antigenicity of the purified OMPs using Koi carp (*Cyprinus carpio*). The purified OMPs were then incorporated into the nanoparticles to generate a nanovaccine. Nanovaccinated Koi carp produced antibodies against the OMPs of *E. tarda*. We propose that the OMP purification method used in the present study is useful for the production of nanovaccines and that such techniques are simple to apply and effective to prevent disease outbreaks in fish farms.

1. Introduction

Owing to the rapid expansion of aquaculture, several farms now stock fish at a very high density. The close proximity of fish and the occurrence of natural pathogens in the aquatic environment increase the frequency of disease outbreaks, which may reduce fish stocks causing huge losses to fish farms [1][2]. To overcome diseases, vaccines have been used as they can provide long-term protection. In fact, the administration of fish vaccines has prevented the loss of fish in fish farms due to disease outbreaks, enabling higher fish yield [3].

The current modes of vaccine administration include injection, oral administration, and immersion. Injection vaccines are administered intramuscularly or intraperitoneally (in the abdominal cavity). They provide long-term protection, i.e., for over a year, and allow multiple antigens to be combined in a single vaccine and thus in a single administration. Despite these advantages, the administration of vaccines via injection is an expensive method because of the heavy dependence on skilled manpower. Moreover, it has a high risk of causing accidental injury to the fish and personnel. Furthermore, injection vaccines can only be administered when fish weigh > 10 g, and therefore, smaller fishes cannot be vaccinated and thus remain unprotected from diseases.

Oral vaccines are either administered in the feed (mixed in or coated) or bio-encapsulated. Oral vaccines have more advantages as they can be easily administered, cause no stress to the fish, require low labor investment, and can be applied at a large scale. However, oral vaccines have a very short-term stability once mixed with the feed [4]. In addition, several oral vaccines have been found to be ineffective due to the failure of fish to uptake a sufficient antigen dosage, and poor antigen delivery and degradation in the digestive tract [4]. In most cases, only limited and short-term protection is offered. Moreover, the injection of vaccine directly into an individual fish is preferred over oral administration as a defined quantity of vaccine can be administered leading to longer protection.

Immersion vaccination involves the functionality of mucosal surfaces. When fish are immersed in water containing the diluted vaccine, the suspended antigens from the vaccine are adsorbed on to the skin and gills [5]. Specialized cells, such as antigen-presenting cells present in the skin and gill epithelium, are consequently activated and thus protect the fish when they are exposed to live pathogen at a later stage. It is an effective method that results in relatively good protection. Although, immersion vaccination is sometimes protective, not many effective immersion vaccines are currently available for use.

The pathogenic marine bacterium *Edwardsiella tarda* causes parasitological diseases or edwardsiellosis in cultured Japanese eel, flounder, red sea bream, and tilapia [6][7]. A vaccine against *E. tarda* has been pursued for several years; however, a practical and commercially available vaccine has not been developed. Only the attenuated vaccine for *Edwardsiella ictaluri* is commercially available in the USA. Moreover, a recent report has indicated that an outer membrane protein (OMP), i.e., glyceraldehyde 3-phosphate dehydrogenase (GAPDH), from *E. tarda* is an effective vaccine candidate against *E. tarda* [8]. In addition, the nanovaccine platform technology has been described for use in vaccinating fish and other animals [9]. Nanovaccines require a specific antigen, such as the OMPs of bacteria carried around and inside the nanoparticles, to act as vaccines.

There are several methods to purify the OMPs. For example, porin, which is a typical OMP, has been purified by selective solubilization because porin is tolerant to strong detergents such as sodium dodecyl sulfate (SDS) [10]. Porin has also been purified by ion exchange and gel filtration with octyl-POE [11]–[16] or by selective solubilization and gel filtration with LDAO and C8E4 [17]–[19]. Ferric enterobactin receptor (FepA) has been purified by selective solubilization with Triton X-100 in the absence and presence of EDTA [20]. Most of the OMPs can be extracted with Triton X-100 and EDTA.

In this study, we developed a quick and low-cost method to isolate and purify the OMPs from marine bacteria and demonstrated the antigenicity of the purified OMPs. The purified OMPs were then incorporated into nanoparticles to develop a nanovaccine.

2. Experiments

Preparation of formalin-inactivated vaccine and evaluation of antigenicity

Edwardsiella tarda (NBRC 105688) cells were first cultured on a plate of NBRC medium No. 802 (containing 1% hipolypepton, 0.2% yeast extract, 0.1% MgSO₄·7H₂O, and 1.5% agar) at 30 °C for 24 h. The cells were then cultured in 100 mL of NBRC medium No. 802 at 30 °C for 24 h. The cultured *E. tarda* cells were diluted with sterilized physiological saline to obtain the OD₆₆₀ of 8.0. The bacteria cells were inactivated with formalin (1%) for 24 h at 4 °C. The inactivated cells were then stored in sterilized physiological saline with 0.1% formalin. The bacterial cell suspension was used as a vaccine in the subsequent experiments.

Koi carp (*Cyprinus carpio*) (n = 6), with an average body weight of 20 g, were housed in aquariums (30 L capacity) and were divided into three immune carp groups (tanks) and three control carp groups. A mixture of vaccine and sunflower oil (1:2) was prepared, and then 100 µL of the mixture was injected into the abdomen of the carp. After 10 days, a booster dose (100 µL) was injected. In the control group, the carp were similarly injected with a mixture of sterile physiological saline and sunflower oil (1:2).

On the 21st day after the first vaccination, blood samples (200 µL) were collected using the standard venipuncture technique. The blood samples were incubated at 4 °C for 24 h and serum samples were obtained by centrifuging the blood samples at 3000 × g for 10 min. Antigenicity was confirmed using the dot blot method.

Cultivation of *E. tarda* and preparation of membrane fraction

Edwardsiella tarda cells were first cultured on a plate of NBRC medium No. 802 at 30 °C for 24 h. Subsequently, the cells were precultured in 100 mL of NBRC medium No. 802 at 30 °C for 6 h, and then 100 mL of preculture was added to 1 L of NBRC medium No. 802 and cultured at 30 °C for 16 h [6]. The bacterial cells were collected by centrifugation at 6500 × g for 5 min at 4 °C, washed in 200 mL of 10 mM Tris-HCl buffer pH 8.0, and collected again by centrifugation at 6500 × g for 5 min at 4 °C. We collected 20 g of bacterial cells from 1 L of culture, froze the cells using liquid nitrogen, and stored them at -80 °C. The bacterial cells were suspended in 10 mM Tris-HCl buffer of pH 8.0 using

4 mL of the buffer per gram of cells and disrupted by sonication. After removal of debris by centrifugation at $6500 \times g$ for 10 min at 4 °C, the membrane fraction was collected from the supernatant by ultracentrifugation at $200,000 \times g$ for 30 min at 4 °C. The membrane fraction was suspended in 10 mM Tris-HCl buffer using the same volume as the weight of the starting cells, and stored at -80 °C.

Solubilization of membrane proteins

The membrane fraction was suspended in 10 mM Tris-HCl with 2% Triton X-100, incubated at 32 °C for 30 min, and ultra-centrifuged at $200,000 \times g$ for 30 min at 32 °C [20]. The supernatant (Triton extraction) was stored at -80 °C to determine protein purity. The pellet (Triton insoluble fraction) was suspended in 10 mM Tris-HCl with 2% Triton X-100 and 5 mM EDTA, incubated at 32 °C for 30 min, and ultra-centrifuged at $200,000 \times g$ for 30 min at 32 °C. The supernatant (Triton/EDTA extraction) was frozen using liquid nitrogen and stored at -80 °C for use in the preparation of nanovaccine. The pellet (Triton/EDTA insoluble) was suspended in 10 mM Tris-HCl with 2% SDS, incubated at 32 °C for 30 min, and ultra-centrifuged at $200,000 \times g$ for 30 min at 32 °C. The supernatant (SDS soluble) and the pellet (SDS insoluble) were stored at -80 °C until further analyses. The Triton/EDTA extract (2 mL of 1 mg/mL) was dialyzed twice with 2 L of phosphate-buffered saline (PBS) to dilute the detergent.

SDS-PAGE analysis of proteins

To confirm the purity of proteins, SDS polyacrylamide gel electrophoresis (SDS-PAGE) was carried out by separating 15 µg of proteins on 12.5% gels. The proteins were confirmed by staining with Coomassie brilliant blue.

Proteins quantification

Protein quantification was conducted by Bradford method using a standard solution of bovine serum albumin (BSA) of known concentration.

Generation of nanoparticles containing bacterial OMPs

The mixture (20 mL) containing 50 mg/mL chitosan–clay and 100 µg/mL of the OMPs in PBS was frozen using liquid nitrogen and dried using a freeze dryer (VirTis). The dry particles were suspended in 20 mL of distilled water.

We analyzed the amount of proteins that could be absorbed by the chitosan–clay nanoparticles. We mixed 100, 200, and 500 µg/mL of dialyzed OMPs with 50 mg/mL of nanoparticles individually. These mixtures were then frozen using liquid nitrogen and dried using a freeze dryer. After freeze drying, the chitosan–clay powder containing the OMPs was suspended in distilled water to form the nanovaccines. To confirm the absorption of OMPs to the nanoparticles, we quantified the proteins in the supernatant after centrifugation at $6000 \times g$ for 1 min.

Vaccination

Five milliliters of 50 mg/mL chitosan–clay suspension with or without 100 µg/mL OMPs were added to 1 L of freshwater in which the fish were allowed to swim for 30 min. The vaccinated and non-vaccinated fish were grown in separate aquariums. On the 21st day after the first vaccination, 200 µL of blood was collected from three carp in the control and treatment groups using the standard venipuncture technique. The blood samples were incubated at 4 °C for 24 h and serum samples were obtained by centrifuging the blood samples at $3000 \times g$ for 10 min. The antigenicity of the nanovaccine was confirmed by immunoblotting. The OMPs from *E. tarda* were separated by SDS-PAGE and transferred on to immunoblot-designed polyvinylidene difluoride membranes. The membranes were then blocked with PBS with 1% BSA at 4 °C overnight, followed by incubation with the serum, which was obtained from vaccinated carp, diluted to 0.2% in PBS for 1 h at 4 °C. The membranes were then washed three times with PBS for 5 min each. The incubation with secondary antibodies was conducted for 30 min with 1% secondary antibody conjugated with horseradish peroxidase (Anti-IgM, Carp/Koi Carp (*C. carpio*), Mouse-Mono, HRP) in PBS at 4 °C. The bands were visualized using ECL Plus Western Blotting Detection Reagents (GE Healthcare).

3. Results and Discussion

Formalin-inactivated *E. tarda* were injected into live carp. After three weeks, blood samples were

collected to obtain serum samples. The results of the dot blot analysis showed that *E. tarda* cells were stained in the serum from carp that were vaccinated with formalin-inactivated *E. tarda* (Fig. 1). On the contrary, *Vibrio* sp. was not stained in the serum from carp vaccinated with formalin-inactivated *E. tarda*. Whereas, *Vibrio* sp. was stained in the serum from carp vaccinated with formalin-inactivated *Vibrio* sp. Contrarily, *E. tarda* cells were not stained in the serum from carp vaccinated with formalin-inactivated *Vibrio* sp. These results suggested that the formalin-inactivated vaccine of *E. tarda* was bound to *E. tarda* and that the formalin-inactivated vaccine of *Vibrio* sp. was bound to *Vibrio* sp.

The extraction procedure was primarily based on selective solubilization of inner MPs and OMPs with Triton X-100 in the absence and presence of EDTA [16]. The inner membrane proteins were solubilized with Triton X-100 (Fig. 2). The Triton-insoluble fractions mostly contained the OMPs. Some of the OMPs were extracted by Triton and EDTA. The 97-, 43-, 40-, and 37-kDa proteins were visible in this fraction (Fig. 2). The purified OMPs included several proteins, namely, 97, 43, 40, and 37 kDa. These proteins were the same as those reported extracted using SDS in a previous study [21]. Especially, the 37-kDa protein, GAPDH, has been reported to be a candidate for vaccination [20]. In the present study, we demonstrated that it is possible to purify GAPDH and other candidate OMPs using this purification method for vaccine preparations. In the purification of OMPs, SDS is often used [21]. However, detergents, especially anionic detergents, such as SDS, which denature proteins are harmful to fish. Therefore, we used the non-ionic detergent, Triton with EDTA instead of SDS for the purification of OMPs. Although dialysis resulted in the dilution of Triton, the direct vaccination of OMPs at a concentration of 0.1% of the body weight resulted in the mortality of fish.

The purified OMPs were used to prepare the nanovaccine. Although several proteins were included in the Triton and EDTA extract, we considered the use of a simple purification method to enable practical application and to reduce cost.

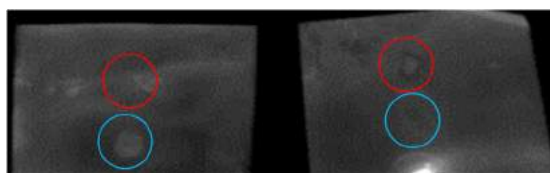


Fig. 1 Dot blot analysis. Top circles: Spotted with *E. tarda*. Bottom circles: Spotted with *Vibrio* sp. Left: Spotted bacteria were probed with the serum sample from Koi carp (*Cyprinus carpio*) vaccinated with *Vibrio* sp. Right: Spotted bacteria were probed with the serum sample from carp vaccinated with *Edwardsiella tarda*.

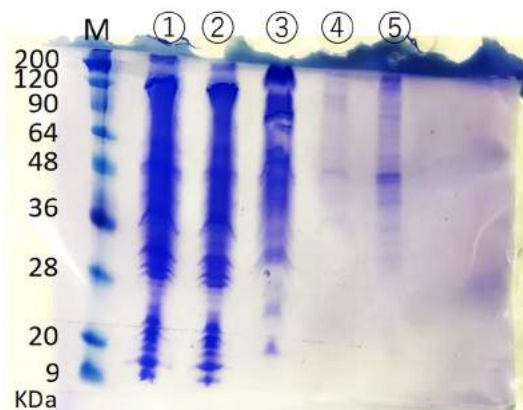


Fig. 2 Coomassie brilliant blue-stained gel of the inner and outer membrane proteins. 1. Membrane fraction. 2. Triton extract. 3. Triton insoluble. 4. Triton/EDTA extract. 5. Triton/EDTA insoluble.

Proportion of chitosan–clay and OMPs

We mixed the OMPs at various concentrations with chitosan–clay at a constant concentration of 50 mg/mL. Table 1 shows the estimated absorption of OMPs by chitosan–clay. When 100 µg/mL OMPs was added, almost all proteins were absorbed by 50 mg/mL nanoparticles. When 400 µg/mL OMPs was added, only 300 µg/mL OMPs was absorbed. These findings suggested that the addition of 100–300 µg/mL OMPs to 50 mg/mL chitosan–clay is suitable to manufacture a nanovaccine with 100–200 µg/mL OMPs.

Table 1 Amount of absorbed outer membrane proteins by the nanoparticles.

100 $\mu\text{g/mL}$ (a), 200 $\mu\text{g/mL}$ (b), and 500 $\mu\text{g/mL}$ (c) OMPs were mixed with 50 mg/mL nanoparticles. After freeze-drying, the chitosan–clay powder that contained the OMPs was suspended in distilled water and the proteins in the supernatant were quantified after centrifugation.

	a	b	c
Concentration of chitosan–clay (mg/mL)	50	50	50
Concentration of outer membrane protein ($\mu\text{g/mL}$)	50	100	400
Protein concentration of supernatant ($\mu\text{g/mL}$)	0.0	0.0	95.6
Estimated concentration of absorbed protein in nanoparticle ($\mu\text{g/mL}$)	50	100	304.4

Three carp were treated with nanoparticles with (nanovaccine) or without (nanoparticle only) the OMPs (Fig. 3). The administration of prepared nanovaccines, in which the detergents were diluted,



Fig. 3 Immersion vaccination for carp. Five milliliter suspensions of 50 mg/mL chitosan–clay with or without 100 $\mu\text{g/mL}$ outer membrane proteins were added to 1 L of freshwater in which the study fish were allowed to swim for 30 min.

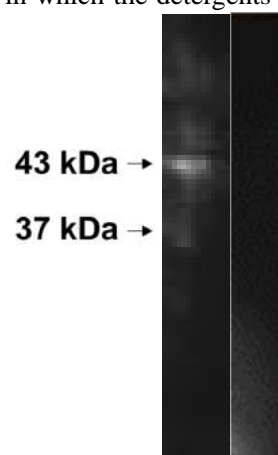


Fig. 4 Evaluation of the production of antibodies in the serum by immunoblotting. The outer membrane proteins from *E. tarda* were separated by SDS-PAGE and transferred on to membranes. The membranes were treated with the serum obtained from the blood samples of vaccinated carp (left) and nonvaccinated carp (right) and secondary antibody conjugated with horseradish peroxidase. Bands appeared at 43, 40, and 37 kDa.

was demonstrated to be safe, i.e., none of the nanovaccinated carp died. After three weeks, blood was collected from the carp and the production of antibodies was determined via immunoblotting. The bacterial OMPs were stained in the blood serum. Bands appeared at 43, 40, and 37 kDa in the serum from nanovaccinated carp. This suggested that the carp produced antibodies against the OMPs in the serum.

4. Conclusions

In this study, we developed a quick and low-cost method to isolate and purify the OMPs from marine bacteria and demonstrated the antigenicity of the purified OMPs. The purified OMPs were then incorporated into nanoparticles to develop a nanovaccine. We propose that our method of purification of OMPs is useful for nanovaccine production and that the use of nanovaccine technology can prevent disease outbreaks and the consequent production losses in fish farms.

Acknowledgments

We thank Dr. Saji George for the helpful discussions. We thank Ms. Anis Muthalib and Mr. Naoki Yamashita for their technical assistance. This study was supported by the Japan Society for the Promotion of Science (JSPS) KAKENHI (Grant Number 17K07922).

References

- [1] M. Hikida, H. Wakabayashi, S. Egusa, and K. Masumura, "Flexibacter sp., a gliding bacterium pathogenic to some marine fishes in Japan." *Bull Jpn Soc Sci Fish* 1979, 45(4):421-428.
- [2] T. Aoki and T. Kitao, "Drug resistance and transferable R plasmids in *Edwardsiella tarda* from fish culture ponds." *Fish Pathol* 1981, 15(3-4):277-281.
- [3] A. E. Ellis, "Current aspects of fish vaccination." *Dis Aquat Org* 1988, 4:159-164.
- [4] C.W. Embregts and M. Forlenza, "Oral vaccination of fish: successes, challenges and future perspectives." *Dev Comp Immunol* 2016, 64:118-137.
- [5] M. Ashraf, M. Akkukur, R. Sharma, and S. Ahmad, "Nanotechnology as a novel tool in fisheries and aquaculture development: a review." *Iran J Energy Environ* 2011, 2(3):258-261.
- [6] T. Miyazaki and N. Kaige, "Comparative histopathology of edwardsiellosis in fishes." *Fish Pathol* 1985, 20(2-3):219-227.
- [7] R. Kusuda and F. Salati, "Major bacterial disease affecting mariculture in Japan" *Ann Rev Fish Dis* 1993, 3:69-85.
- [8] K. Kawai, Y. Liu, K. Ohnishi, and S. Oshima, "A conserved 37 kDa outer membrane protein of *Edwardsiella tarda* is an effective vaccine candidate." *Vaccine* 2004, 22(25-26):3411-3418.
- [9] D. Rawtani and Y.K. Agarwal, "Multifarious applications of halloysite nanotubes: a review." *Rev Adv Mater Sci* 2012, 30(3): 282-295
- [10] T. Nakae, J. Ishii, and M. Tokunaga, "Subunit structure of functional porin oligomers that form permeability channels in the outer membrane of *Escherichia coli*." *J Biol Chem* 1979, 254(5):1457-1461.
- [11] S. W. Cowan, G. Schirmer, M. Steiert, R. Ghosh, R.A. Pauptit, J. N. Jansonius, and J.P. Rosenbusch, "Crystal structures explain functional properties of two *E. coli* porins." *Nature* 1992, 358:727-733.
- [12] R. M. Garavito and J. P. Rosenbusch, "Isolation and crystallization of bacterial porin." *Meth Enzymol* 1986, 125:309-328.
- [13] R. A. Pauptit, H. Zhang, G. Rummel, T. Schirmer, J. N. Jansonius, and J. P. Rosenbusch, "Trigonal crystals of porin from *Escherichia coli*." *J Mol Biol* 1991, 218(3):505-507.
- [14] M. Bruen, H. Engelhardt, A. Schmid, and R. Benz, "The major outer membrane protein of *Acidovorax delafieldii* is an anion-selective porin." *J Bacteriol* 1991, 173(13):4182-4187.
- [15] K. Zeth, K. Diederichs, W. Welte, and H. Engelhardt, "Crystal structure of Omp 32, the Anion-selective porin from *Comamonas acidovorans*, in complex with a periplasmic peptide at 2.1 Å resolution." *Structure* 2000, 8:981-992.
- [16] K. Zeth, and V. Schnaible, M. Przybylski, W. Welte, K. Diederichs, and H. Engelhardt, "Crystallization and chemically modified anion-selective porin from *Comamonas acidovorans*." *Acta Crystallogr* 1998, D54:650-653.
- [17] M. S. Weiss, U. Abele, J. Weckesser, W. Welte, E. Schiltz, and G. E. Schulz, "Molecular architecture and electrostatic properties of a bacterial porin." *Science* 1991, 254(5038):1627-1630.
- [18] M. S. Weiss, A. Kreuzsch, E. Schiltz, U. Nestel, W. Welte, J. Weckesser, and G. E. Schulz, "The structure of porin from *Rhodobacter capsulatus* at 1.8 Å resolution." *FEBS Lett* 1991, 280(2):379-382.

- [19] A. Kreuzsch, M. S. Weiss, W. Welte, J. Weckesser, and G. E. Schulz, "Crystals of an integral membrane protein diffracting to 1.8 Å resolution." *J Mol Biol* 1991, 217(1):9-10.
 - [20] M. A. F. Jalal and D. van der Helm, "Purification and crystallization of ferric enterobactin receptor protein, FepA, from the outer membranes of *Escherichia coli*." *FEBS Lett* 1989, 243(2):366-370.
 - [21] X. Tu and K. Kawai, "Isolation and characterization of major outer membrane proteins of *Edwardsiella tarda*." *Fish Pathol* 1998, 33(5):481-487.
- (Received: 29 October 2018, Accepted: 21 January 2019)